

2D benchmark experiments and simulations of density coupled flow problems

Inauguraldissertation

Zur Erlangung der Würde eines Doktors der Philosophie
vorgelegt der
Philosophisch-Naturwissenschaftlichen Fakultät
der Universität Basel

von

Markus Wolfgang Konz

Basel, 2010

Originaldokument gespeichert auf dem Dokumentenserver der Universität Basel
edoc.unibas.ch



Dieses Werk ist unter dem Vertrag „Creative Commons Namensnennung-Keine kommerzielle Nutzung-Keine Bearbeitung 2.5 Schweiz“ lizenziert. Die vollständige Lizenz kann unter **creativecommons.org/licences/by-nc-nd/2.5/ch** eingesehen werden.

Genehmigt von der Philosophisch-Naturwissenschaftlichen Fakultät auf Antrag von Prof.
Dr. Philippe Ackerer und
Prof. Dr. Peter Huggenberger

Basel, den 17.02.2009

Prof. Dr. E. Parlow
Dekan



Namensnennung-Keine kommerzielle Nutzung-Keine Bearbeitung 2.5 Schweiz

Sie dürfen:



das Werk vervielfältigen, verbreiten und öffentlich zugänglich machen

Zu den folgenden Bedingungen:



Namensnennung. Sie müssen den Namen des Autors/Rechteinhabers in der von ihm festgelegten Weise nennen (wodurch aber nicht der Eindruck entstehen darf, Sie oder die Nutzung des Werkes durch Sie würden entlohnt).



Keine kommerzielle Nutzung. Dieses Werk darf nicht für kommerzielle Zwecke verwendet werden.



Keine Bearbeitung. Dieses Werk darf nicht bearbeitet oder in anderer Weise verändert werden.

- Im Falle einer Verbreitung müssen Sie anderen die Lizenzbedingungen, unter welche dieses Werk fällt, mitteilen. Am Einfachsten ist es, einen Link auf diese Seite einzubinden.
- Jede der vorgenannten Bedingungen kann aufgehoben werden, sofern Sie die Einwilligung des Rechteinhabers dazu erhalten.
- Diese Lizenz lässt die Urheberpersönlichkeitsrechte unberührt.

Die gesetzlichen Schranken des Urheberrechts bleiben hiervon unberührt.

Die Commons Deed ist eine Zusammenfassung des Lizenzvertrags in allgemeinverständlicher Sprache: <http://creativecommons.org/licenses/by-nc-nd/2.5/ch/legalcode.de>

Haftungsausschluss:

Die Commons Deed ist kein Lizenzvertrag. Sie ist lediglich ein Referenztext, der den zugrundeliegenden Lizenzvertrag übersichtlich und in allgemeinverständlicher Sprache wiedergibt. Die Deed selbst entfaltet keine juristische Wirkung und erscheint im eigentlichen Lizenzvertrag nicht. Creative Commons ist keine Rechtsanwaltsgesellschaft und leistet keine Rechtsberatung. Die Weitergabe und Verlinkung des Commons Deeds führt zu keinem Mandatsverhältnis.

Quelle: <http://creativecommons.org/licenses/by-nc-nd/2.5/ch/>

Datum: 3.4.2009

Content

Content.....	iv
Acknowledgements.....	5
Summary.....	6
I. Introduction	8
I.1 Major targets and questions of this study	8
I.2 General background of this work	9
I.3 Regional subsrosion processes.....	9
I.4 Variable density flow phenomena	12
I.5 Mathematical models of variable density flow in porous media systems	13
I.6 Existing theoretical and experimental benchmark tests	15
I.7 Measurement techniques to determine solute concentrations in flow tank experiments	18
II. Methodology	20
II.1 Measurement of salt concentrations in 2 D flow tanks using resistivity technology and photometry	20
II.1.1 On the measurement of solute concentrations in 2D flow tank experiments..	21
II.2 Measurement of salt concentrations in 2D flow tanks using transmission or reflection intensity measurements.....	44
II.2.1 Comparison of light transmission and reflection techniques to determine concentrations in flow tank experiments	45
III. Benchmarking numerical density-flow models	58
III.1 2D Stable Layered Laboratory-scale Experiments for Testing Density-coupled Flow Models	59
IV. Experiments and simulations of 2D-density flow problems in heterogeneous porous media.....	83
IV.1 Variable-density flow in heterogeneous porous media – Laboratory experiments and numerical simulations	84
V. Conclusions and outlook.....	99
Conclusions.....	99
Outlook	101
References.....	102
Curriculum Vitae	110

Acknowledgements

Numerous people have contributed to the successful completion of this thesis in different ways. I would like to express my gratitude to each of them.

I would like to thank my lector Prof. Dr. Peter Huggenberger for supporting this interesting topic and for providing an open and friendly working environment.

I am very grateful to Dr. Philippe Ackerer who encouraged me and inspired me throughout all stages of my work. His optimistic manner made the time at his institute in Strasbourg very enjoyable for me. This is also because of Dr. Anis Younes who helped me a lot with the numerical simulations. Sincere thanks goes to Claude Veit, without him the technical realisation of the flow tank wouldn't have been possible. He shared all the passion and exertion in the lab with me. I want to thank all the other colleagues in Strasbourg for many helpful scientific discussions and nice hours without scientific discussions.

Dr. Lukas Rosenthaler introduced me to numerical image processing techniques and contributed significantly to the development of the image analysis method. Edi Meier did a great job on the resistivity based concentration measurement devices. He was always open for fruitful discussions. Dr. Franz Conen always had an open door for my questions.

A special thank goes to Silvia Leupin and Antoinette Lüdin for their administrative help. Dr. Eric Zechner and Ralph Kirchhofer contributed to the success of my thesis in different ways through intensive discussions and IT support. I want to express my gratitude to all colleagues at the Applied and Environmental Geology (AUG) group for a very good time and an inspiring working environment.

My parents encouraged my interest in natural phenomena and enabled me to study such a fascinating subject. They further supported all my interests, whether they were related to my studies or to my spare-time activities.

Last but not least, I want to thank my wife Nadine, for sharing all my joys and frustration.

Summary

Variations of fluid densities can alter flow patterns and transport processes, if solute concentration differences are high enough to cause relevant density contrasts. Since numerous environmental problems are related to these phenomena, the need for accurate process description and modeling continues to increase. The numerical simulation of such processes is challenging due to the strong non-linear coupling of flow and transport processes. Therefore, experimental studies are required to elaborate the basic principles and to test numerical codes in order to provide reliable tools for water resources management and planning. In this thesis, density-coupled flow processes under the influence of geometrical boundary conditions are studied and numerical codes are tested against high resolution experimental data.

Photometric methods were further developed to increase the accuracy of measurements in flow tank experiments. They directly related digitally measured intensities of a tracer dye to solute concentrations. This enabled an effective processing of a large number of images in order to compute concentration time series at various points of the flow tank and concentration contour lines. Perturbations of the measurements were lens flare effects and the image resolution. Transmissive and reflective intensity measurements were compared. The reflection images were more homogeneous in spatial illumination than the transmission images. Major perturbations of the transmissive images were lens flare effects and light dispersion within the bead-water-Plexiglas system which smeared the front of the plume. Based on the conducted evaluation of transmissive and reflective intensity measurements, the reflection data delivered more reliable intensity values to derive solute concentrations in intermediate scale flow tank experiments. The newly developed resistivity measurement system used two different input voltages at gilded electrode sticks to enable the measurement of salt concentrations from 0 to 300 g/l. The method was highly precise and the major perturbations were caused by temperature changes, which can be controlled in the laboratory. The two measurement approaches, photometric and resistivity methods, were compared with regard to their usefulness in providing data for benchmark experiments. Due to the unknown measurement volume of the electrodes, the photometric method was better to determine experiments in a series of laboratory-scale 2D porous medium tank experiments.

Various density-driven flow problems were investigated using well-defined experimental parameters and boundary conditions. The experiments were carried out both in a rectangular flow tank ($158 \times 100 \times 4 \text{ cm}^3$) and in a more complex geometrical setup aiming to study variable density flow in geological formations of aquifers and aquicludes connected via fault zones. An impermeable layer within the porous medium tank forced the solutes to pass through a channel to reach the outlet of the tank. The porous medium was homogeneous in both cases. The image analysis technique delivered 2, 10, 50 and 80% salt concentration isolines at distinct times and breakthrough curves of the dyed saltwater. The experimental data were presented as benchmark problems to evaluate numerical codes. A numerical model based on Mixed Finite Elements for the fluid flow problem and a combination of Discontinuous Galerkin Finite Element and Multi-Point Flux Approximation methods for the transport turned out to be adequate for the simulation of the physical experiments. The high data availability made the proposed benchmark experiments a valuable tool for assessing the performance of density-coupled

flow models. Heterogeneous porous medium experiments were conducted with a low permeability zone in the centre of the tank. Three different boundary conditions, corresponding to different localizations of the inflow and the outflow openings at the opposite edges of the tank, were applied and different flow scenarios are observed in the heterogeneous tank. The numerical model used for the simulations was based on efficient advanced approximations for both spatial and temporal discretizations. The Method Of Lines (MOL) was used to allow higher-order temporal discretization and the model adapted in both the order of approximation and time step to provide the necessary accuracy. The model was able to reproduce the experiments. The numerical results were improved by assuming a non-Fickian dispersivity for high density experiments.

I. Introduction

1.1 Major targets and questions of this study

In order to provide solid tools for a reliable assessment of density-flow related problems, adequate test cases for numerical density-flow codes are needed. Numerical methods have to be tested against highly precise experimental data in order to determine the most appropriate approach for simulating field scale problems. The following targets are considered in this work:

- Development of an experimental setup able to study density flow processes in appropriate dimensions and relevant geometries aiming to represent natural aquifers [Konz *et al.*, 2008 a, b; 2009 a];
- Development of appropriate techniques to measure 2D concentration distributions in porous medium flow tanks [Konz *et al.*, 2008 a, b; 2009 a];
- Benchmarking of numerical codes in homogeneous and heterogeneous porous media [Konz *et al.*, 2009 b, c].

This leads to the following questions, which are discussed in this work:

- How much information is needed to benchmark numerical codes against experimental data, and which technology provides the best data sets?
- Which numerical method is suitable to simulate density flow problems?
- How can density-flow models be used to assess field scale salt dissolution processes?

These questions are considered in the four papers attached to this work. The first two papers [Konz *et al.*, 2008 a; 2009 b] are dealing with technical issues concerning the experimental techniques. Konz *et al.*, [2008 a] compares a resistivity based measurement technique with optical reflection measurements. The second paper [Konz *et al.*, 2009 a] raises the question which type of optical measurements are more reliable, transmission or reflection measurements. The third paper [Konz *et al.*, 2009 b] investigates the ability of two different numerical schemes to reproduce experimental plume patterns. Different geometrical settings are used; a homogeneous porous medium and a more complex geometry with an impermeable layer between a lower and an upper flow region. This setting aims to imitate natural conditions in the region of Basel in order to study the regional flow conditions, which are responsible for the dissolution of halites. The fourth paper [Konz *et al.*, 2009 c] focuses on density flow phenomena in heterogeneous porous media and on non-linear dispersion and fingering. Since aquifers, especially gravel aquifers, are highly heterogeneous, test cases to benchmark numerical models under such conditions are required. This paper presents data sets to test numerical codes under heterogeneous conditions.

1.2 General background of this work

Groundwater circulation in evaporite bearing horizons and resulting subsidence of salt frequently causes geomechanical problems like land subsidence or collapses. This process represents a major concern in infrastructure planning and construction projects such as railway-connections or highways. Furthermore, land subsidences can also be detected within densely populated residential areas causing considerable infrastructural damages. There are four requirements for salt dissolution: (1) a deposit of salt; (2) a supply of water which is unsaturated with respect to NaCl; (3) an outlet for removal of the saline water; and (4) a hydraulic gradient to force water to flow through the system (modified after Johnson, 1981, 1992). The halite (NaCl) dissolution kinetics occurs very fast [e.g., Ritzel, 1911; Wagner, 1949; Durie & Jessen, 1964; James, 1992; Frumkin, 1994, 1998, 2000a, 2000b; Alkattan *et al.*, 1997], so that it can be assumed that water in contact with rock salt is always saturated with respect to halite. For this reason, the rate of transport of dissolved halite is of primary importance to understand subsidence. An increased NaCl concentration in the liquid phase causes higher densities compared to freshwater. Therefore, the transport processes of dissolved halite are highly density-dependent and the simulation of the plume migration requires the solving of coupled transport and flow equations. However, the modelling of density-driven flow in porous media remains challenging, due to the non-linear coupling [Diersch & Kolditz, 2002; Johannsen *et al.*, 2002; Oswald & Kinzelbach, 2004]. Specific experimental studies of the occurring phenomena are required, which can be used to test the existing numerical codes. Those laboratory scale experiments need to represent natural flow systems in terms of geometry but also have to be simplified in a way that simulation inaccuracies can directly be related to numerical errors and not to parameter uncertainty. The experiments have to be highly precise in the description of boundary conditions and experimental parameters. Furthermore, very detailed concentration measurements such as isolines or breakthrough curves (BTC) are required. The present work investigates saltwater flow in 2D porous medium flow tanks under different geometrical setups in homogeneous and heterogeneous porous media.

1.3 Regional subsidence processes

The subsidence process takes place in a depth of 160 m below an open-mined section of the Adlertunnel, Basel, Switzerland, which is part of a new European North-South railway-connection. Further, land subsidences were also detected within densely populated residential areas of Basel in the region of Muttenz-Pratteln based on precision measurements (Figure I.1). These areas are located east of the city of Basel in the tectonic unit of the Tabular Jura and have been excessively used for subsurface solution mining of halite, industrial groundwater pumping, and water withdrawal for drinking water supply. The area is underlain by Triassic and Jurassic strata that dip gently to the southeast and are subdivided by a series of NNE-SSW striking Horst and Graben structures overlain by quaternary sediments. The Horst and Graben structure of the Tabular Jura in the area of Muttenz-Pratteln (Figure I.2) and the Adlerhof-Anticline were explained as the combination of (a) the detachment of the sedimentary cover by gravity gliding and (b) the development of the Rhine Graben Flexure towards the west [Laubscher, 1982].

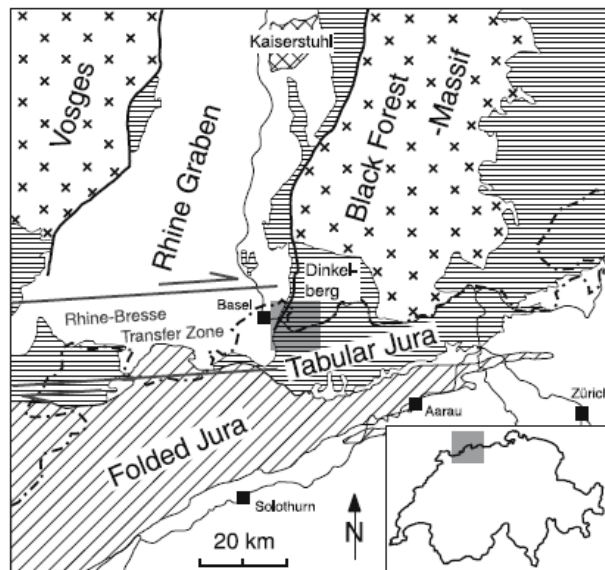


Figure I.1: Regional overview with working area [Spotke *et al.*, 2005, modified after Thury *et al.*, 1994]

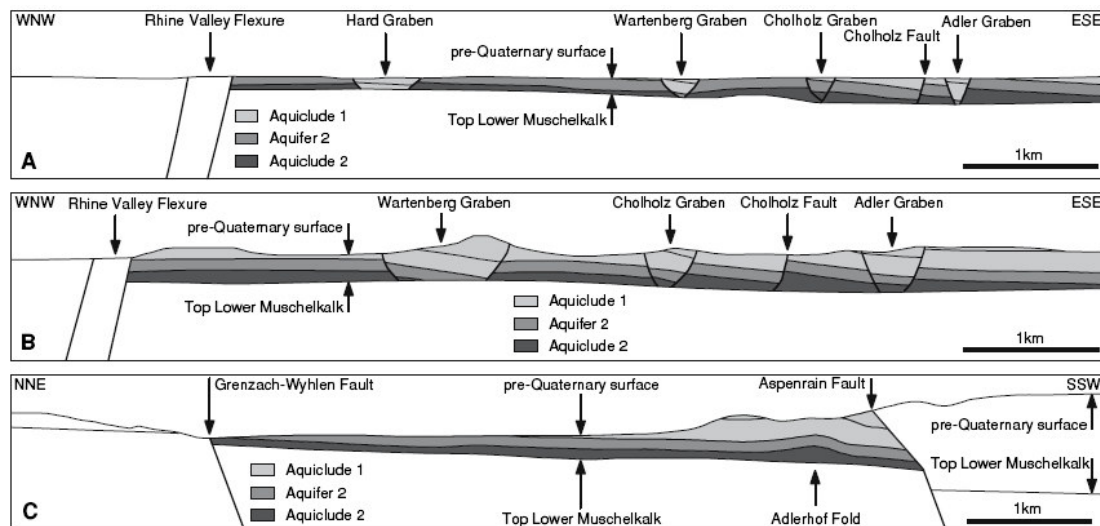


Figure I.2: Cross-sections showing the Horst and Graben structures [Spotke *et al.*, 2005]

According to Gürler *et al.* [1987] some of the sub vertical faults, however, appear to originate at the basement and continue through its sedimentary cover indicating that a combination of thick- and thin-skinned kinematics was active from Middle Eocene to Late Oligocene. A 3D analysis provided insight into the discussion on the kinematics of the area [Spotke *et al.*, 2005] and it could be shown that both thin-skinned and thick-skinned tectonic elements occur in the model area, and that the Adlerhof Anticline and a series of narrow graben structures developed simultaneously during an extensional stress-field trending from E-W to SSE-NNW, which lasted from Middle Eocene to Late Oligocene.

During an observation period of 78 days in 1997, land subsidence occurred in a section of the open-mined Adlertunnel at rates of 6 to 10 mm/month [Aegerter & Bosshardt, 1999].

The vertical subsidence has decreased but still persists since 1997. Analysis of the geodetic data shows that the vertical movements are initiated by solution cavities located at the top of the rock salt layer in the Middle Muschelkalk. The evaporite formations of the Middle Muschelkalk in the Upper Rhine valley have been described by several authors since the discovery of the salt deposits by *Glenk* [1836] to the west of the Red-House near Schweizerhalle. The first comprehensive description of salt deposits in northeastern Switzerland was given by *Verloop* [1909] and *Heim* [1919]. For geotechnical purposes *Trefzger* [1925, 1950] investigated the relationship between solution mining of halite and land subsidence. He compared subsidence and salt production rates for different exploration wells in the Rheinfeldern solution-mining district. His papers are the first ones to mention risk assessment related to areas with low subsidence expectations. For safety reasons, *Hauber* [1971] proposed to shift the salt exploration away from Schweizerhalle to a more southern position in a low populated area (Zinggbrunn, Kt. Basel -Landschaft).

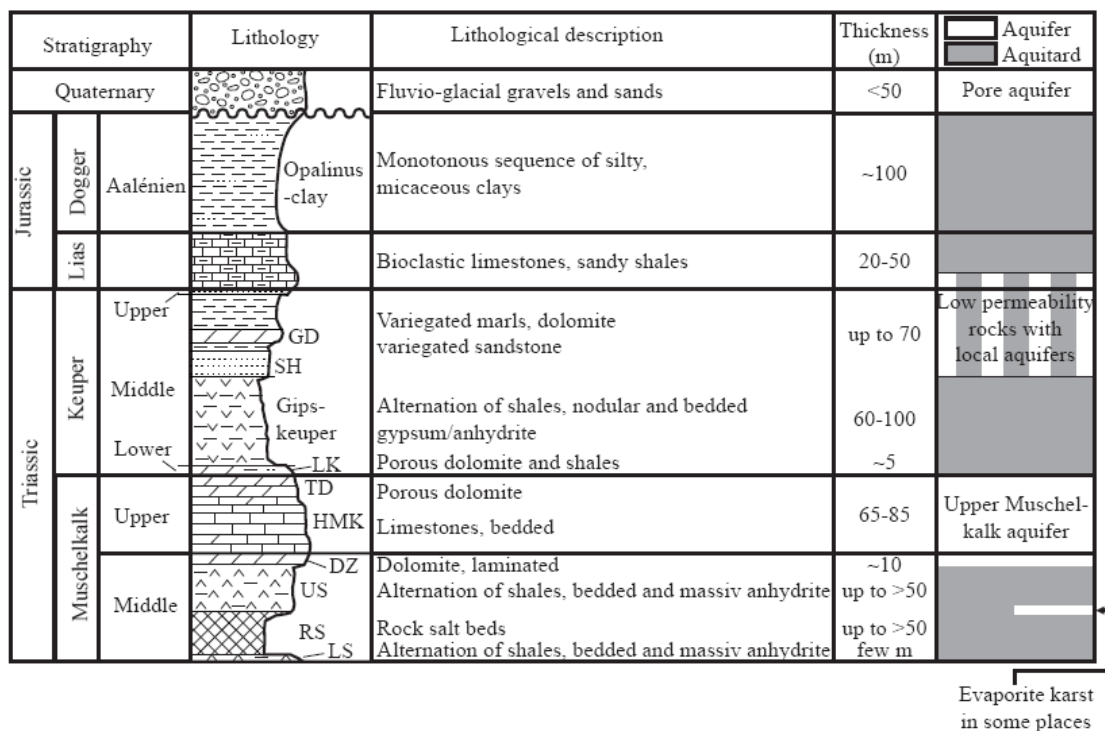


Figure I.3: Schematic, stratigraphic section showing hydrogeological characteristics of the study area (*Gechter* 2008; modified from *Pearson et al.*, 1991). GD = Gansinger Dolomit, SH = Schilfsandstein, LK = Lettenkohle, TD = Trigonodus-Dolomit, DZ = Dolomitzone, US = Upper Sulfatzone, RS = rock salt layer, LS = Lower Sulfatzone.

The rock salt layer is underlying the impermeable upper section of the Sulphat zone (Figure I.2). Drillhole information located beneath the open-mined part of the Adlertunnel revealed that the lower section of the Sulphat zone consists of a ~10 m thick zone of strongly weathered, brecciated units and sequences of sandy marls and clays with intercalations of gypsum and anhydrite [*Aegerter & Bosshard*, 1999]. The loss of drill-core material at the bottom of the Upper Sulphat zone is an indication for the existence of a subsrosion zone (interstratal karst) at this level. Very few is known about the spatial

extent and the hydrology of interstratal karst in the area. Latest drillings have shown that these voids (solution cavities) are common at the top of the rock salt layer and that they enlarge to a maximal height of approximately one meter and a width of several tens to hundreds of meters. Within the rock salt units, however, these features are generally absent [Johnson, 1981; Reuter & Stoyan, 1993; Aegerter & Bosshardt, 1999]. Similar observations are documented in the works of Johnson [1981], Reuter & Tolmačev [1990], Reuter *et al.* [1992]. Other than regional scale groundwater circulations, subsrosion process is often caused by the potential interaction between conflicting uses of natural resources, such as groundwater withdrawal for drinking water supply or industrial use and solution mining of halite. Anthropogenic factors such as large-scale groundwater extraction combined with artificial groundwater recharge may significantly increase hydraulic gradients on large parts of the aquifer. As a consequence, larger hydraulic head differences can locally be maintained, which intensify flow in a karst aquifer and, thus, accelerate the karst evolution.

For the assessment of the regional subsidence hazards reliable simulations of the flow processes are required and need to take density-driven flow processes into account. In the flow tank experiments conducted to test the numerical codes we considered the Upper Muschelkalk aquifer as the upper aquifer above the impermeable layer, which is in reality the Sulphate zone in Figure I.3. The lower aquifer is assumed to be at the interface of the halite and the Sulphate zone.

1.4 Variable density flow phenomena

Variable density flow phenomena can be observed in the atmosphere, in oceans and lakes, in soils and aquifers. In the present work, the focus is on groundwater systems. Density dependent flow exhibits characteristic features, which cannot be observed in ordinary groundwater flow, such as the creation of instabilities, referred to as ‘fingering’, caused by a layering of lighter fluids below denser ones, and a topology influenced flow on the aquifer base [e.g. Schincariol & Schwartz, 1990; Pearl *et al.*, 1993; Swartz & Schwartz, 1998; Oswald *et al.*, 2007]. The flow field strongly influences the solute transport and the solute concentration determines the structure of the flow field, which alters the dynamics of the flow field. Both flow and transport processes are therefore coupled processes and cannot be considered separately. Besides the already discussed subsrosion processes, variable density flow and transport processes in groundwater systems are related to wide range of problems comprising saltwater intrusion in coastal aquifers [Huyakorn *et al.*, 1987], the leakage from landfills [Ostrom *et al.*, 1992b], radioactive or toxic waste disposal in salt rock formations [Ludwig *et al.*, 2001], and the use of geothermal heat in shallow groundwater systems. Schincariol & Schwartz [1990] showed the impact of density effects on plume migration even with a very small density contrast of 0.8 g/l in their laboratory scale flow tank experiments. Further studies proved a density effect 3 g/l [Koch & Zhang, 1992] density contrasts.

1.5 Mathematical models of variable density flow in porous media systems

The mathematical description of variable density flow in porous media aquifers comprises a set of equations representing the underlying physical processes. The most common models are based on the work of *Bear* [1972]. The reader is referred to, e.g. *Hassanizadeh & Leijnse* [1988], *Nield & Bejan* [1992], *Kolditz et al.* [1998] or *Diersch & Kolditz* [2002] for a detailed discussion of the mathematical models. Here, the models are accepted as a mathematical representation of the physical processes and the equations are presented but not discussed.

Due to the mass conservation of the fluid, the continuity equation can be written as

$$\frac{\partial(\varepsilon\rho(C_m))}{\partial t} + \nabla(\rho(C_m)q) = \rho_s Q_s \quad (I.1)$$

where ρ is the density of the fluid [$M L^{-3}$], ε the porosity [-], Q_s the sink/source term [$L T^{-1}$], ρ_s the density of the sink/source term [$M L^{-3}$], q the Darcy's velocity [$L T^{-1}$] and C [$M L^{-1}$] the fluid concentration. The flow of the salt mass does not only consist of the advection but also on dispersion. This part results from both molecular diffusion and hydrodynamic dispersion. Fick's law describes the molecular diffusion with the pore water diffusion coefficient D_m

$$\frac{\partial C_m}{\partial t} = \nabla(D_m \nabla C_m) \quad (I.2)$$

C_m is the mass fraction: mass of salt/ total mass of fluid [M_s/M_T].

Equation (I.2) holds for a constant temperature and a single pollutant. In more general cases, the mass transport can be caused by chemical potential gradients, temperature gradients, or by another dissolved solute.

The hydrodynamic dispersion is described with a comparable approach and the solute mass transport equation defines as

$$\frac{\partial(\varepsilon\rho(C_m)C_m)}{\partial t} + \nabla(\rho(C)qC_m - \varepsilon\rho(C_m)(D + D_m)\nabla C_m) = C_{m_s}\rho_s Q_s \quad (I.3)$$

where D is the dispersive tensor and C_{m_s} the concentration mass fraction of the sink/source term. Here, the D_m describes the effective molecular diffusion in a porous medium, which is reduced compared to the free diffusion in fluids because of the increased flow length in the porous medium. The dispersive tensor depends on the flow velocity, $v=q/\varepsilon$ and is given by

$$D_{ij} = \frac{(\alpha_L - \alpha_T)}{|v|} v_i v_j + (D_m + \alpha_T |v|) I \quad (I.4)$$

Longitudinal and transversal dispersivities α_L, α_T [L] are dispersion lengths in and transversal to the flow direction. Both can be considered as properties of the porous medium. This approach assumes that the center of mass of the contaminant plume travels with the average fluid velocity and that the mechanical and chemical spread of the contaminant around this center of mass can be described completely by a Fickian process given a high degree of homogeneity in the hydraulic conductivity field [Berkowitz & Scher, 2001]. The advection-dispersion equation (I.3) fails to capture contaminant migration if preferential flow paths exist. Non-Fickian tracer transport in ‘homogeneously’ packed column experiments were clearly shown by Hoffman *et al.* [1996] and Oswald *et al.* [1997]. Field and laboratory analyses demonstrate that dispersivity is not constant but is dependent on the time and/or length scale of experiment [Gelhar *et al.*, 1992]. Such scale-dependent dispersion (also referred to as ‘‘anomalous’’ or ‘‘non-Gaussian’’) is often referred to as ‘‘non-Fickian’’ transport [Levy & Berkowitz, 2003]. Berkowitz & Scher [1995] introduced the continuous time random walk theory to account for a very wide range of non-Fickian and Fickian transport behaviors. Besides heterogeneities, density or viscosity contrasts are argued to affect the dispersivity. Several authors [Brigham *et al.*, 1961; Slobod & Howlett, 1964; Standards Australia, 1995; Kempers, 1991; Hassanizadeh & Leijnse, 1995; Watson *et al.*, 2002] have reported experiments showing consistently that, for the stable conditions, an increase in the density or viscosity contrast leads to a reduced mixing zone. Thus, in macroscopic terms, the hydrodynamic dispersion coefficient will vary with these contrasts. Watson *et al.* [2002] carried out a series of laboratory experiments for testing density-dependent flow and transport theories. The results show clearly that Darcy’s law is valid, whereas a non-linear extension of Fick’s law [Hassanizadeh & Leijnse, 1995] was necessary to simulate the experiments accurately.

Besides the transport equation (I.3) Darcy’s law plays a crucial role in groundwater flow and relates pressure p and q following

$$q = -\frac{k}{\mu}(\nabla p \pm \rho(C)g) \quad (I.5)$$

where g is the gravity acceleration [$L T^{-2}$] and μ is the dynamic viscosity of the fluid [$M L^{-1}T^{-1}$]. The permeability k depends on the aquifer properties and often the hydraulic conductivity k_f is used instead, being

$$k_f = \frac{\rho(C)gk}{\mu} \quad (I.6)$$

The maximum concentration is defined by aquifer conditions in terms of temperature, pressure, pH, and further dissolved materials. Here, the concentration is related to the maximal concentration used for the experiments.

Equations (I.1), (I.3), (I.4), and (I.5) are a system of nonlinear, partial differential equations coupled by density and viscosity of the fluid. Both the density and the viscosity depend on temperature and pressure besides the salt concentration. However, the pressure dependence of viscosity is negligible. In terms of density, pressure is either neglected or can be considered in the storage term. The most popular state equations are the linear model for density [Voss, 1984] and the polynomial model for viscosity

$$\varphi = \varphi_0 + 200C_m \quad (\text{I.7})$$

$$\mu = 1.002 \times 10^{-3} (1 + 0.4819C_m - 0.2774C_m^2 + 0.7814C_m^3) \quad (\text{I.8})$$

with φ_1 being the fluid density at saturation, φ_0 , μ_0 the freshwater density and viscosity and a_i are fitted coefficients. The linear model for density in (I.7) is easy to handle and works well for absolute concentrations being significantly smaller than the maximal possible concentration of dissolved salt. For the entire concentration range, however, an exponential model fits best to the measured values as stated in *Herbert et al.* [1988] and *Leijnse* [1992]. *Herbert et al.* [1988] proposed the third order polynomial function given in (I.8), which is valid for the entire concentration range and fits well to the measured values. *Molson & Frind* [1994] developed a relation between temperature and density, which can be used if temperature dependent density variations need to be considered. This is not the case in this work.

1.6 Existing theoretical and experimental benchmark tests

Commonly, three benchmark tests for density-coupled flow models are used: The Hydrocoin problem of a simplified salt dome [*OECD*, 1988]; the Henry problem of seawater intrusion [*Henry*, 1964] and the unstable Elder problem [*Elder*, 1967]. In the following summarized details on the three test cases are given.

Hydrocoin, level 1, Case 5

This test problem was designed according to the conditions above a salt dome. The modeling domain is a vertical cross section through an aquifer with a simple rectangular geometry (Figure I.4). A Dirichlet boundary condition is set in the center of the aquifer base for the salt concentration imitating a salt dome. The remaining base boundary and the side edges are no flow boundaries. The upper edge maintains a linear pressure gradient forcing a freshwater flow from one side to the other. The hydrogeological parameters are constant throughout the domain. This test case is commonly used for intercomparison of numerical solutions because the solution is not exactly known and the different numerical codes can only be evaluated by plausibility assessments. Therefore, various flow patterns exist depending on the used parameters like the diffusion coefficient, dispersivities, numerical methods, convergence criteria and the realization of the boundary condition at the base of the domain. Numerous authors have presented simulations of the problems, e.g. *Herbert et al.* [1988], *Oldenbourg & Preuss* [1995], *Johns & Rivera* [1996], *Oldenbourg et al.* [1996], *Konikow et al.* [1997] and *Kolditz et al.* [1998].

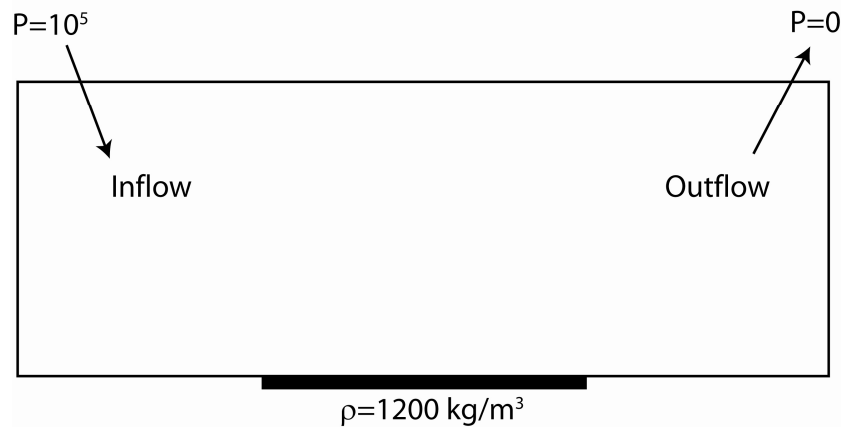


Figure I.4: Problem definition of the Hydrocoin test case [after *Herbert et al.*, 1988].

Henry problem of seawater intrusion

This test case represents a simplified seawater intrusion scenario. *Henry* [1964] formulated the model by the use of dimensionless parameters and a solution for stationary salt concentration distributions is given by an infinite progression. This kind of solution is called a semi-analytical solution. The model domain is rectangular and the parameters are constant and homogeneous with impermeable flow boundaries at the top and bottom of the domain (Figure I.5).



Figure I.5: Problem definition of the Henry test case [after *Kinzelbach et al.*, 1998].

Freshwater flows into the domain from the left edge and a hydrostatic pressure of seawater with a density being 1.025 times the density of freshwater prevails on the right edge. The lower part of the seawater edge shows an influx of saltwater. Freshwater leaves the domain in the upper part whereas in the middle part mixed water flows out of the domain. The boundary conditions are simplified and thus physically not sound on the seaward boundary, because a constant concentration is assumed although freshwater flows out of the domain at the upper edge. A realization of such a transmission boundary condition is difficult because the position of the turning point from inflowing saltwater to outflowing freshwater is not known in advance. However, these shortcomings show almost no effect on the isolines of the inflowing saltwater at the lower right edge. Simulations of the original Henry problem showed deviations from the semi-analytical solution [*Frind*, 1982; *Huyakorn et al.*, 1987; *Galeati et al.*, 1992; *Croucher & O'Sullivan*, 1995] partly caused by a different use of the diffusion coefficient [*Voss & Souza*, 1987]. Furthermore, Henry's solution was not calculated exact enough as shown

in *Segol* [1994]. A revised version of the Henry problem [*Segol*, 1994] can be better simulated with existing codes [*Oswald et al.*, 1996]. *Voss & Souza* [1987] stated that this test case gives no details on the consistency of the velocity approximation or of the treatment of sharp interfaces. Therefore, the Henry problem can be viewed as a minimal standard to test the quality of numerical solutions. Furthermore, the density contrast is relatively small and thus the problem exhibits relatively small non-linearity.

Elder problem of instable flow and fingering

Elder [1967] conducted Hele-Shaw cell experiments to study the development of fingers caused by a vertical temperature gradient. Flow of an incompressible viscose fluid through parallel layered plates follows the Darcy's law so that the stream patterns are comparable to flow in porous medium [*Nield & Bejan*, 1992]. Simulations of the problem are published by e.g. *Oldenbourg & Preuss* [1995], *Leijnse* [1992], *Kolditz et al.* [1998] and recently *Ackerer & Younes* [2008]. An analogue problem can be designed using a vertical salt concentration gradient instead of temperature gradients. In the middle part of the upper boundary of a rectangular domain a maximal value ($c=1$) of concentration is given, the entire lower boundary imposes a value of 0 for concentration (Figure I.6).

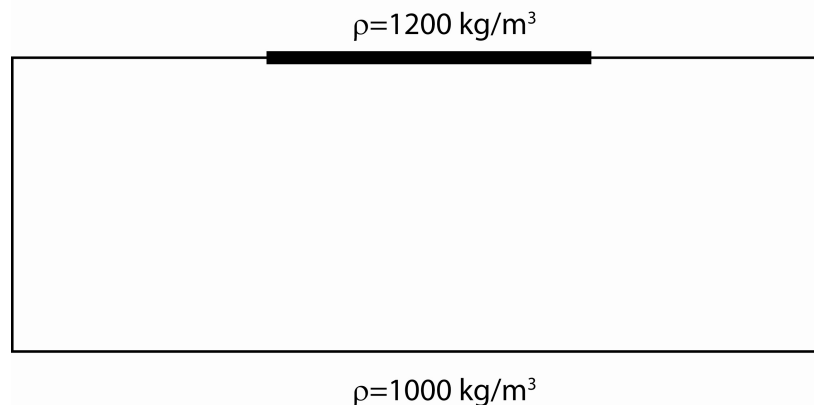


Figure I.6: Problem definition of the Elder test case [after *Voss & Souza*, 1987].

Apart from the upper two corners the boundaries are impermeable for flow and salt transport. A constant pressure is assigned to these corners. Salt enters the domain as a diffusive flux over the $c=1$ boundary. Following the density contrast, fingering and convection cells develop within the modeling domain. Hydrodynamic dispersion and concentration dependence of viscosity are not considered. Comparable to the Hydrocoin test case, the Elder problem can only be used for model intercomparison because the measurements of *Elder* [1967] are of an insufficient quality and present a temperature driven convection and not a concentration driven one. Further, the simulations are highly sensitive to the grid size or to the applied approximation method, e.g. the Boussinesq-Oberbeck approximation [*Diersch*, 1996; *Kolditz et al.*, 1998].

It can be concluded from the above discussion that the test cases are either not sensitive [Henry problem, *Simpson & Clement*, 2003], or the solution is not precisely known (Elder and Hydrocoin). All three test cases assume homogeneous situations and simple geometries. Either only hydrodynamic dispersion is considered (Hydrocoin) or only diffusion (Henry, Elder) and the boundary conditions are numerically problematic (Elder,

Hydrocoin) or not always physically sound (Henry). Hence, in order to evaluate the accuracy of the numerical codes, an increasing number of laboratory-scale experiments exist for 2D and 3D problems [e.g. *Schincariol & Schwartz*, 1990; *Oostrom et al.*, 1992b; *Swartz & Schwartz*, 1998; *Oswald & Kinzelbach*, 2004; *Goswami & Clement*, 2007]. Laboratory experiments have several advantages: boundary and initial conditions are known, and the porous medium properties can be determined separately. The most relevant advantage however is the uniqueness of the results it what enables an objective code testing by comparing the simulation results with experimental data.

Goswami & Clement [2007] conducted physical experiments to study seawater intrusion according to the Henry problem. They visually derived the 50% isoline of a salt wedge penetrating into a freshwater porous medium reservoir. But the benchmark gave no access to more isolines like the 2% and 10% isolines, nor to breakthrough curves which can be more difficult to match with numerical codes. *Oswald & Kinzelbach* [2004] presented a three-dimensional benchmark problem, the saltpool problem, where the exact experimental results and boundary conditions are known. The experimental dimension is $20 \times 20 \times 20 \text{ cm}^3$, both full 3-D data sets for two experiments and several breakthrough curves for 6 different density contrasts are available and complemented by breakthrough curves for repetition experiments. Although the experiments are three dimensional the flow length might not be long enough to show significant dispersion or complex flow patterns which are sensitive to numerical diffusion.

Besides these stable layered experiments a number of unstable experiments exist which are suited for comparison with numerical results [e.g. *Schincariol & Schwartz*, 1990; *Swartz & Schwartz*, 1998; *Oswald et al.*, 2007]. *Schincariol & Schwartz* [1990] studied the development of a salt plume under horizontal flow conditions in 2D in homogeneous and heterogeneous conditions. Semi quantitative data are available for different density contrasts. A more quantitative study of plume migration in horizontal flow conditions was conducted by *Oostrom et al.* [1992a] and *Oostrom et al.* [1992b]. They used a non-intrusive gamma radiation system to derive salt concentrations in two dimensions. Hele-Shaw cells and photometric methods were used by *Wooding et al.* [1997 a,b] to examine the finger development due to evaporation. Stable layered displacement experiments were conducted by *Hassanizadeh & Leijnse* [1995]; concentrations were measured using conductivity cells. Furthermore, multi species solutions consisting of different solutes [*Cooper et al.*, 1997]. Different methodologies are suitable to measure salt concentrations in flow tanks, the most relevant for 2D and 3D are discussed in the following section.

1.7 Measurement techniques to determine solute concentrations in flow tank experiments

A variety of methods exists for qualitative and quantitative determination of solute transport in porous media experiments. Traditionally this is done by intrusive methods where extracted fluids are analyzed in the laboratory [e.g. *Swartz & Schwartz*, 1998; *Barth et al.*, 2001]. These methods are work intensive and require a well-equipped laboratory for chemical analysis. Furthermore, the temporal and spatial resolution of concentration determination is limited due to point sampling, and perturbations of the flow field cannot be excluded. Electrical resistivity measurement technique to determine salt concentrations (0-300 g/l) at discrete points within the porous media can be used both

in 2D and 3D applications. Resistivity measurements are a well-developed technology to determine ion concentrations of fluids. However, there are only few examples in literature where this technology is used for in-situ measurements in porous media experiments. *Siliman & Simpson* [1987] used electrode arrays in a narrow interval of low concentrations from 50 to 1000 mg/l. *Hassanizadeh & Leijnse* [1995] took platinum disc electrodes facing each other to measure salt concentrations in the range of 0.001 to 0.24 kg kg⁻¹ (about 280 g/l). A 3D application of resistivity measurement technique is given in *Danquigny et al.* [2004]. In the published literature, dyes have been used mainly to qualitatively and quantitatively visualize spatial mixing patterns of contaminants in intermediate scale 2D porous media flow tank experiments. Reflected light is often used for image analysis in intermediate scale experiments [e.g. *Oostrom et al.*, 1992b; *Schincariol & Schwartz*, 1990; *Swartz & Schwartz*, 1998; *Wildenschild & Jensen*, 1999; *Simmons et al.*, 2002; *Rahman et al.*, 2005; *McNeil et al.*, 2006; *Goswami & Clement*, 2007]. The advantage of this technique is that it can be used with non-transparent porous media material, e.g., sand and with thick flow tanks that prevent light transmission. In the literature on photometric measurements of plume distribution in flow tanks, little attention has been paid to errors in concentration determination caused by image resolution (pixels per length), and lens flare. The light transmission technique to measure emitted light from behind the flow tank opposite to the light source is usually used in micro model experiments with thin flow tanks [e.g. *Corapcioglu et al.*, 1997; *Detwiler et al.*, 2000; *Huang et al.*, 2002; *Theodoropoulou et al.*, 2003; *Jones et al.*, 2005]. An excellent literature review of transmissive experiments and data processing techniques can be found in *Catania et al.* [2008]. Since only the transmitted light is recorded for concentration determination, reflections of surroundings can be excluded. The use of transmission intensities has the advantage that migration effects are averaged over the width of the flow model. Therefore, possible 3D effects are less severe than with reflection data. However, light scattering within the system of glass beads, water and Plexiglas leads to light dispersion [*Huang et al.*, 2002; *Rezanezhad et al.*, 2006].

In three dimensions the measurement of concentrations is more complex than in 2D. Hele-Shaw cells and image analysis techniques are not useful and resistivity cells or fluid sample analysis require a huge amount of sampling points in order to provide a representative picture of the concentration distribution and these methods are invasive and may alter the flow field. *Oostrom et al.* [2003] introduced the non-intrusive dual-energy gamma radiation system methods for 3D experiments. Nuclear Magnetic Resonance Imaging (NMRI) can be applied to determine concentration distribution in the porous medium in 3D. This physical method is used to visualise water flow and mass transport in saturated porous and fractured media, e.g. *Guillot et al.* [1991], *Hoffman et al.* [1996], *Greiner et al.* [1997], *Oswald et al.* [1997] or *Oswald & Kinzelbach* [2004]. This method is used to visualise tracer transport using paramagnetic ions as a dissolved contrast agent [e.g. *Pearl et al.*, 1993; *Istok & Humphrey*, 1995; *Hoffman et al.*, 1996; *Oswald et al.*, 2002]. This method is precise but it is limited to small flow tank experiments due to the size of the NMR tomograph.

In this thesis a detailed discussion of the applicability and limitations of the photometric image analysis method to determine plume concentrations in 2D experiments is given in *Konz et al.* [2008 a; 2009a].

II. Methodology

II.1 Measurement of salt concentrations in 2 D flow tanks using resistivity technology and photometry

Paper published in *Hydrology and Earth System Sciences*

On the measurement of solute concentrations in 2-D flow tank experiments

Konz, M.⁽¹⁾; Ackerer, P.⁽²⁾; Meier, E.⁽³⁾; Huggenberger, P.⁽¹⁾; Zechner, E.⁽¹⁾; Gechter, D.⁽¹⁾

⁽¹⁾Department of Environmental Sciences, University of Basel, Institute of Geology, Applied and Environmental Geology, Basel, Switzerland

⁽²⁾ Université Louis Pasteur, Institut de Mécanique des Fluides et des Solides, CNRS, UMR 7507, Strasbourg, France

⁽³⁾ Edi Meier & Partner AG, Winterthur, Switzerland

II.1.1 On the measurement of solute concentrations in 2D flow tank experiments

II.1.1.1 Abstract

In this study we describe and compare photometric and resistivity measurement methodologies to determine solute concentrations in porous media flow tank experiments. The first method is the photometric method, which directly relates digitally measured intensities of a tracer dye to solute concentrations, without first converting the intensities to optical densities. This enables an effective processing of a large number of images in order to compute concentration time series at various points of the flow tank and concentration contour lines. This paper investigates perturbations of the measurements; it was found both lens flare effects and image resolution were a major source of error. Attaching a mask minimizes the lens flare. The second method for in situ measurement of salt concentrations in porous media experiments is the resistivity method. The resistivity measurement system uses two different input voltages at gilded electrode sticks to enable the measurement of salt concentrations from 0 to 300 g/l. The method is highly precise and the major perturbations are caused by temperature changes, which can be controlled in the laboratory. The two measurement approaches are compared with regard to their usefulness in providing data for benchmark experiments aimed at improving process understanding and testing numerical codes. Due to the unknown measurement volume of the electrodes, we consider the image analysis method more appropriate for intermediate scale 2D laboratory benchmark experiments for the purpose of evaluating numerical codes.

II.1.1.2 Introduction

Laboratory experiments are an excellent way of providing data to develop transport theories and validate numerical codes. They have several advantages: boundary and initial conditions are known, the porous medium properties can be defined separately and the experiments can be repeated if necessary. Excellent reviews of mass transfer in porous media at the laboratory scale can be found in *Silliman et al.* [1998] and *Simmons et al.* [2002]. A variety of methods exists for qualitative and quantitative determination of solute transport in porous media experiments. Traditionally this is done by intrusive methods where extracted fluids are analyzed in the laboratory [e.g. *Swartz and Schwartz*, 1998; *Barth et al.*, 2001]. These methods are work intensive and require a well-equipped laboratory for chemical analysis. Further, the temporal and spatial resolution of concentration determination is limited due to point sampling, and perturbations of the flow field cannot be excluded. *Oostrom et al.* [2003] introduced the non-intrusive dual-energy gamma radiation system methods for 3D experiments. *Oswald et al.* [1997] and *Oswald and Kinzelbach* [2004] used the nuclear magnetic resonance (NMR) technique to derive concentration distributions of 3D benchmark experiments for density dependent flow. This method is very precise but it is limited to small flow tank experiments due to the size of the NMR tomograph.

In the published literature, dyes have been used mainly to qualitatively and quantitatively visualize spatial mixing patterns of contaminants in intermediate scale 2D porous media flow tank experiments. The dye itself can be used as contaminant (e.g. *Rahman et al.*,

2005), or it acts as an optical tracer to mark contaminants with density effects [e.g. *Schincariol et al.*, 1993, *Swartz and Schwartz*, 1998, *McNeil et al.*, 2006, *Goswami and Clement*, 2007].

Reflected light is used for image analysis in most intermediate scale experiments [e.g. *Oostom et al.*, 1992, *Schincariol et al.*, 1990, *Swartz and Schwartz*, 1998, *Wildenschild and Jensen*, 1999, *Simmons et al.*, 2002, *Rahman et al.*, 2005, *McNeil et al.*, 2006, *Goswami and Clement*, 2007]. The advantage of this technique is that it can be used with non-transparent porous media material, e.g., sand and with thick flow tanks that prevent light transmission. However, the use of reflected light to quantify dye concentrations can lead to problems with image noise, reflected and diffusive light from surroundings and can therefore alter the image quality. A promising alternative is the light transmission technique to measure emitted light from behind the flow tank opposite the light source [e.g. *Corapcioglu et al.*, 1997, *Detwiler et al.*, 2000, *Huang et al.*, 2002, *Theodoropoulou et al.*, 2003, *Jones et al.*, 2005]. *Catania et al.* [2008] provide an excellent literature review of transmissive experiments and data processing techniques. These studies used very thin small-scale flow models of maximum 1 cm thickness, which enable light transmission.

Variations in lighting, exposure and film development result in non-uniform image intensities between successive images. *Rahman et al.* [2005] used the γ -calibration model to correct the color representation of images (I_{corr}):

$$I_{corr} = a + b \cdot I^\gamma \quad (\text{II.1})$$

where a,b, and γ are correction parameters, assumed to be spatially uniform, and I is the measured intensity. The values of the parameters are determined by fitting the measured intensities of color cards to the ideal model. *Schincariol et al.* [1993] and *McNeil et al.* [2006], amongst others, convert the measured intensities to optical density. Optical density D is non-linearly related to intensity I by:

$$D = \log_{10}(a/I) \quad (\text{II.2})$$

where a is a constant of proportionality. This involves the optimization of intensity vs. optical density standard curve of each image to be investigated and an optimization of optical density vs. concentration standard curve. However, the conversion of intensity to optical density or the application of the γ -calibration model is only necessary if:

1. Analogue images are taken and the film has to be developed and scanned to convert the image to digital data;
2. Automatically, non-linearly adjusted and compressed images are used.

If only the spatial evolution of plumes at a limited number of timesteps is investigated, the computational efficiency is of minor importance because the intensity vs. optical density standard curve has to be optimized only for a small number of images. For the evaluation of numerical codes however, breakthrough curves at distinct points with a high temporal resolution are necessary. This requires processing of a large number of images and the computational efficiency becomes a significant criteria. As opposed to *Schincariol et al.* [1993], *Swartz and Schwartz* [1998] and *McNeil et al.* [2006] we relate linearly measured intensities directly to concentrations without standardization to optical densities to enable processing of a large number of images with the aim of deriving

breakthrough curves of a high temporal resolution. In this study, we apply the light reflection technique because the back wall of our flow tank holds devices for measuring resistivity and pressure, which preclude the use of a light transmission technique. The light reflection technique is more appropriate if experiments are done with porous media that is more opaque than glass beads such as clayey inclusions and lenses. Therefore, this study aims to provide details on this technique. We investigate the impact of image resolution (pixels per length) on the precision of the results, and the impact of lens flare on intensity measurements. In the literature on photometric measurements of plume distribution in flow tanks, little attention has been paid to errors in concentration determination caused by these effects.

While image analysis is a useful tool for 2D applications, electrical resistivity measurement technique to determine salt concentrations (0-300 g/l) at discrete points within the porous media can be used both in 2D and 3D applications. We present in this paper technical details of the resistivity method and discuss the implementation of this method for porous media experiments. Resistivity measurement is a well-developed technology to determine ion concentrations of fluids. However, there are only few examples in literature where this technology is used for in-situ measurements in porous media experiments. *Siliman and Simpson* [1987] used electrode arrays in a narrow interval of low concentrations from 50 to 1000 mg/l. *Hassanizadeh and Leijnse* [1995] took platinum disc electrodes facing each other to measure salt concentrations in the range of 0.001 to 0.24 kg kg⁻¹ (about 280 g/l). A 3D application is given in *Danquigny et al.* [2004]. However, none of the authors present technical details of their systems. Since not all measurement systems are standard commercial systems, a significant effort is necessary to develop the technology. The aim of the detailed description of both independent measurement techniques, resistivity measurement and image analysis is to provide experimentalists with information to construct measurement systems and assess their applicability to the specific experiments. We demonstrate the advantages and limitations of these techniques based on a model experiment, and discuss them in view of their applicability to benchmark experiments on density dependent flow.

II.1.1.3 Description of the experimental setup

The flow experiments were conducted in a Plexiglas tank with the dimensions (L × H × W) of 1.58m × 0.6 m × 0.04 m (Figure II.1 and Figure II.2). The back of the tank holds measurement instruments, such as pressure sensors, electrodes of the resistivity measurement cell system (RMC) and temperature sensors. The front side of the tank consists of a clear Plexiglas pane facilitating visual observation of the tracer movement through the homogenous porous medium during the course of the experiments. The tank has four openings at the bottom, which are regulated by valves. Another six openings

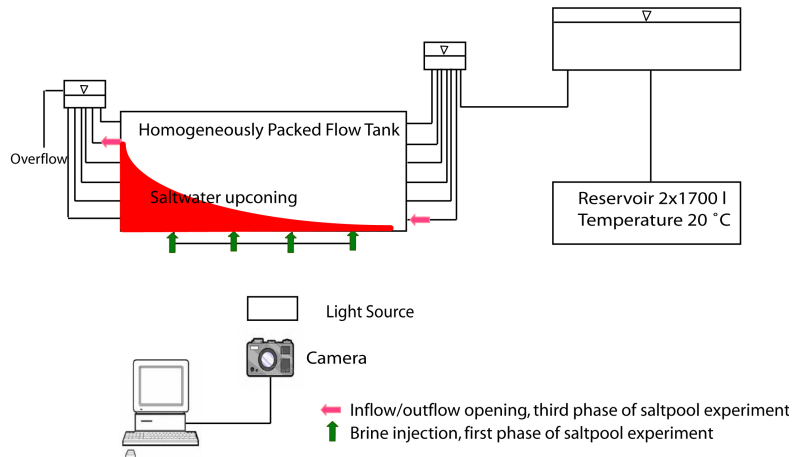


Figure I.1: Schematic experimental setup.

each are placed at the left and right side of the tank. These openings are also regulated by valves and connected to freshwater reservoirs. The height of the reservoirs can be adjusted to adapt the velocity of the water inside the porous media. Two 1700 l deionized freshwater reservoirs, where the water temperature is kept constant at 20 °C to avoid degassing in the porous media, maintain water supply to the inflow reservoir. Tension pins with a diameter of 0.5 cm were installed within the tank to prevent the deformation of the Plexiglas wall. Because these obstacles are minor, we assume that they do not perturb the flow. Glass beads with a diameter of 0.6 mm were used as a porous media. The tank was homogeneously packed. During filling, there was always more water than glass beads in the tank in order to avoid air trapping. A neoprene sheet and air tubes were placed between the Plexiglas cover and the porous media. The air tubes can be inflated to compensate for the free space when the glass bead settles, preventing preferential flow along the top cover of the tank. A supplementary experiment with traced water and horizontal flow conditions revealed that there are no preferential pathways and that the water flows homogeneously through the porous media.

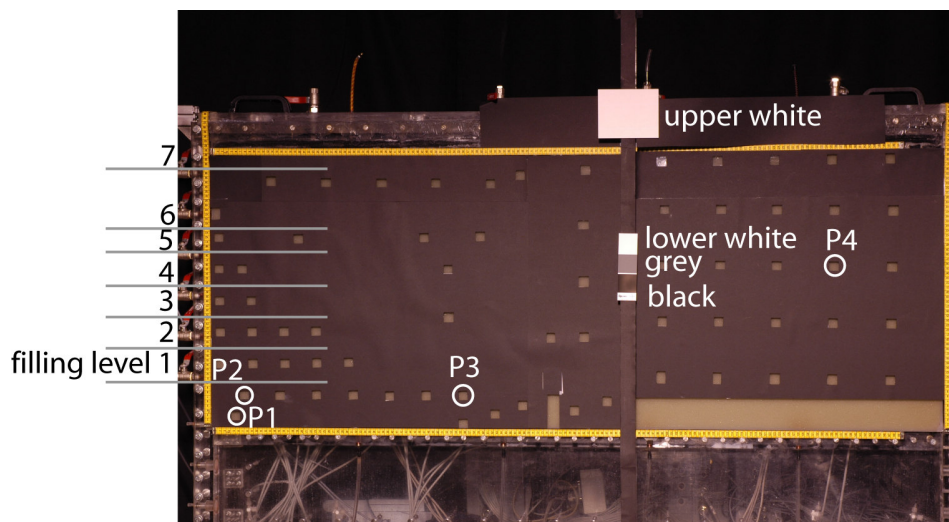


Figure II.2: Tank of E3 with mask to reduce effects of flare and filling levels of E4.

Five different experiments were conducted in order to assess the image analysis methodology and the resistivity measurement system. Table II.1 summarizes the experiments.

Table II.1: Experiments conducted to assess the image analysis technique and the resistivity measurement cell (RMC) technology.

Experiment	Number	Objective
Successively attached black cards	E1	Demonstrate lens flare effects
Saltpool flow experiment; without mask	E2	Demonstrate the impact of lens flare on measured reflection intensities
Saltpool flow experiment; with mask	E3	Test a possibility to reduce the measurement error
Progressively filling of salt-dye solutions of different concentrations; with mask	E4	Estimate the error caused by lens flare effects
Continuous inflow of marked saltwater	E5	Mass balance determination at different times

In the first experiment E1, we successively placed black cards on the front window of the tank to demonstrate the lens flare effect. E2 and E3 are density-dependent flow experiments using red dyed saltwater with a density of 1063 g/l. The experiments E2 and E3 in Table II.1 consisted of four phases. The brine with an initial concentration of 100 g/l was marked with 1 g/l of the red food dye Cochineal Red A (E124). In the first phase of the experiment, the brine was pumped into the domain from four openings at the bottom of the tank, as indicated in Figure II.1 by the green arrows. Buoyancy effects forced the brine to move laterally in the second phase and form a planar brine-freshwater interface. No flow was applied in this second phase through any openings in the tank. At the end of this phase, the brine had equilibrated with a mixing zone of about 4 cm above 3 cm of brine with the initial concentration of 100 g/l. The head difference between inflow and outflow reservoirs generated a constant flow during the third phase of the experiment, which we refer to in the following as the flow phase. Flow through the inflow opening on the lower left side of the tank (11 cm above the ground, red arrow in Figure II.1), close to the brine and the outflow opening on the upper right side of the tank (45 cm above the ground, red arrow in Figure II.1), forced an upconing of the saltwater below the outlet as shown in Figure II.1. Mechanical dispersion and advection processes cause the upconing of the saltwater. The last phase is the calibration phase to enable the conversion of dye intensities to concentrations.

The difference between E2 and E3 is the attached mask in E3. The mask has observation holes and reduces the flare effect. E4 is an experiment to assess the error caused by the flare effect. We filled the tank progressively with solutions of different salt-dye concentrations and evaluated the impact of lens flare on the observation holes (see Figure II.2 for filling levels). In E5, the dense saltwater (same as in E2 and E3) is continuously pumped into the porous media through a single inflow opening at the edge of the tank. This enables the exact quantification of saltwater entering the domain and the image analysis technique can be verified using salt mass balances.

II.1.1.4 Concentration determination with photometry

II.1.1.4.1 Image acquisition and general concept of optical concentration determination

The dense fluid was marked with a dye to visually differentiate the saltwater from the ambient pore water. Cochineal Red A (E124) was used as tracer. This food dye is non-sorbing, nonreactive with NaCl in concentrations used for the experiment [Rahman *et al.*, 2005 and our own batch experiments]. Photometric analysis of different dye-saltwater solutions revealed that there is no degradation or optical decay of dye over a period of up to 7 days. Different diffusivity could cause separation of dye and saltwater leading to erroneous concentration determinations. In the literature other authors have used various dyes, including food color, to track the movement of dense saltwater in laboratory-scale aquifer models. Neither Schincariol *et al.* [1993], Swartz and Schwartz [1998] nor Goswami and Clement [2007] reported difficulties due to dye-salt separation. The latter used a red food color comparable to Cochineal Red A. We conducted column experiments (1m length) with different salt-dye solutions and compared breakthrough curves of salt and colour. The salt concentrations were measured using standard resistivity cells (WTW) and the color concentrations were determined using a spectrometer (Shimadzu UV-1700 Pharma Spec). No separation could be observed. Furthermore, differences in the diffusivity are of minor importance in experiments dominated by advection as is the case in our experiments.

To determine concentration distributions in the tank, we took photos with a digital camera (Nikon D70) using a reproducible illumination with a single light source placed right above the camera at a distance of ~3 m from the tank. The light source (EKON JM-T 1x400 W, E40) was adjusted and checked with a luxmeter to minimize spatial lighting nonuniformity. However, it was not possible to totally avoid lighting nonuniformity and a higher intensity remains in the center of the photographed domain. White, grey and black cards were attached on the front pane of the tank (Figure II.2). A dark curtain placed around the entire experimental setup prevented reflections of any objects on the tank pane. Furthermore, in order to avoid lighting nonuniformity due to daylight, there were no windows in the laboratory. All camera parameters were set manually (shutter speed 1/8s, aperture 13.0, ISO200). For image processing it is important that images, taken at different times, match on a pixel-by-pixel basis. A computer programme (Nikon camera controlPRO) controlled the camera, which was not touched or removed during the entire experiment including the calibration procedure. Therefore, neither rotation nor translation of images is necessary. The digital camera stores linear raw data (.nef) beside the automatically non-linearly processed photos (.jpg). Raw data is the output from each of the original red, green and blue sensitive pixels of the image sensor, after being read out by the array electronics and passing through an analogue-to-digital converter. A linear development means that no gamma correction has been applied yet, and thus levels are distributed along the histogram in a linear way being each of them proportional to the amount of light (number of photons) that the pixel was able to capture during the exposure. The used converter, ddraw, generates linear 16-bit tiff images from the raw data. The 12-bit information gained from the camera is linearly spread along the 16-bit of the tiff image. This was necessary because standard PC systems either work on 8- or 16-bit but not on 12-bit. 16-bit was taken to preserve the information of the 12-bit data (e.g. http://www.guillermoluijk.com/tutorial/dcrow/index_en.htm).

The image-processing procedure includes the following steps: (1) data converting to 16 bit tiff images (65536 intensity values per channel of the RGB color space) with the freeware ddraw (<http://cybercom.net/~dcoffin/dcrow/>), (2) selection of green channel (most sensitive to dye concentrations), (3) correction of fluctuations in brightness, (4) determination of measurement area, (5) construction of a curve that relates intensities to concentrations from calibration images and determination of function parameters for the mathematical formulation of the curve, and (6) conversion of measured intensities of the experiment into concentrations. In the following, steps 3 to 6 are described in detail and we discuss the impact of lens flare on the measurements.

II.1.1.4.2 Correction of fluctuations in brightness (Step 3)

A constant light source is difficult to achieve because of fluctuations in energy supply. The first four graphs in Figure II.3 show the intensities of attached white, grey and black cards (see Figure II.2 for the position of the cards), which are strongly influenced by the fluctuations in lightning. The spikes in the raw data (first four graphs) could be caused by fluctuations in electricity supply.

The intensities shown in the figure were recorded over two days including the night. 0-600 were taken in the evening and overnight, whereas 600 onwards are images taken in the morning and over the day. This could explain the increased fluctuations in energy supply during the day. Existing methods of image processing convert measured intensities into optical densities based on intensity vs. optical density standard curve in order to correct fluctuations in brightness. The reference values of optical density are taken from the attached grey scales. This step is necessary if the raw data are non-linear because analogue photography is used and the photos are developed and scanned, or automatically pre-processed images are taken. Due to the linearity of our raw data, neither the γ -calibration model [Rahman *et al.*, 2005] nor the translation to optical density [e.g. Schincariol *et al.*, 1993] to correct fluctuations in brightness is necessary. The fluctuations can be corrected ($I_{corr}(i,j)$) using the attached upper white card as reference value (I_{ref}) for each image:

$$I_{corr}(i, j) = I(i, j) / I_{ref} \quad (II.3)$$

The last three graphs in Figure II.3 show how the correction method works for the lower white card, the grey and the black cards (Figure II.2). We tested this approach for several points on the tank located not only in the center of the tank but also in the corner of the domain where illumination differences between the reference white and the observation points are highest. The method performs well at all observation points. As a consequence, the images are on the same intensity level after the correction step, and changes in intensity do result only from changes in dye concentration and not from fluctuation in lightning. Minor fluctuations still persist and are related to scattered reflection on the camera lens, which cannot be corrected.

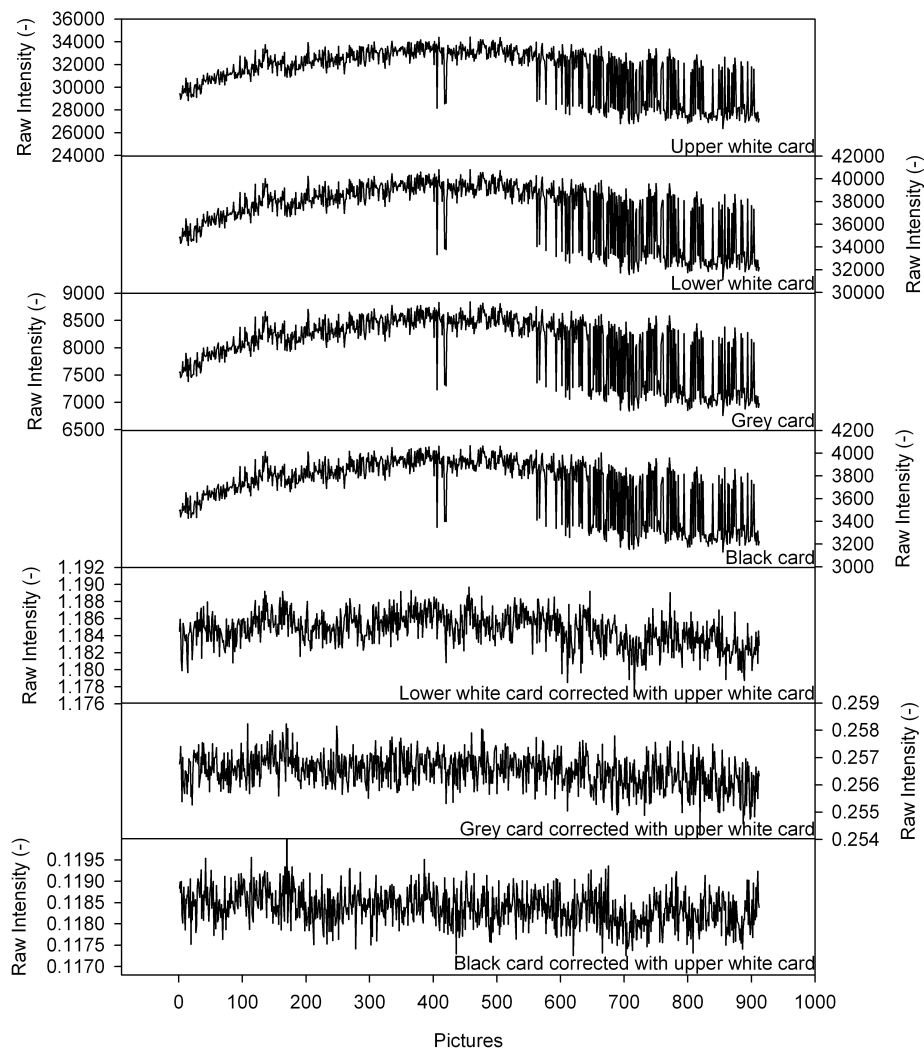


Figure II.3: Measured and processed intensity values of grey and black cards.

II.1.1.4.3 Impact of optical heterogeneity of porous media and determination of measurement area (Step 4)

The resolution of the images is crucial, especially in experiments where concentrations vary spatially with a steep gradient, e.g., in transition zones. In the literature, little attention has been paid to analyzing the impact of the resolution on the precision of the derived concentration data. *Schincariol et al.* [1993] suggested a general median smoothing (3x3 pixels) to reduce noise from bead size. The image resolution of our digital images (approx. 0.31 mm²/pixel) implies a high resolution of the concentration determination at a point. In order to assess the impact of resolution, we filled the tank with solutions of different concentrations, took images of each solution and analyzed the intensity distributions in squares of 25 cm² (8281 pixels) at different positions of the image. The squares were filled equally with the respective solution and, due to the small extent of 25 cm², the impact of uneven lighting can be excluded. As an example of this Figure II.4A shows the intensities of one of the squares for 100 g/l derived from 1x1

pixel and from the median over 5x5, 10x10 and 18x18 pixels. The fluctuation of intensities increases with increasing resolution due to the noise from bead size or the position of the beads.

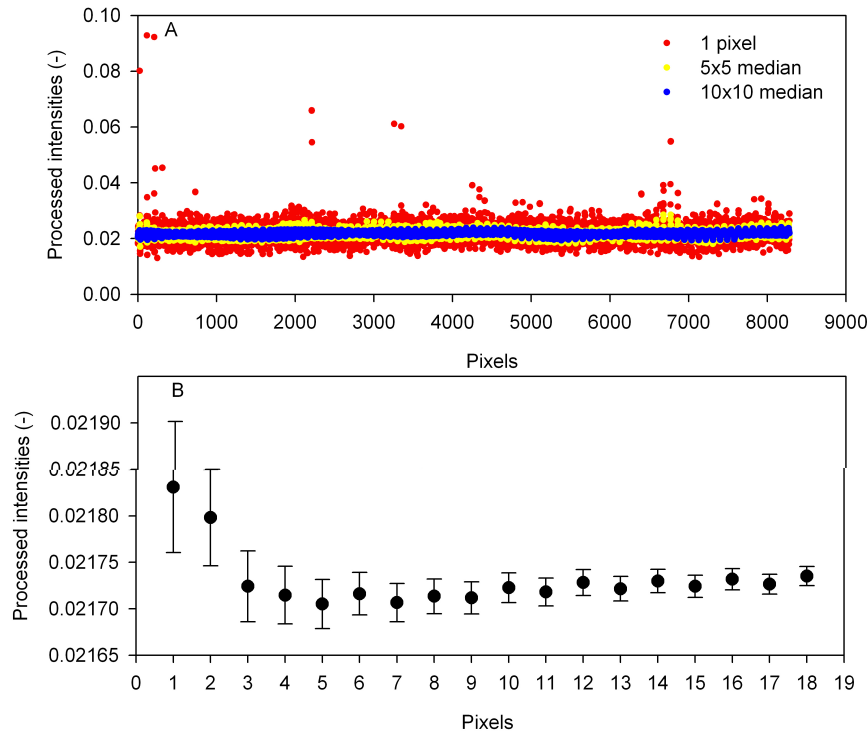


Figure II.4: A: Intensities of the 8281 pixels of a square of 5x5 cm² of calibration image 100 g/l derived as median of squares of 1, 5 and 10 pixels edge length; B: Median of squares of 1x1 to 18x18 pixels and 95% confidential interval.

The comparison of the 95% confidential intervals in Figure II.4B shows that the precision of the medians increases with increasing edge length. These patterns apply to all concentrations and are demonstrated for 100 g/l. The calculated intensities vary significantly for resolutions smaller than 10² pixels. In this study the median over 100 pixels (10 pixels edge length) is taken to calculate concentrations at a point. This corresponds to an area of about 31 mm². The actual resolution for concentration determination is therefore lower than the image resolution itself. Since the noise from the grain size depends on the grain diameter, the adequate resolution has to be derived for each experimental setup.

II.1.1.4.4 Image calibration and converting of intensities to concentrations (Steps 5 and 6)

In order to relate a given value of intensity to a concentration of salt or dye, calibration runs were made with solutions of predetermined dye-salt concentrations. In the calibration experiment solutions of 0.5, 3, 5, 8, 10, 15, 20, 40, 70, 100 g/l of saltwater and the dye concentration of the respective solution at a ratio of 1/100 of the salt concentration were pumped into the tank and photos were taken. Due to the higher ion activity of the saltwater we used salt-dye solutions for calibration. This accounts for

possible intensity differences between equally concentrated solutions of dye-saltwater and dye-freshwater. The solutions were pumped into the tank from the bottom of the tank upwards in a sequential order from low-density solutions to high-density solutions. This prevents instabilities and enables a uniform filling of the domain. 50 photos were made of each calibration step. Since we use linear raw data the brightness-corrected intensities can be translated directly to concentrations based on intensity vs. concentration standard curves, which have to be derived for each point where concentrations are to be determined. In our experiment, the salt concentration, and not the tracer concentration, is of particular interest. Therefore, we relate intensities of the dye directly to salt concentrations (Figure II.5B), which are just 100 times the dye concentration. The plotted intensities vs. concentrations of observation points P1, P2, P3 and P4 (Figure II.2) in Figure II.5B exhibit a non-linear relationship which agrees with observations by *Catania et al.* [2008] and *Jones and Smith* [2005] who used fluorescent dyes. The theoretical relation between intensity and concentration (in the case of transmittance) follows an exponential function. This relation is known as Lambert-Beer's law and it is valid for monochromatic light and for solutions without porous media. Because this is not the case in our experiments, we tested various functions to relate intensity and concentration (power laws of higher order and exponential functions). A second order exponential function turns out to be the most suitable for relating intensities to concentrations (Equation II.4, Table II.2).

$$C(t)_{i,j} = A1_{i,j} \cdot \exp(I_{corr}(t)_{i,j} / t1_{i,j}) + A2_{i,j} \cdot \exp(I_{corr}(t)_{i,j} / t2_{i,j}) + y0_{i,j} \quad (\text{II.4})$$

$C(t)_{i,j}$	Concentration at time t
$A1_{i,j}, A2_{i,j}, y0_{i,j}, t1_{i,j}, t2_{i,j}$	Parameters; see Table II.2 for values
$I_{corr}(t)_{i,j}$	Brightness corrected intensity at time t

Table II.2: Calibration parameters of second order exponential function.

	P1	P2	P3	P4
y0	-0.81727	-0.99127	-0.75114	-0.71146
A1	89.4648	580.7729	376.0868	120.6542
t1	0.04421	0.01295	0.01657	0.03952
A2	355.5046	111.7840	96.76833	417.4293
t2	0.01577	0.03839	0.04733	0.01368
R ²	0.99997	0.99998	0.99998	0.99998

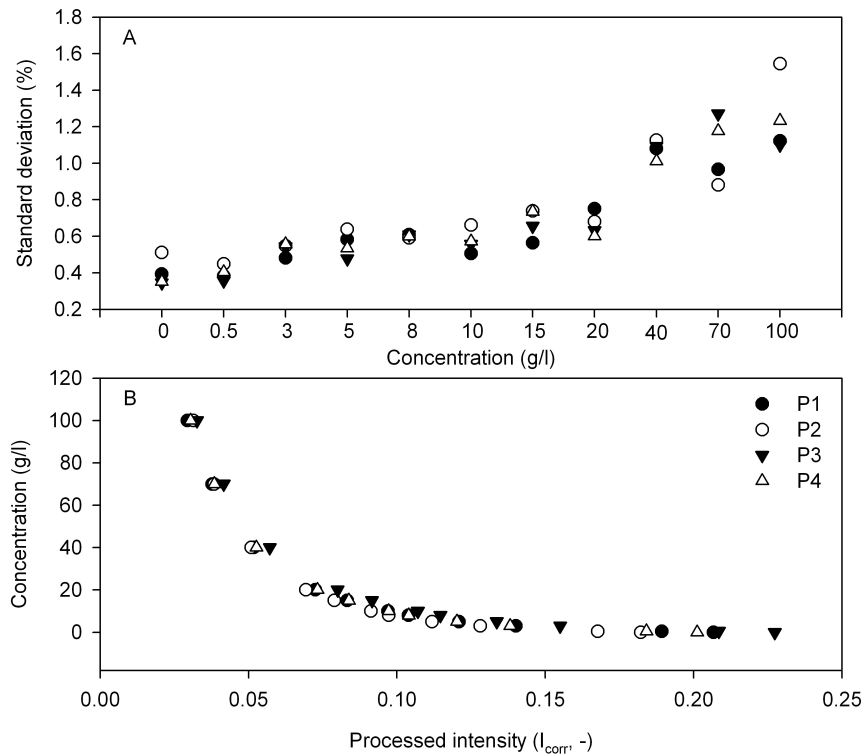


Figure II.5: A: Standard deviations of calibration images at observation point P1-P4 (Figure II.2); B: Intensity vs. concentration calibration plot of P1-P4.

Since we need to resolve concentration ranges from 0 to 100 g/l salt, 1 g/l dye concentration proves to be adequate to mark the maximum salt concentration of 100 g/l. The initial concentration (maximum concentration) of dye must be high enough so that, even with a large dilution, e.g. 0.5 g/l salt (corresponding to 0.005 g/l color), the plume can be differentiated optically from the ambient pore water. However, the maximum concentration needs to be below intensity saturation to enable the correct resolution of the high concentrations.

The parameters of the calibration curve had to be derived for each specific observation point (Table II.2). Thus, background levelling, as suggested in *Schincariol et al.* [1993] to compensate the spatially uneven lighting in the tank, was not necessary. This is an advantage because background levelling can reduce the dynamic range and adds noise to the original data [Russ, 1999]. Once the parameters of the standard curve are determined, they apply to all experiments if illumination and camera position is constant. This approach offers a computationally effective way to derive the high-resolution time series of concentrations.

II.1.1.4.5 Impact of lens flare on measured intensities

The basis of photometry in terms of concentration measurements of fluids is as follows: the brightness of two solutions is of equal intensity during calibration and all stages of the experiment, provided that the solutions are equally concentrated [Arnold et al., 1971]. However, this prerequisite could become perturbed due to the effects of lens flare. Rogers

[in Newman, 1976] stated: “one of the most usual problems created by white backgrounds is that of flare, caused by excessive reflection from white surface into the camera lens [...]” In porous media experiments, the artificial glass beads cause high reflection intensity and might generate flare effects, which have enough intensity to perturb the measurements. Regions of the photographed domain, which have a high dye concentration, might appear brighter because of the lens flare effects. That causes an underestimation of concentrations. We conducted a series of experiments in order to investigate the impact of lens flare effects on reflected intensity measurements (Table II.1).

In experiment E1, we successively placed four 70 cm long black cards one after another at the left side of the front window of our tank as illustrated in Figure II.6. Fifty images were made of each of the 4 steps.

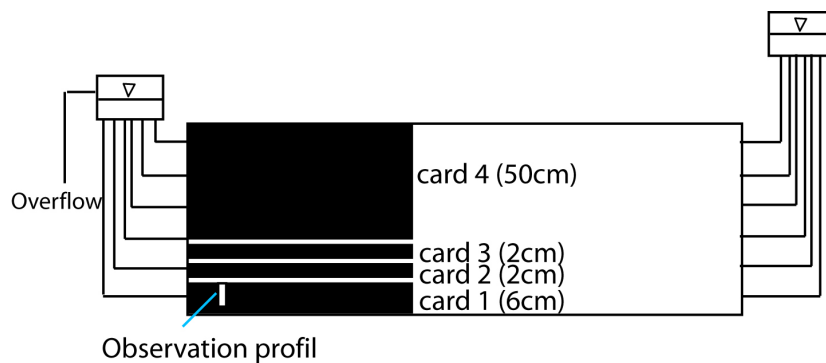


Figure II.6: Setup of the experiment E1. The cards are placed one after another right above each other, the heights of the cards are written in brackets.

Figure II.7 shows the decline of intensities along a vertical profile on card 1 (Figure II.6) for the four steps of the experiment. Adding cards 2 to 4 above card 1 decreases the reflection from the porous media above card 1 and therefore the effect of flare was reduced and made card 1 appear darker. The fourth stage of E1 is comparable to the calibration phase of E2 when the entire tank was filled with the dyed saltwater and lens flare significantly reduced. However, the dye tracer did not affect the largest portion of the tank during the flow phase of E2, and reflection intensity of the porous media was high. The shape of the salt body during the upcoming process of the flow phase of E2 is shown schematically in Figure II.1. Flare effects like in E1 can occur. In order to demonstrate the flare effects in E2 we derived intensities at a point 2 cm above the ground. The position of this measurement point is equal to the observation hole P1 of E3 (Figure II.2). Concentration profiles showed that the transition zone of the saltwater at the end of the equilibration phase, the second phase of the saltpool experiment, started 3cm above the ground. Therefore, the concentration is necessarily 100 g/l at 2 cm above ground. Since the salt body moves upwards to the outlet during the course of the experiment, no concentration changes are expected at this point. The intensities in Figure II.8 show a clear shift from 100 g/l calibration to the equilibration phase (approximately 7% increase in intensity) and from calibration to the flow phase (approximately 3%).

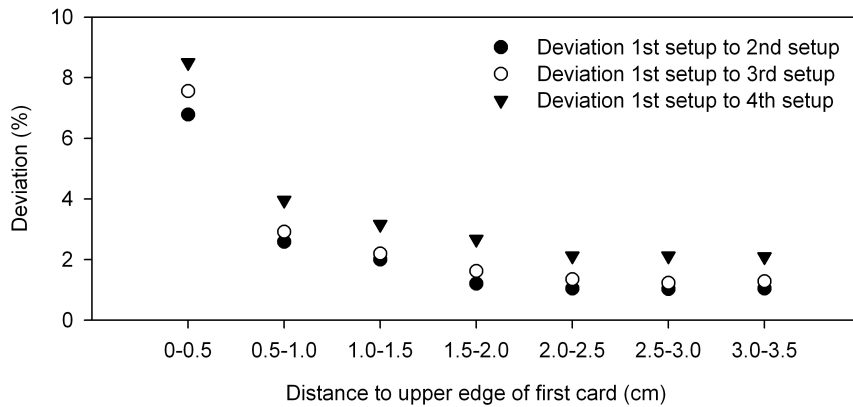


Figure II.7: Deviation (decline) of intensities taken at the profile in Figure II.6 when adding cards above card 1.

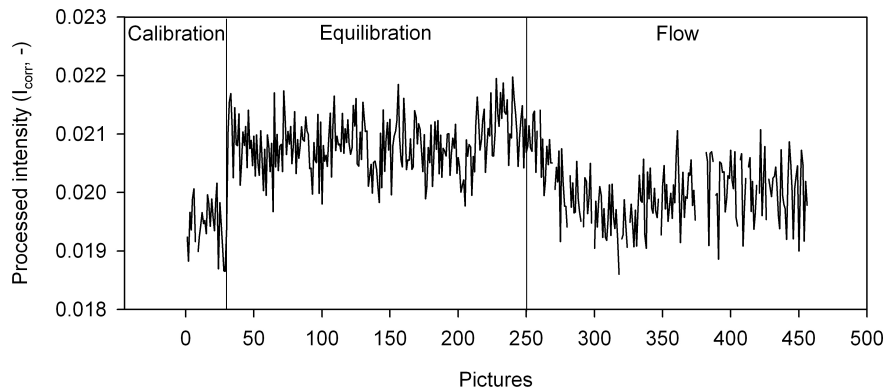


Figure II.8: Intensities of P1 (without mask) where no concentration changes occur during the flow phase of the density flow experiment (constant concentration of 100 g/l).

The intensity values decline during the upconing process of the flow phase. With the upconing of the saltwater, the dyed water affects a larger region around the observation point and reflection intensities are reduced. Therefore, the flare effects are reduced and the deviation between calibration intensities for 100g/l and the measured intensities during the flow phase decline to 3 %. This effect is comparable to the effects observed in E1 when the black cards are attached above card 1.

Rogers [in Neuman, 1976] suggested: “this problem [of lens flare] is largely overcome [...] and reduced to a minimum by masking the background area so that as little as possible is displayed.” Therefore, we attached a mask on the photographed domain with holes (1.5x1.5 cm²) at those points where we wanted to derive breakthrough curves for the third experiment E3 (Figure II.2). The upconing took place at the left side of the domain below the outlet. Therefore, as many observation points as possible were distributed in or close to the area of the expected saltwater upconing. Figure II.9 shows the intensities of P1 during all stages of the experiment.

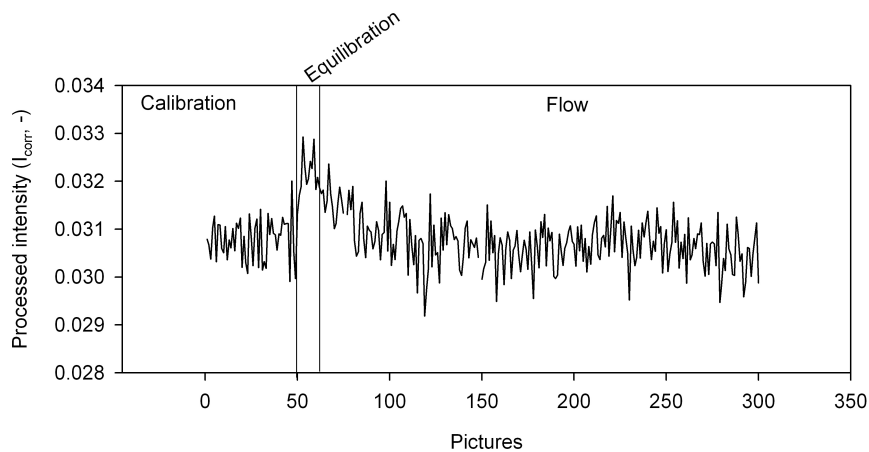


Figure II.9: Intensities of observation point P1 with mask.

It becomes evident that the effect of lens flare is strongly reduced, especially during the flow phase (0% intensity deviation between calibration and flow phase). However, there is still an approximately 3% deviation between the intensities of the calibration and the equilibration phases of E3. We attribute this effect to the impact of the observation points close to P1. These were not influenced by the dye and therefore reflection intensity was high and, hence, could cause lens flare effects. During the course of the experiment the salt plume rose and the points in the neighbourhood of P1 appeared darker, which reduced flare effects during the flow phase comparable to the effects observed in E1 and E2. Therefore, the attached mask helps to reduce flare effects.

The experiment E4 was conducted to estimate the error caused by flare effects. Solutions of predetermined 5, 40, and 100 g/l (salt+dye) were progressively pumped into the tank from the bottom upward. Seven different filling levels with a horizontally planar salt water front were established so that all observation points in the same horizontal line were fully immersed in the solution. In order to estimate the impact of lens flare we derived intensities at all observation points visible in Figure II.2 (not only P1-P4) for all filling levels of the experiment of the three solutions and analyzed their development during the course of the experiment. E4 revealed that the error depends on (i) the concentration of the solution, and the error increases with increasing concentration; and (ii) the intensity of the neighboring observation points, while the error decreases with decreasing intensity. The maximal deviation of intensities for the 100 g/l solution in E4 amounted to 3%. This experiment shows only 1D vertical movement of the brine, and 2D plume shapes such as in the saltpool experiments E2 and E3 do not occur. Therefore, we used the results of E4 only to estimate the error caused by lens flare effects, and not to correct the measured data. We assumed a maximal error of 3% of overestimation (compared to calibration) of the intensities during the flow phase caused by lens flare effects for E3 with the attached mask.

II.1.1.4.6 Error assessment

In order to estimate the precision of the photometric method, we calculated the standard deviation of the calibration images for each calibration step (Figure II.5A). The maximum deviation, which we consider as the accuracy of the measured intensities, occurs for salt concentration of calibration steps 70g/l or 100 g/l. From the above

discussion, we know that there is an additional error of +3% in the measured intensities due to the lens flare effect. Therefore, the concentrations are given with confident limits (see Figure II.15). The lower boundary is calculated from the processed intensity I_{corr} plus standard deviation (%), whereas for the upper boundary I_{corr} minus 3% and standard deviation is used to derive concentrations. The intensities are converted to concentrations using the second order exponential equation (II.4). This propagates the intensity error non-linearly to the concentration error. The mass balances in experiment E5 can also be calculated to test the performance of the image analysis approach based on the given mass of salt entering the domain and the mass determined by image analysis at different time steps (Figure II.10, Table II.1).

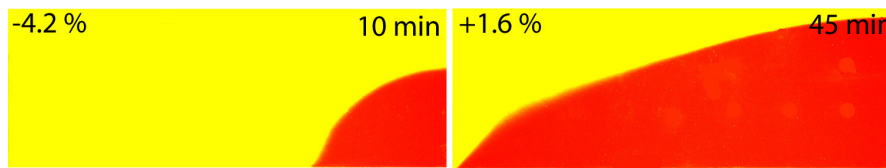


Figure II.10: Mass balance analysis of E5 after 10 min and 45 min.

The image analysis takes into account the porosity and the depth of the tank. The impact of lens flare becomes more pronounced if a small portion of the domain is filled with the dark solution. If the tank is filled with the dark solution the effect should be reduced. In E5, the dye-salt solution enters the domain over one inlet at the edge of the tank with a constant well-known flow rate. The concentration is 100 g/l of NaCl. An image is taken every 30 sec and we analyzed the images after 10 and 45 minutes. Figure II.10 shows the spatial distribution of the saltwater (red). The 10 min image delivers an underestimation of the total mass of -4.2% compared to the mass entering the domain. This is within the range of expected lens flare error. After 45 min, the bright region of the tank is significantly reduced and the mass error accounts for 1.6% indicating that the method overestimates the total mass. On the basis of this analysis, the calibration parameters of Equation II.4 can be considered reliable, and possible errors can be explained by the impact of lens flare.

II.1.1.5 Concentration determination with resistivity measuring cells (RMC)

II.1.1.5.1 Technical setup of the RMC system

Each RMC consists of five gilded stainless steel electrodes (diameter 0.4 cm, length 13 cm, Figure II.11). We used gilded electrodes, because uncontrollable fluctuations in the resistivity measurement occur with ungilded stainless steel electrodes. The electrodes are equally spaced 1 cm around the center electrode and mounted on a Plexiglas flange. They are installed perpendicular to the flow direction through the back wall of the tank.

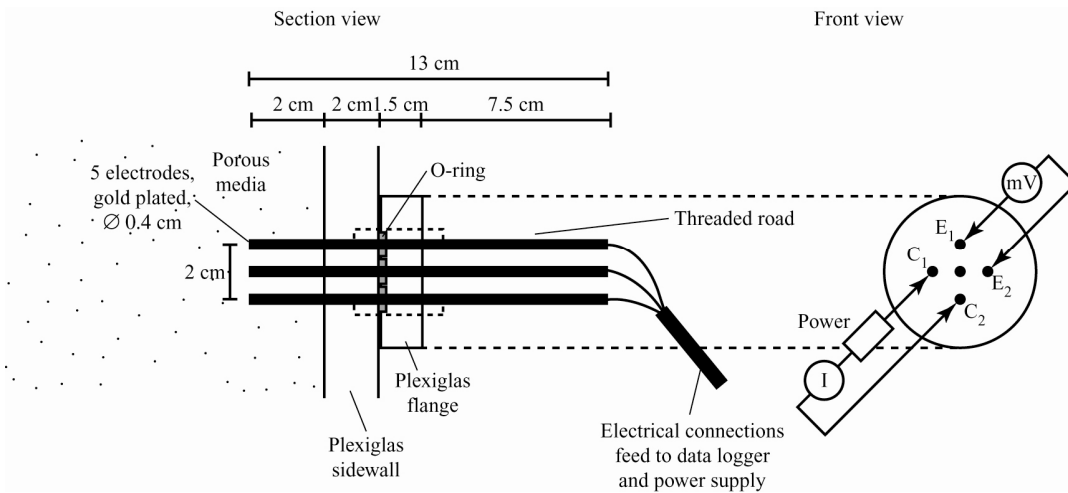


Figure II.11: Electrode array with two current electrodes (C_1 and C_2), two potential electrodes (E_1 and E_2) and grounding in the center of the array.

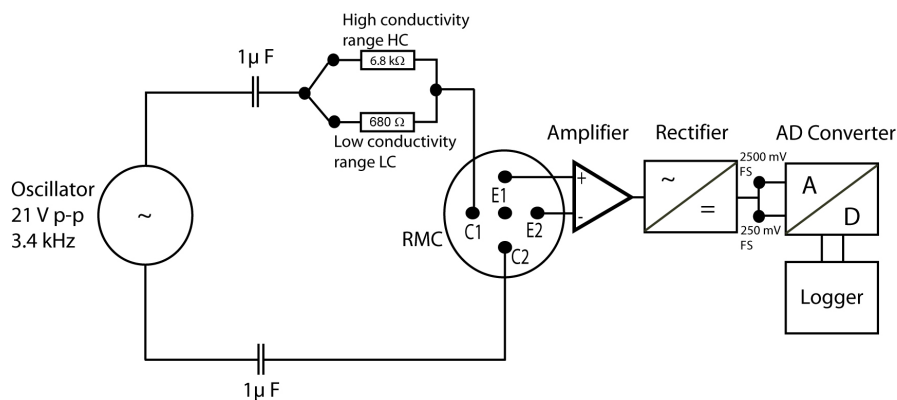


Figure II.12: Construction plan of the RMC system.

Figure II.12 shows the schematic construction plan of the entire RMC system. The system involves measuring the output voltage between the electrodes E_1 and E_2 while electrical current is caused to flow through the porous media between the outer pair of electrodes C_1 and C_2 . The grounding electrode is in the center. The measuring principle is based on a 4-electrode resistivity measurement technique, where the current is supplied through a very precisely regulated sinusoidal oscillator signal. The measured AC voltage is rectified through a synchronous demodulator in phase to the oscillator. The resulting DC output voltage was recorded utilizing a micro-logger and a relais based multiplexer to measure all the RMCs sequentially. An alternating current was applied in all measurements to minimize polarization within the cell and to prevent movement of the ions due to the presence of a voltage potential.

Since the measurement has to cover a wide range of voltage values due to the high salt concentrations, two different input voltages are used at each time step. This enables measurements to be made in two measurement ranges, one for the high concentration, referred to as MR1, and the other for low concentrations, MR2. As this measuring method is sensitive to temperature variations, temperature sensors (YSI 4006; accuracy $\pm 0.01^\circ\text{C}$) are also inserted into the porous medium.

II.1.1.5.2 Electrode arrays

Various electrode arrays were tested in preliminary experiments in a small container (35x16x9 cm³) filled with saturated porous media. Figure II.13 shows the three investigated arrays. In array 1 all electrodes are uniformly placed in a line with the grounding electrode in the center.

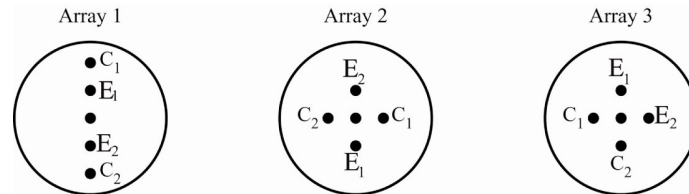


Figure II.13: Evaluated sets of electrode arrays.

Array 2 is a cross-placement of $C_{1,2}$ (current electrodes) and $E_{1,2}$ (potential electrodes) while in array 3 input and output electrodes are placed in an adjacent position (parallel). In preliminary tests to evaluate the best array setup, the three different arrays were also rotated clockwise to study the influence of flow direction of the saltwater front. Array 1 was rotated clockwise by 90°, array 3 was rotated clockwise by 90°, 135°, 180° and 315°. A total of 4 tests were carried out. The setups were evaluated by measuring a successively rising saltwater front in the small experimental tank. Figure II.14 shows the measured breakthrough curves of output voltages of the 8 different arrangements.

The breakthrough curves of array 1 and its clockwise rotated (by 90°) setup clearly show the dependence of these alignments on the flow direction of the salt front.

There is a temporal shift between both curves, and array 1 even shows a plateau of the curve. Array 2 delivers no analyzable breakthrough curve. In this setup, both electrodes should detect the same voltage under homogeneous conditions. The fact that a voltage change is visible might be due to local concentration differences or asymmetric manufacturing of the RMC. Array 3 and its rotated setups deliver curves less dependent on the flow direction of the front and a realistic shape of the curve is observed. As the result of these findings, we chose array 3 for measuring the resistivity.

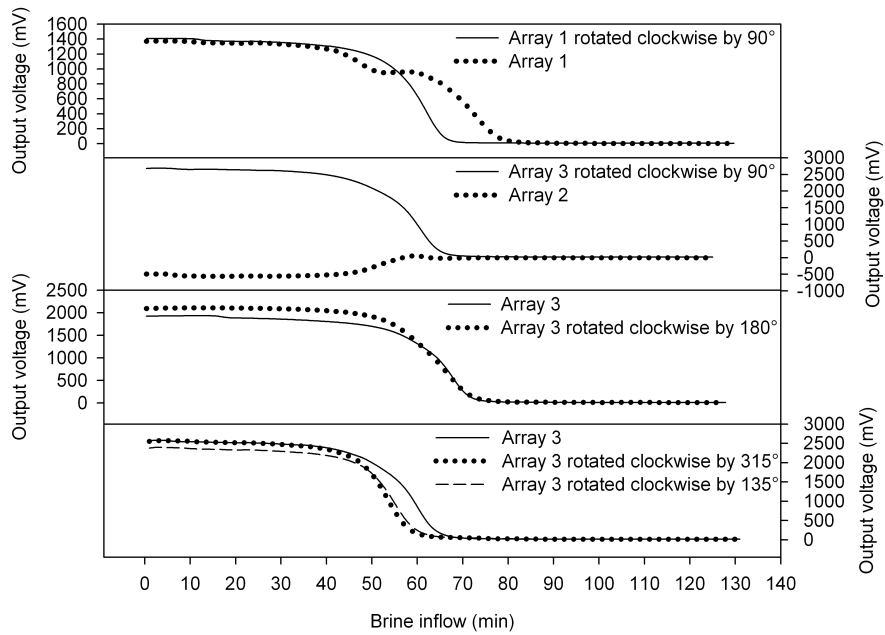


Figure II.14: Measured breakthrough curves of output voltage (mV) for the different sets of electrodes and their clockwise-rotated arrangements.

II.1.1.5.3 Calibration of the RMC

The resistivity measured between two electrodes is a function of the porous material, porosity, temperature, geometrical arrangement of the electrodes, state of gold coating and the ion concentration [Telford *et al.*, 1990]. During an experiment, all factors apart from the ion concentration are kept constant and the measured resistivity can be related to the concentration of the solution surrounding the electrodes. The output voltages of the two measuring ranges, MR1 and 2, are correlated with the concentrations using specifically fitted power laws for each RMC and measurement range. Figure II.15 shows, by way of example, the calibration curves for MR1 and 2 of the RMC located at observation point P2 (Figure II.2).

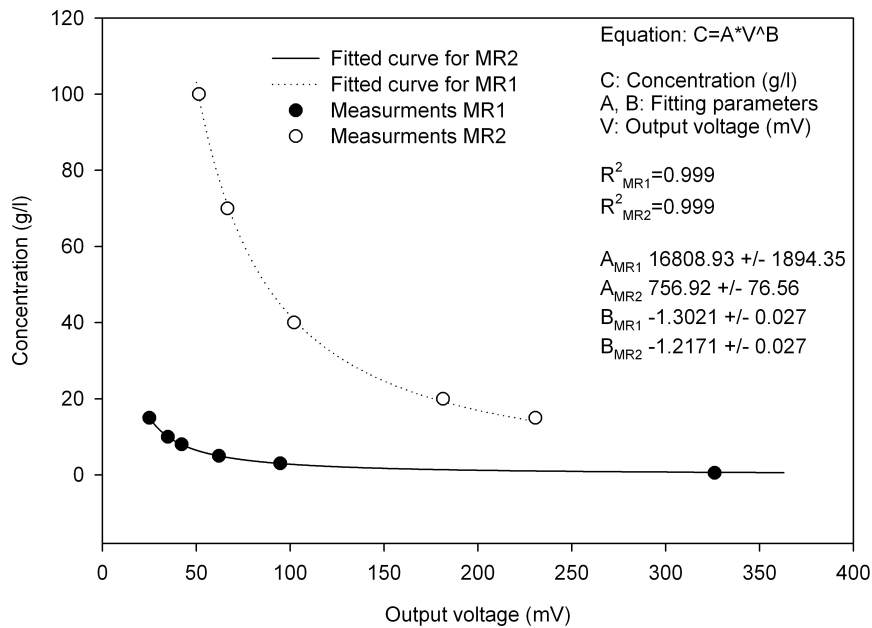


Figure II.15: Calibration curves for the RMC at P2.

The errors associated with the concentration consist of two parts: measurement errors and parameter errors associated with the calibration curves. The measurement errors are small and the maximum error found during the calibration experiment was +/- 0.5%. The errors associated with the calibration curve are within the range of -1.5 to +2.5 %. Since the calculated error is small we do not show error bars in Figure II.16. Typically, systematic errors are caused by temperature fluctuations. However, these can be minimized for laboratory experiments due to controlled room and water temperatures.

II.1.1.6 Comparison of the two methods

For direct comparison of the RMC method and the image analysis method we derived concentrations from the images at the position of the centre electrode of the RMC at observation points P2 and P3 (Figure II.2). The comparison reveals that both independent methods reproduce the expected concentrations of 100 g/l at P2 when the saltwater rises, although the RMC shows a slightly earlier reaction than the image analysis approach, which can be explained by the larger measurement volume of the RMC (Figure II.16).

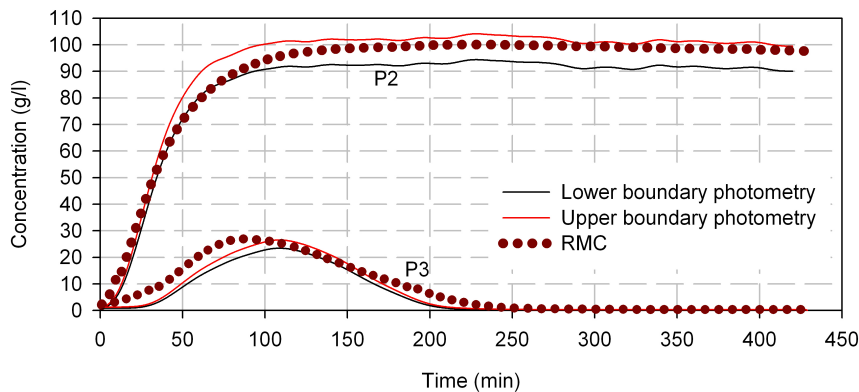


Figure II.16: Breakthrough curves of P2 (100 g/l) and P3 (max. 30 g/l) derived from electrodes and from photometric method. The solid lines represent the range of error of the photometric method.

However, if the electrode is placed within the transition zone, where steep concentration gradients exist, the two methods differ significantly due to the different measurement volumes, as is the case at P3 (Figure II.16). The RMC measures an apparent resistivity of the environment around the electrodes. Thus, it is not a point measurement but an integral value. The measurement volume strongly depends on the ion concentration distribution and on the resistivity contrast during the experiment. Therefore, the measurement volume is not constant throughout the course of the experiment. This problem is the major drawback of the RMC method especially for measuring points within the transition zone, where a concentration gradient occurs within the measuring volume of the RMC. However, especially for points such as P2 where the electrodes are surrounded by a uniform concentration, this problem is of minor importance. A numerical simulation of the resistivity field, the current density and of the voltage at the electrodes for heterogeneous resistivity distributions could enable the determination of the measurement volume. This work was beyond the scope of this study but we highly recommend further investigation in this field.

II.1.1.7 Conclusions

In this study we present a photometric methodology, which enables effective computation of high-resolution time series of plume concentrations. The method is capable of treating a large number of images since only one optimization of the intensity vs. concentration standard curve is required. Once the parameters of this curve are known for the observation point they can be used for a series of experiments, if the camera position and the tank position do not change and the images fit on a pixel-by-pixel basis. Beside the breakthrough curves contour lines of concentration can be determined. The resolution of the observation point is crucial for the precision of the measured intensity values. Therefore, we suggest a statistical analysis for each experimental setup to determine the adequate resolution. A major source of error is the impact of lens flare. High reflections of bright regions of the photographed domain, which are not influenced by the dye, could generate flare effects that increase the measured intensity of dark, dye-influenced regions of the tank. This leads to an underestimation of the concentration. Attaching a mask at the

front window of the tank, which reduces the percentage of bright regions, can minimize this effect. However, information is available in this case only at the predetermined points, i.e., the observation holes in the mask. Since the mask itself influences the brightness of the observation holes, both the calibration and the flow experiments have to be conducted using the same setup with the mask. This minimizes the flexibility of the experiment in order to run different experiments with changing boundary conditions and therefore with different plume patterns.

Nevertheless, the precision of the measurement is high even without the mask. A successive filling of the tank with predetermined concentrations of salt-dye solutions enables an estimation of the error caused by flare effects. The successive filling gradually reduced the percentage of bright regions and therefore decreased the impact of flare effects at the observation points. The deviation between the measured intensity of the entirely filled tank and the partly filled tank was determined as maximal error.

In this study, the light reflection technique was used instead of the transmission technique because:

1. The back of the tank holds devices to measure resistivity, temperature and pressure;
2. Applicability and limitations of the widely used reflection method need to be assessed.

For future research, we suggest a direct comparison of the light reflection and the transmission techniques.

The resistivity measurement system provides highly precise measurements of output voltages, which can be translated into concentrations using a power law. The major perturbations of the measurement are temperature changes, which can be avoided in laboratory scale experiments. However, the main drawback of the resistivity method is the unknown measurement volume. For the evaluation of numerical codes it is crucial to know the exact measurement volume, especially in an intermediate scale experiment where significant variations in concentrations occur, even over a few centimetres. Therefore, we consider the image analysis approach as more suitable for deriving breakthrough curves for benchmarking numerical codes. The electrodes, however, can be used to cross-check the results of the image analysis method at points of uniform concentration distribution. Further, the methodology is useful in 3D experiments of large tank volumes to determine concentrations at points within the tank. A numerical analysis of the measurement volume of the RMC system could help to improve the applicability of the technique for detailed laboratory-scale flow experiments. Regarding hydrogeological field observations, the RMC method could be further developed for multi-level monitoring of electrical conductivities in the context of highly saline groundwaters mixing with groundwaters of low salinity. This is of special interest in active evaporite subsidence and/or forced groundwater circulation systems (active pumping). Resistivity tomography could be tested and compared with the imaging method – viewing the results of the imaging method as ‘true’ system behaviour.

II.1.1.8 References

Arnold, C., Rolls, P., Stewart, J.: Applied photography. The Focal Press, ISBN 0 240 50723 1, 1971.

- Barth, G.R., Illangsekare, T.H., Hill, M.C., Rajaram, H.: A new tracer-density criterion for heterogeneous porous media. *Water Resour. Res.* 37, 21– 31, 2001.
- Catania, F., Massabo, M., Valle, M., Bracco, G., Paladino, O.: Assessment of quantitative imaging of contaminant distributions in porous media. *Exp Fluids* 44, 167–177, 2008.
- Corapcioglu, M. Y., Chowdhury, S., Roosevelt, S. E.: Micromodel visualization and quantification of solute transport in porous media. *Water Resour. Res.* 33, 11, 2547–2558, 1997.
- Danquigny, C. Ackerer, P., Carlier, JP.: Laboratory tracer tests on three-dimensional reconstructed heterogeneous porous media. *J. Hydrol.*, 294 (1-3). 196-212 Sp. Iss. SI JUL 15, 2004.
- Detwiler, R. L., Rajaram, H., Glass, R. J.: Solute transport in variable-aperture fractures: An investigation of the relative importance of Taylor dispersion and macrodispersion. *Water Resour. Res.* 36, 7, 1611– 1625, 2000.
- Goswami, R., Clement, P.: Laboratory-scale investigation of saltwater intrusion dynamics. *Water Resour. Res.* 43, W04418, 2007.
- Hassanizadeh, S. M., Leijnse, A.: A non-linear theory of high-concentration-gradient dispersion in porous media. *Advances in Water Resour.* 18, 4, 203-215, 1995.
- Huang W., Smith C.C., Lerner D.N. Thornton S.F., Oram A.: Physical modelling of solute transport in porous media: evaluation of an imaging technique using UV excited fluorescent dye. *Water Res* 3, 7, 1843–1853, 2002.
- Jones E.H., Smith C.C.: Non-equilibrium partitioning tracer transport in porous media: 2-D physical modelling and imaging using a partitioning fluorescent dye. *Water Res* 39, 20, 5099–5111, 2005.
- McNeil, J.D., Oldenborger, G.A., Schincariol, R.A.: Quantitative imaging of contaminant distributions in heterogeneous porous media laboratory experiments. *J. Contam. Hydrol.* 84, 36-54, 2006.
- Oostrom, M., Dane, J.H., Guven, O., Hayworth, J.S.: Experimental investigation of dense solute plumes in an unconfined aquifer model. *Water Resour. Res.* 28, 2315– 2326, 1992.
- Oostrom, M., Hofstee, C., Lenhard, R.J., Wietsma, T.W.: Flow behavior and residual saturation formation of liquid carbon tetrachloride in unsaturated heterogeneous porous media. *J. Contam. Hydrol.* 64, 93– 112, 2003.
- Oswald, S., Kinzelbach, W., Greiner, A., Brix, G.: Observation of flow and transport processes in artificial porous media via magnetic resonance imaging in three dimensions. *Geoderma* 80, 417– 429, 1997.

- Oswald, S., Kinzelbach, W.: Three-dimensional physical benchmark experiments to test variable-density flow models. *J. Hydrol.* 290, 22–42, 2004.
- Rahman, A., Jose S., Nowak W., Cirpka, O.: Experiments on vertical transverse mixing in a large-scale heterogeneous model aquifer. *J. Contam. Hydrol.* 80, 130– 148, 2005.
- Rogers, G.: Photography in paediatrics. Published in photographic techniques in scientific research, Volume 2, edited by Newman, A.. Academic Press, ISBN 0 12 517960, 1976.
- Russ, J.C.: The image processing handbook, 3rd edn. CRC, Boca Raton, 1999.
- Schincariol, R.A., Herderick, E.E., Schwartz, F.W.: On the application of image analysis to determine concentration distributions in laboratory experiments. *J. Contam. Hydrol.* 12, 197–215, 1993.
- Silliman, S.E., Simpson, E.S. Laboratory evidence of the scale effects in dispersion of solutes in porous media. *Water Resour. Res.* 23, 1667– 1673, 1987.
- Silliman, S.E., Zheng, L., Conwell, P.: The use of laboratory experiments for the study of conservative solute transport in heterogeneous porous media. *Hydrogeol. J.* 6, 166– 177, 1998.
- Simmons, C.T., Pierini, M.L., Hutson, J.L.: Laboratory investigation of variable-density flow and solute transport in unsaturated–saturated porous media. *Transp. Porous Media* 47, 15– 244, 2002.
- Swartz, C.H., Schwartz, F.W.: An experimental study of mixing and instability development in variable-density systems. *J. Contam. Hydrol.* 34, 169– 189, 1998.
- Telford, W.M., Geldart, L.P., Sheriff, R.E.: Applied geophysics. – 2nd edition. Cambridge University Press, ISBN 0-521-33938-3, 1990.
- Theodoropoulou M.A., Karoutsos V., Kaspiris C., Tsakiroglou C.D.: A new visualization technique for the study of solute dispersion in model porous media. *J Hydrol* 27, 1–4, 176–197, 2003.
- Wildenschild, D., Jensen, K.H.: Laboratory investigations of effective flow behavior in unsaturated heterogeneous sands. *Water Resour. Res.* 35, 17–27, 1999.

II.2 Measurement of salt concentrations in 2D flow tanks using transmission or reflection intensity measurements

Paper published in *Experiments in Fluids*

Comparison of light transmission and reflection techniques to determine concentrations in flow tank experiments

Konz, M.⁽¹⁾; Ackerer, P.⁽²⁾; Huggenberger, P.⁽¹⁾; Veit, C.⁽²⁾

⁽¹⁾Department of Environmental Sciences, University of Basel, Institute of Geology, Applied and Environmental Geology, Basel, Switzerland

⁽²⁾ Université Louis Pasteur, Institut de Mécanique des Fluides et des Solides, CNRS, UMR 7507, Strasbourg, France

II.2.1 Comparison of light transmission and reflection techniques to determine concentrations in flow tank experiments

II.2.1.1 Abstract

Transmissive and reflective intensity measurements for visual concentration determinations in 2D flow tank experiments were compared and evaluated for their applicability in the study of flow and transport phenomena. A density-dependent heterogeneous flow experiment was conducted and transmission and reflection images of the dyed saltwater plume were analyzed. A single light source and dark curtains forced the light to pass through the porous media only, thus facilitating the transmission measurements. The reflection images delivered a more homogeneous spatial illumination than the transmission images. Major perturbations of the transmission images were lens flare effects and light dispersion within the bead-water-Plexiglas system which smear the front of the plume. Based on the conducted evaluation of transmissive and reflective intensity measurements, the reflection data delivered more reliable intensity values to derive solute concentrations in intermediate scale flow tank experiments.

II.2.1.2 Introduction

Laboratory scale flow tank experiments are increasingly used to investigate flow and transport phenomena in porous media. In 2D experiments spatial and temporal measurements of plume concentration distributions have been made by direct non-intrusive optical observations of dye tracers. The photometric technique is based on Lambert Beer's law assuming an exponential decline of light intensity with increasing dye concentration. The intensity can be measured either as light transmitted through the three-phase system consisting of glass beads, freshwater or dyed water and the Plexiglas panes, or the intensity values can be taken from reflected light. For both techniques the relationship between intensity and concentration needs to be determined by calibration.

Most intermediate scale experiments used reflected light for image analysis [e.g. *Schincariol et al.* 1990; *Oostom et al.* 1992; *Swartz and Schwartz* 1998; *Wildenschild and Jensen* 1999; *Simmons et al.* 2002; *Rahman et al.* 2005; *McNeil et al.* 2006; *Goswami and Clement* 2007; *Konz et al.* 2008a; *Konz et al.* 2008b]. The reflection measurement can be conducted with non-transparent porous media material and with thick flow tanks that prevent light transmission. Image noise, fluctuations in brightness, and reflections from the surroundings can have a negative impact on the reflection measurements. *Konz et al.* [2008a] showed the impact of lens flare effects on reflection intensity measurements in homogeneous porous media flow experiments. The flare effect artificially increases the intensity of dark regions because of light scattering within the lens system of the camera. This leads to an underestimation of concentrations.

The light transmission technique to measure emitted light from behind the flow tank opposite to the light source is normally used in micromodel experiments with thin flow tanks [e.g. *Corapcioglu et al.* 1997; *Detwiler et al.* 2000; *Huang et al.* 2002; *Theodoropoulou et al.* 2003; and *Jones et al.* 2005]. An excellent literature review of transmission experiments and data processing techniques can be found in *Catania et al.* [2008]. Since only the transmitted light is recorded for concentration determination, reflections from the surroundings can be excluded. The use of transmission intensities has

the advantage that migration effects are averaged over the width of the flow model. Therefore, possible 3D effects are less severe than with reflection data. However, light scattering within the system of glass beads, water and Plexiglas leads to light dispersion [Huang *et al.* 2002; Rezaeehad *et al.* 2006]. This effect does not arise if reflection intensities were imaged to derive concentrations.

The aim of this study is to compare the light reflection and transmission techniques and evaluate their applicability to intermediate scale flow tank experiments with heterogeneous porous media. The comparison focuses on the impact of (i) illumination homogeneity, (ii) lens flare effects, and (iii) light dispersion within the flow tank, on the intensity measurements.

II.2.1.3 Materials and methods

II.2.1.3.1 Materials

Flow tank: The flow tank (internal dimensions: 158 cm length x 98 cm height x 4 cm depth) used for the experiments was constructed of 2 cm thick Plexiglas sheets (Figure II.17). Tension pins prevented deformation of the sidewalls of the tank allowing for maximum viewable area. The bottom of the tank had six openings (diameter 0.9 cm) and another nine openings each were placed at the sides of the flow tank. The openings could be connected either to a peristaltic pump or to reservoirs in order to meet the targeted boundary conditions.

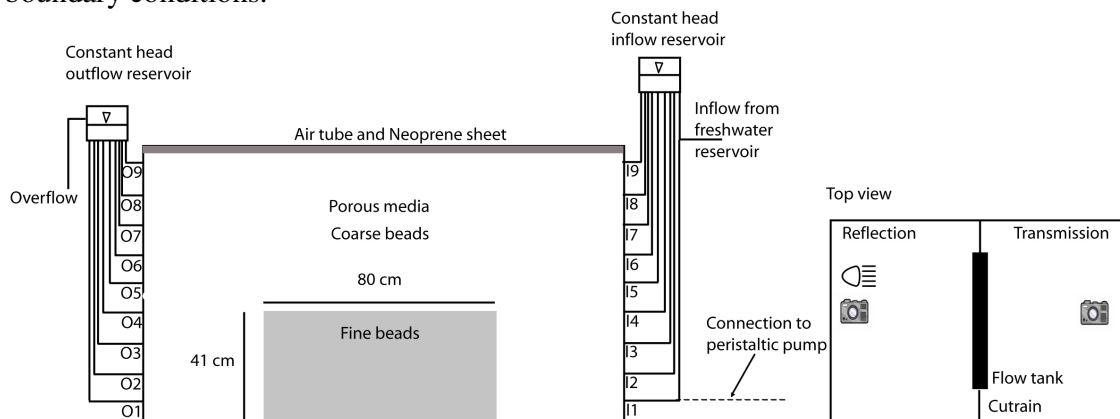


Figure II.17: Experimental flow tank.

Porous matrix: The tank was filled with two different glass bead types in order to achieve a heterogeneous porous media. The coarse beads had a diameter of 2 to 2.4 mm and the fine beads' diameter was between 0.5 and 0.7 mm. Figure II.18 shows the heterogeneous packing of the tank with the block of fine beads in the center of the tank. The tank was packed under fully saturated conditions and the glass beads were poured into the tank in order to avoid air trapping. The de-ionized water used for the experiments was kept constant at 20°C in two 1700l freshwater reservoirs to prevent degassing in the porous media. Water temperature was measured in the outflow reservoir after it passed the tank and no relevant changes (+/- 1.5 °C for all experiments and calibration) were detected. Therefore, degassing due to temperature changes can widely be excluded. Further, no formation of air bubbles could be observed on the tank walls at any time. The two zones

were divided by stainless steel emplacement dividers, which were removed once the targeted height of the fine porous media block was reached.

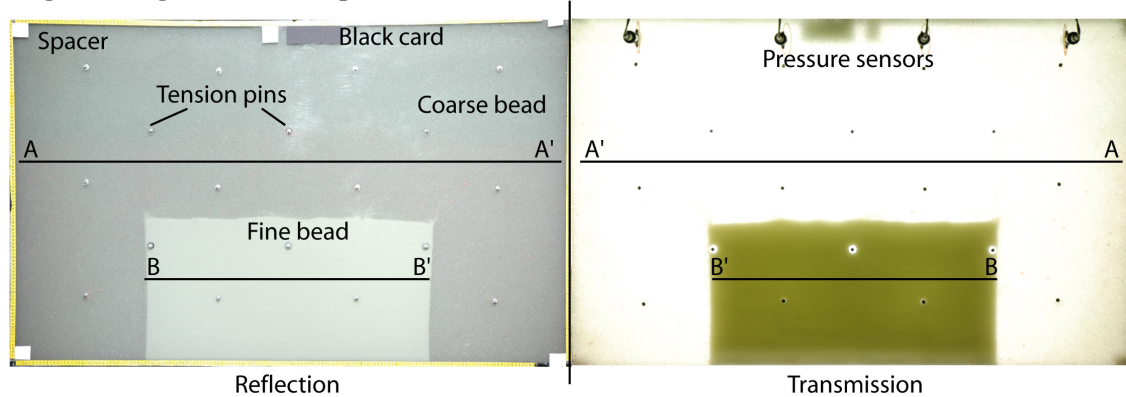


Figure II.18: Comparison of transmission and reflection images and position of profiles in Figures II.5 (AA') and II.12 (BB').

Light source: A single light source was placed at a distance of 3 m away from the tank. The light source (Kobold-Licht, DFR200, 200W, 5600K) was adjusted and checked with a luxmeter to minimize spatial lighting non-uniformity. However, it was not possible to avoid lighting non-uniformity and a higher intensity remained in the center of the image. The effects are shown in Figure II.21. Opaque, black curtains surrounded the entire tank. This setup forced the light to pass only through the porous media, a prerequisite for light transmission measurements.

Tracer: Cochineal Red A (E124) was used as tracer. This food dye is non-sorbing, nonreactive with NaCl in concentrations used for the experiment [Rahman *et al.*, 2005 and our own batch experiments]. The maximum absorption wavelength of the red dye is 507 nm. In order to test the tracer for degradation or optical decay of dye, the tank was filled with a dyed saltwater solution and images were taken over a period of 14 hours. Intensity measurements were analyzed and revealed that the intensity values remained on a constant level. Additional photometric analyses using a spectrometer (Shimadzu UV-1700 Pharma Spec) to measure the intensities of different dye-saltwater solutions exposed to the same lighting proved that there is no degradation or optical decay of dye over a period of up to 7 days.

Camera: The images were recorded by two Nikon digital cameras (D70 and D80). The cameras deliver 12-bit images.

II.2.1.3.2 Methods

Image acquisition and image processing: Schincariol *et al.* (1993) and McNeil *et al.* (2006) outlined that the same image analysis techniques can be used for transmitted and reflected light. The image analysis method used here, is discussed in Konz *et al.* (2008a) and the interested reader is referred to this publication for a detailed description of the image processing method. The procedure consists of: (i) data conversion to 16-bit tif images (65536 intensity values per channel of the RGB color space) with the freeware ddraw (<http://cybercom.net/~dcoffin/dcrow>) to preserve the information of the 12-bit raw data, (ii) selection of the most sensitive green channel [Konz *et al.* 2008a; McNeil *et al.*

2006], (iii) determination of measurement area, (iv) correction of fluctuations in brightness using attached black cards, in the case of reflection measurements, (v) construction of a curve that relates intensities to concentrations from calibration images and determination of function parameters for the mathematical formulation of the curve expressed by:

$$C_{i,j}(t) = A1_{i,j} \exp(I_{i,j}^{corr}(t)/b1_{i,j}) + A2_{i,j} \exp(I_{i,j}^{corr}(t)/b2_{i,j}) + D_{i,j} \quad (\text{II.5})$$

where $C_{i,j}(t)$ is the concentration at time t , $A1_{i,j}, A2_{i,j}, D_{i,j}, b1_{i,j}, b2_{i,j}$ are parameters, $I_{i,j}^{corr}$ is the brightness-corrected intensity at time t , and i and j are the coordinates of the pixels. The parameters have to be determined for each observation point in order to account for illumination heterogeneities.

Calibration and determination of appropriate camera settings: To establish the relationship between reflected/transmitted image intensity and salt concentration in Equation II.5, the entire tank was filled with solutions of predetermined saltwater-dye concentrations. The dyed saltwater solutions were pumped into the tank in a sequential order from low-density solutions to high-density solutions. Fifty images of transmission and reflection intensities were taken of each calibration solution to get a statistically significant measure of the dye intensities. The median of the 50 images was used to calculate the calibration intensity [Konz *et al.*, 2008a]. Since concentration ranges from 0 to 100g/l salt need to be resolved, 1g/l dye concentration proves to be adequate to mark the maximum salt concentration of 100g/l [Konz *et al.* 2008a]. The initial maximum dye concentration must be high enough so that, even with a large dilution, the plume can be differentiated optically from the ambient pore water. However, the maximum concentration needs to be below intensity saturation to enable the correct resolution of the high concentrations. In order to find the appropriate camera settings, different parameter sets of shutter speed, aperture and ISO number were tested. The ability to resolve intensity differences between the 70 and 100g/l solutions defines the adequate parameter set. Since the brightness differences between the two bead glasses are high, the parameter set used for the experiments represents a compromise to determine concentrations of both zones with one camera. The camera parameters must be constant and should not vary automatically so that the brightness corrected intensity variations can only be related to variations in dye concentration. Figure II.19 shows the calibration curves of intensity vs. concentration for points in the fine and the coarse zone using a shutter speed of 2 sec, aperture of 4.5 and ISO200 for transmission and 1 sec, aperture of 8 and ISO200 for reflection. The intensities of the reflection measurements are brightness corrected (see point (iv)), therefore the values in Figure II.19 are smaller than the transmission data.

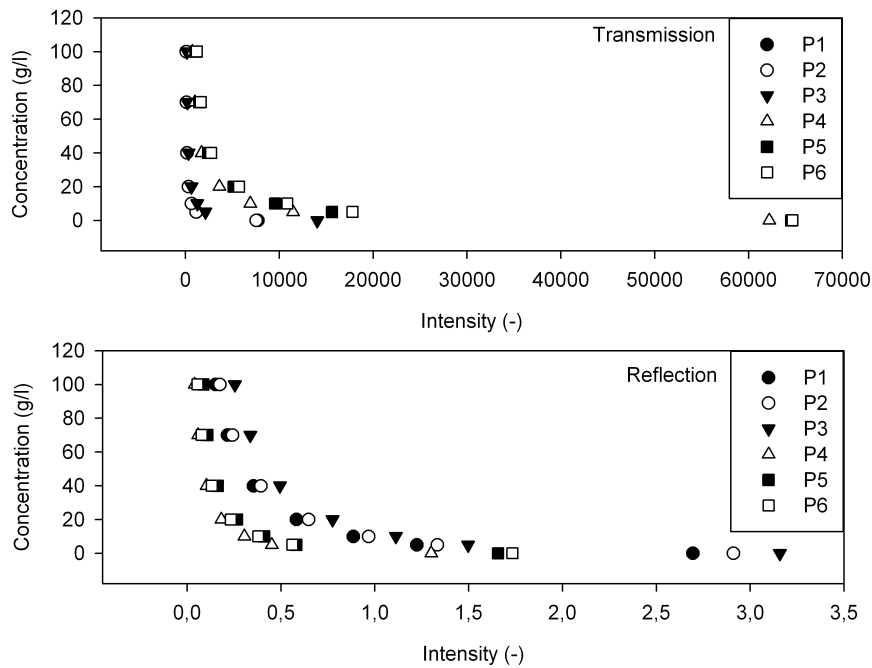


Figure II.19: Calibration curves for points of transmission and reflection images. P1-P3 are placed in the fine beads, P4-P6 in the coarse beads.

II.2.1.3.3 Experimental procedure

A density dependent flow experiment, E1, shows the applicability and limitations of the transmissive and reflective measurement techniques to derive concentrations of heterogeneous flow tank experiments. The flare effects in the camera lenses [Rogers 1976; Konz *et al.* 2008a] and light dispersion due to scattering within the 3-phase system of beads, water/dye and Plexiglass [Huang *et al.* 2002; and Rezaeezhad *et al.* 2006] represent crucial perturbations of optical measurements. The experiments E2 and E4 were conducted in order to demonstrate the impact of these effects on intensity measurements in our experimental setup. Experiment E3 shows a possible way to minimize the effect of lens flare.

Density-driven flow experiment (E1): The dyed solute of 100g/l salt marked with 1g/l dye was pumped into the domain through I1 and O8 was used as outlet (Figure II.17). Therefore, the tank continuously filled with solute and the bright region was reducing during the course of the experiment.

Assessment of lens flare effect (E2): Three black cards were placed sequentially above each other at the transmissive side of the tank to reduce the bright region of the tank (Figure II.20). Images were taken from each step and the development of intensity profiles of the first card was observed.

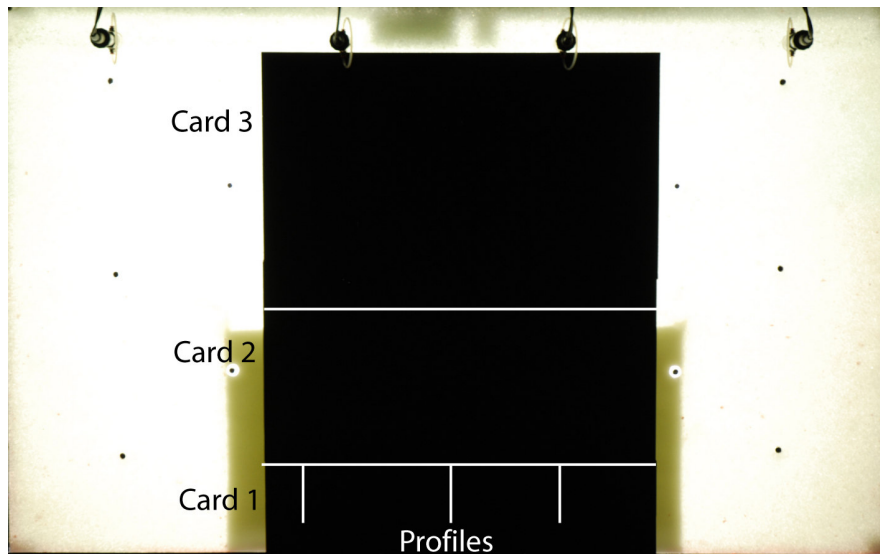


Figure II.20: Black card experiment, E2, to show the impact of lens flare effects on the intensity measurements along profiles of Card 1.

Density-driven flow experiment with attached mask (E3): A black mask with observation holes was attached on the transmissive side of the tank in order to reduce the flare effect. The same density dependent flow experiment as in E1 was conducted.

Assessment of light dispersion effect (E4): The last experiment examined the light scattering in the 3-phase system. Three slits of 7-13 cm length (1-1.5 cm wide) in masks attached on the reflection side of the tank reduced the light source and the transmission images were recorded. The recorded transmission images should ideally deliver a sharply delineated slit. However, light is subject to reflection and refraction within the 3-phase system, resulting in light dispersion.

II.2.1.4 Results and discussion

II.2.1.4.1 Homogeneity of illumination and determination of measurement area

Figure II.18 shows a reflection image and a transmission image. The fine glass bead is highly reflective and therefore appears brighter than the coarse beads on the reflection image. For the transmission it is vice versa and the coarse bead zone transmits more light. The horizontal intensity profiles in Figure II.21 (AA' in Figure II.18) indicate a brighter region in the center of the tank for both reflection and transmission measurements. The brightness variations along the reflection profile are less pronounced than along the transmission profile. Although the glass beads act as prism, spatial homogeneous illumination cannot be achieved by transmission measurements. However, this is not a disadvantage because the parameters of Equation II.5 are determined for each observation point specifically. Since the heterogeneous illumination patterns are equal for each image and independent of the dye intensity of the experiments, the observation point based calibration accounts for illumination heterogeneity. Vignetting could also cause a reduction of an image's brightness or saturation at the periphery compared to the image center [Ray, 2002]. The calibration procedure accounts for that and avoids errors caused by vignetting.

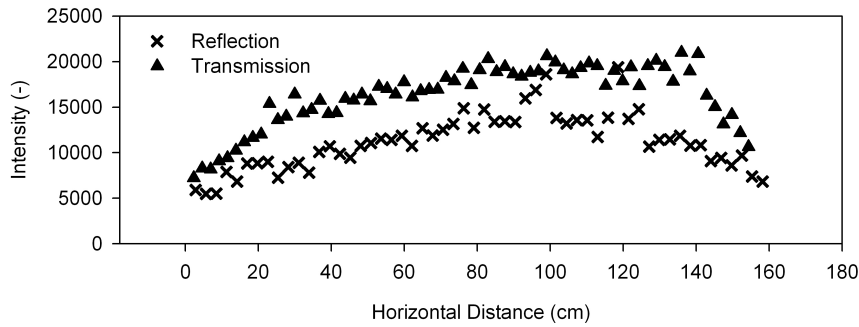


Figure II.21: Horizontal intensity profile AA' (Figure II.18) for transmission and reflection intensities.

The glass beads cause noise and the precision of point measurements increases with increasing number of pixels summarized to the observation point [Konz *et al.*, 2008a]. The transmission images had a resolution of 0.46 mm per pixel, the reflection images had 0.56 mm per pixel. Two different cameras were used (Nikon D70 and D80), which explains the differences in resolution. Standard deviations (%) of intensities of eleven 100×100 pixel squares consisting of 10000 pixels each, placed in the fine beads zone and in the coarse beads zone, were calculated in order to show the optical heterogeneity for transmission and reflection images (Figure II.22). The reflection measurements deliver higher deviations for the coarse beads of about 12% and about 4% for the fine beads. The transmission intensities show no differences between the bead sizes. In order to determine the appropriate measurement resolution, we analyzed the intensity distributions in the 100×100 pixel squares. The intensities were determined by medians of stepwise increased pixels from 1×1 to 20×20 pixels. The standard deviation was taken as a measure for the quality of the calculated intensity value. The appropriate measurement resolution was found to be 10×10 pixels for transmission images and 10×10 pixels and 15×15 pixels for the fine, respectively coarse, beads of the reflection images. The reflection images are therefore more sensitive to the grain size than the transmission images.

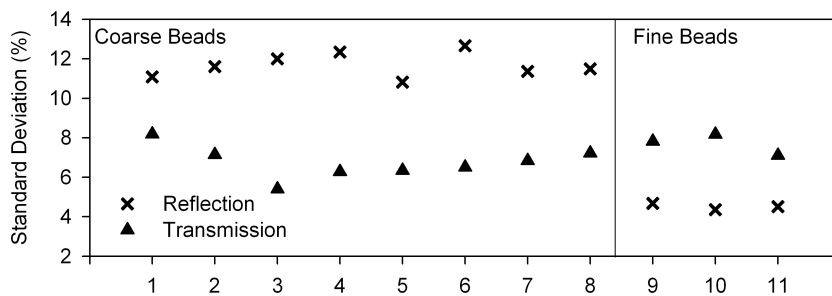


Figure II.22: Standard deviations of eleven 100×100 pixel squares.

II.2.1.4.2 Lens flare effect and scattered light

Figure II.23 compares the concentrations of three points spread along the tank during experiment E1, determined by transmission (blue) and reflection (red) measurements.

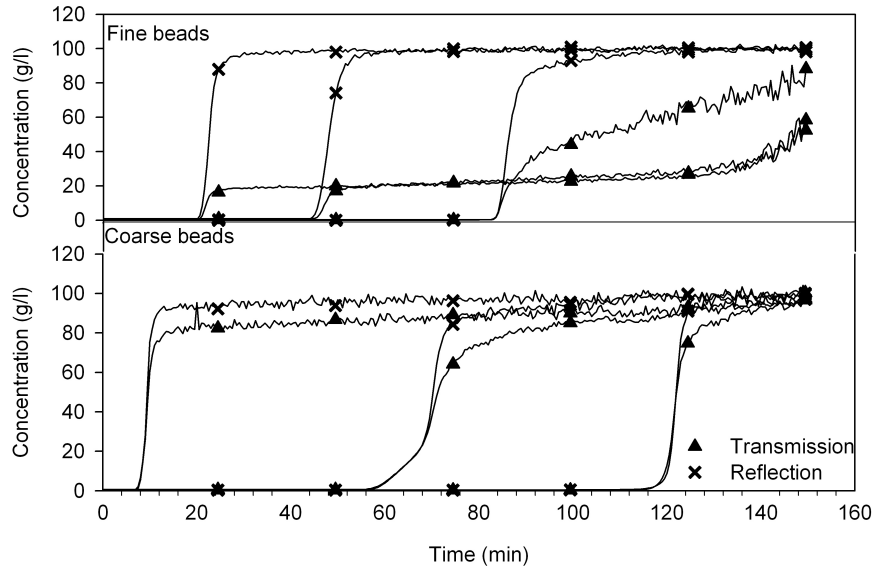


Figure II.23: Concentrations of E1 determined by reflection and transmission measurements.

The reflection images deliver the expected S-type curve, which reach the maximum concentration of 100g/l. However, the transmissive concentration curves show significant deviations from the S-type curve. The onset of concentration rise compares well between transmissive and reflective measurements, but the transmission data exhibit plateaus over several minutes and a second concentration ascent can be observed at the end of the experiment. The effect is more pronounced for the fine beads than for the coarse beads. The curves of the coarse beads show a continuous ascent of concentration. Since the experimental conditions are stable (saltwater below freshwater) fingering is not relevant. Two sources of errors can explain this behavior of the transmission curves: (i) lens flare effects, and (ii) light dispersion due to scattering within the porous media.

Lens flare effect: Cameras contain lenses, which are comprised of several lens elements. Lens flare is caused by light, which reflects internally on lens elements any number of times (back and forth) before finally reaching the digital sensor. Thus, flare is technically caused by internal reflections. In order to become significant, it requires an intense light source. In flow tank experiments, the most intense image light source is the reflection or the transmission of regions not affected by the dyed solute. The dye absorbs light and therefore reduces the intensity. Due to the flare effects regions of the tank with high dye concentrations, resulting in low reflected or transmitted intensity, might appear brighter. During the course of E1, the reflection intensity reaches the level of the expected intensity for the maximum dye concentration of the solute found in the calibration experiments (Figure II.24).

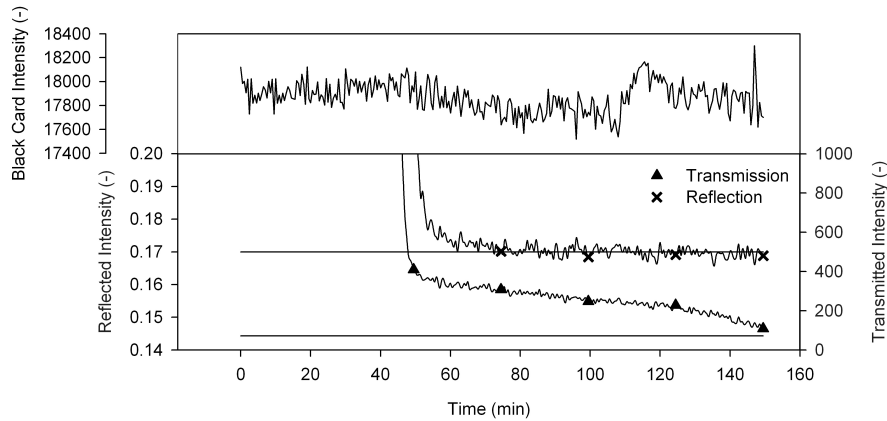


Figure II.24: Intensity values of reflection and transmission measurements with 100g/l calibration intensity.

Perturbations caused by flare are minor in this experimental setup for reflection measurements. *Konz et al.* [2008a] reported a relatively small error of up to 3% caused by flare effects for reflection images. In their experimental setup a homogeneous porous media with the fine glass beads (diameter: 0.6 mm) was used. As shown in Figure II.18 the fine glass beads reflect more light than the coarse beads and therefore might generate relevant flare effects if the entire tank is filled with these beads. The transmission data in Figure II.24, however, show a continuous decline of intensity in line with the decrease of bright regions of the tank. The coarse beads appear significantly brighter than the fine beads causing the flare effects. The reflected black card intensity (see Figure II.28) in Figure II.24 is on a constant level, which proves the existence of a constant light source. Therefore, changing illumination does not cause the decline of transmitted intensity. The impact of flare can also be observed by comparing the intensity of sequentially attached black cards on the transmission side of the tank [*Konz et al.*, 2008a]. The profiles in Figure II.25 were taken from a 10 cm high black card placed at the bottom of the tank in E2 (Figure II.20). Additional black cards were attached in a sequential order and images were taken of each step. In the last step of E2, the cards covered the entire tank above the first card and therefore significantly reduced the transmitted light.

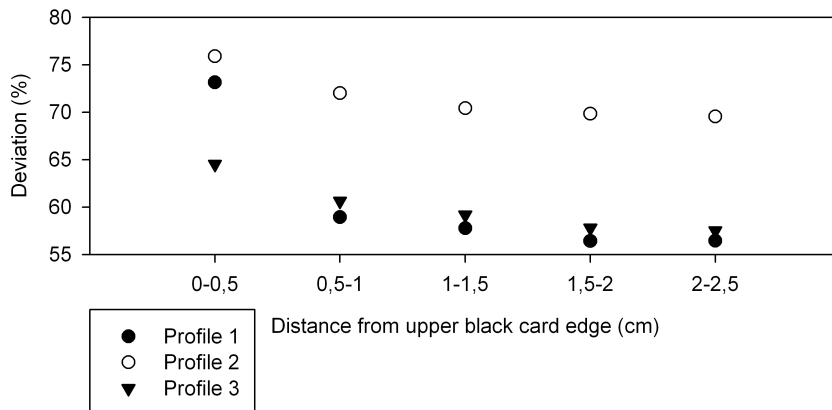


Figure II.25: Intensity deviation (%) between the first and the third step of E2 along vertical profiles of black Card 1 shown in Figure II.20.

Figure II.25 shows the differences of intensities taken along profiles of the first card between the first and the last step. Up to 78% of intensity decline could be observed. A comparable experiment with reflection intensities delivered an error of less than 1%. *Konz et al.* [2008a] showed that a black mask with observation holes can reduce the flare effect. In E3 a mask was placed on the transmission side of the tank with observation holes at different positions on the tank. The same density-dependent experiment as in E1 was conducted and intensity values were recorded at the observation holes. Figure II.26 exemplifies the intensity developments for observation points in the fine beads zone and in the coarse beads zone. In contrast to E1 without the mask, the transmissive intensities reached a constant level during the course of E3 and no flare effects were observed (Figure II.26). The mask significantly reduced the light of the transmission image and thus eliminated the prerequisite for flare effects. The experiments E2 and E3 showed the relevance of this effect for transmission measurements.

Light scattering: Scattering within the bead-water-Plexiglas system causes light dispersion of the transmission image smearing the plume front [*Huang et al.*, 2002; and *Rezanezhad et al.*, 2006]. The dispersion of light intensity is shown for one slit of E4 in Figure II.27. The 1.5 cm wide slit causes an area with an extent of up to 27 cm to be affected. The center of the affected area matches with the location of the actual edges of the silts.

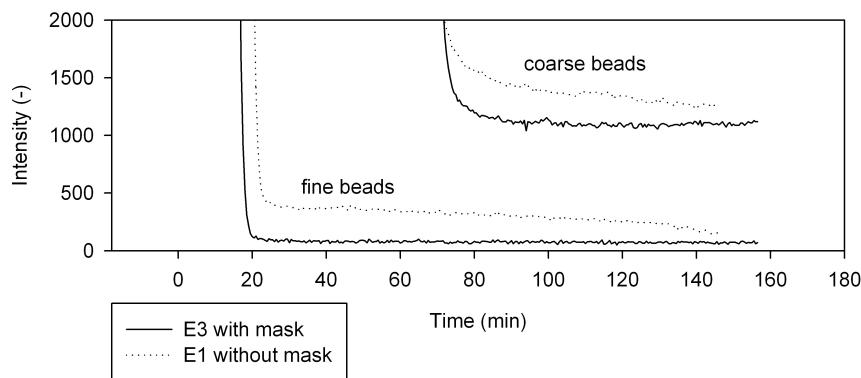


Figure II.26: Comparison of transmission intensities of E1 without the mask and E3 with the mask.

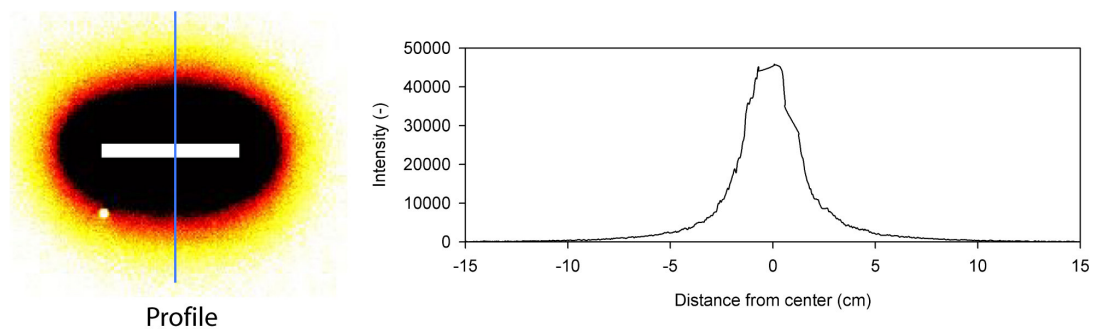


Figure II.27: Light dispersion caused by a rectangular slit (white). The intensities are taken along the vertical profile.

The coarse glass beads favor the Gaussian-like decay of intensity due to light dispersion, whereas the effect is less pronounced for the fine beads. Scattering reduces the contrast

between zones of different dye concentration and between porous media classes, and therefore smears the front of the plume. The profile BB' (Figure II.18) in Figure II.28 shows an intensity increase at the edges of the fine glass bead zone caused by scattered light from the coarse beads zone. This effect can be observed for 0g/l and 1g/l (100g/l salt concentration) of dye concentration. *Rezanezhad et al.* [2006] applied a point spread function to correct for distortion of the images. Their results proved the ability of the procedure to improve the images. However, the effect still has an impact on the quality of the transmission data. The effect also depends on the width of the tank and is therefore reduced in thin flow tanks.

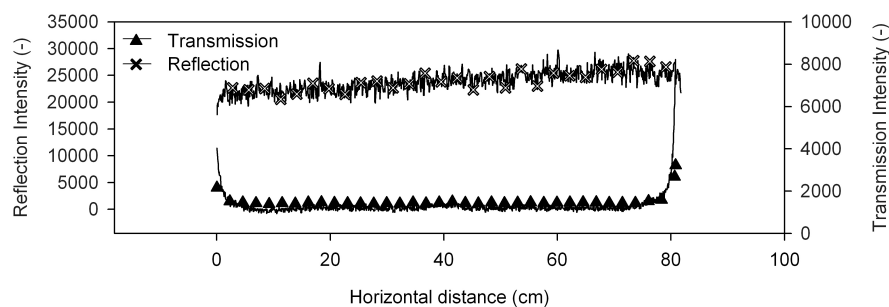


Figure II.28: Horizontal reflection and transmission intensity profiles, BB' (Figure II.18) along the fine glass beads.

II.2.1.5 Conclusions

We compared transmission and reflection intensity measurements to determine solute concentrations in heterogeneous intermediate scale laboratory experiments using an ordinary light source and a non-fluorescent dye tracer. This was done regarding illumination homogeneity of the photographed domain, lens flare effects and scattered light within the bead-water-Plexiglas system. The following phenomena could be observed:

- Fine glass beads appear brighter than coarse beads on the reflection image and vice versa on the transmission image.
- The reflection images deliver a more homogeneous spatial illumination than the transmission images.
- The noise from the glass beads is the most pronounced at the coarse beads of the reflection images.
- Lens flare effects significantly perturb the transmission measurements.
- Scattered light within the bead-water-Plexiglas system smears the plume front of the transmission images.

Due to these phenomena, the light reflection method outperformed the transmission method in our experimental setup. The perturbations are highly dependent on the experimental setup, e.g. width of the tank, camera and light source position. It is therefore recommended to assess the perturbations of the intensity measurements for each setup specifically. The mask with observation holes reduces the flare effect; however, it also reduces the data availability to a predefined number of observation points and does not allow for the determination of concentration contour lines. The utilization of fluorescent dye under ultra-violet illumination could reduce the lens flare effect since the light captured by the camera is emitted from the tracer itself.

II.2.1.6 References

- Catania F, Massabo M, Valle M, Bracco G, Paladino O (2008) Assessment of quantitative imaging of contaminant distributions in porous media. *Exp Fluids* 44: 167–177
- Corapcioglu M Y, Chowdhury S, Roosevelt S E (1997) Micromodel visualization and quantification of solute transport in porous media. *Water Resour. Res.* 33 (11): 2547–2558
- Detwiler R L , Rajaram H, Glass R J (2000) Solute transport in variable-aperture fractures: An investigation of the relative importance of Taylor dispersion and macrodispersion. *Water Resour. Res.* 36 (7): 1611– 1625
- Goswami R, Clement P (2007) Laboratory-scale investigation of saltwater intrusion dynamics. *Water Resour. Res.* 43: W04418
- Huang W, Smith C C, Lerner D N, Thornton S F, Oram A (2002) Physical modelling of solute transport in porous media: evaluation of an imaging technique using UV excited fluorescent dye. *Water Res* 3 (7): 1843–1853
- Jones E H, Smith C C (2005) Non-equilibrium partitioning tracer transport in porous media: 2-D physical modelling and imaging using a partitioning fluorescent dye. *Water Res* 39 (20): 5099–5111
- Konz M, Ackerer P, Meier E, Huggenberger P, Zechner E, Gechter D (2008a) On the measurement of solute concentrations in 2-D flow tank experiments. *Hydrol. Earth Syst. Sci.*, 12: 727-738
- Konz M, Ackerer P, Younes A, Huggenberger P, Zechner E (2008b) 2D Stable Layered Laboratory-scale Experiments for Testing Density-coupled Flow Models. *Water Resour. Res.*, 45, doi:10.1029/2008WR007118, 2009
- McNeil J D, Oldenborger G A, Schincariol R A (2006) Quantitative imaging of contaminant distributions in heterogeneous porous media laboratory experiments. *J. Contam. Hydrol.* 84: 36-54
- Oostrom M, Dane J H, Guven O, Hayworth J S (1992) Experimental investigation of dense solute plumes in an unconfined aquifer model. *Water Resour. Res.* 28: 2315– 2326
- Rahman A, Jose S, Nowak W, Cirpka O (2005) Experiments on vertical transverse mixing in a large-scale heterogeneous model aquifer. *J. Contam. Hydrol.* 80: 130– 148
- Ray S F (2002) *Applied photographic optics*, 3rd ed., Focal Press.
- Rezanezhad F, Vogel H J, Roth K (2006) Experimental study of fingering flow through initially dry sand. *Hydrol. Earth Syst. Sci. Discuss.*, 3: 2595-2620

Rogers G (1976) Photography in paediatrics. Published in photographic techniques in scientific research, Volume 2, edited by Newman, A.. Academic Press, ISBN 0 12 517960

Schincariol R A, Herderick E E, Schwartz F W (1993) On the application of image analysis to determine concentration distributions in laboratory experiments. *J. Contam. Hydrol.* 12: 197–215

Simmons C T, Pierini M L, Hutson J L (2002) Laboratory investigation of variable-density flow and solute transport in unsaturated–saturated porous media. *Transp. Porous Media* 47: 15– 244

Swartz C H, Schwartz F W (1998) An experimental study of mixing and instability development in variable-density systems. *J. Contam. Hydrol.* 34: 169– 189

Theodoropoulou M A, Karoutsos V, Kaspiris C, Tsakiroglou C D (2003) A new visualization technique for the study of solute dispersion in model porous media. *J Hydrol* 27 (1–4): 176–197

Wildenschild D, Jensen K H (1999) Laboratory investigations of effective flow behavior in unsaturated heterogeneous sands. *Water Resour. Res.* 35: 17–27

III. Benchmarking numerical density-flow models

Paper published in *Water Resources Research*

2D Stable Layered Laboratory-scale Experiments for Testing Density-coupled Flow Models

Konz, M.⁽¹⁾; Ackerer, P.⁽²⁾; Younes, A.⁽²⁾; Huggenberger, P.⁽¹⁾; Zechner, E.⁽¹⁾

⁽¹⁾Department of Environmental Sciences, University of Basel, Institute of Geology, Applied and Environmental Geology, Basel, Switzerland

⁽²⁾ Université Louis Pasteur, Institut de Mécanique des Fluides et des Solides, CNRS, UMR 7507, Strasbourg, France

III.1 2D Stable Layered Laboratory-scale Experiments for Testing Density-coupled Flow Models

III.1.1 Abstract

A series of laboratory-scale 2D porous medium tank experiments was conducted to study stable layered variable density flow problems using well-defined experimental parameters and boundary conditions. The experiments were carried out both in a rectangular flow tank and in a more complex geometrical setup aimed at studying variable density flow in geometries similar to geological formations of aquifers and aquicludes connected via fault zones. An impermeable layer within the porous medium tank forced the solutes to pass through a vertical channel, representing a geological fault zone, to reach the outlet of the tank. Flow through the porous medium occurred through a single inflow opening and through an outflow opening on the opposite edge of the domain. An image analysis technique delivered 2, 10, 50 and 80% salt concentration isolines at distinct times. Breakthrough curves of the dyed saltwater with an initial density of 1063g/l were available at any location within the tank. The experimental data are presented as benchmark problems to evaluate numerical codes. A numerical model based on Mixed Finite Elements for the fluid flow problem and a combination of Discontinuous Galerkin Finite Element and Multi-Point Flux Approximation methods for the transport turned out to be adequate for the simulation of the physical experiments. The high data availability makes the proposed benchmark experiments a valuable tool for assessing the performance of density-coupled flow models.

III.1.2 Introduction

The need for accurate simulations of variable-density solute transport in aquifers continues to increase due to the large number of environmental problems associated with variable-density flow phenomena. The range of problems comprises saltwater intrusion in coastal aquifers [Huyakorn *et al.*, 1987], the leakage from landfills, and radioactive or toxic waste disposal in salt rock formations [Ludwig *et al.*, 2001]. The field example underlying this study is the subsidence hazard in urban areas caused by salt dissolution. The Upper Rhine valley, in the sector extending across the Tabular Jura of north-western Switzerland, is characterized by urban activities such as a complex system of natural and artificial groundwater recharge and groundwater uptake (up to 1.5 m³/s) for industrial processes and drinking water supply. The artificial flow field is one possible reason for dissolution of subsurface salt formations causing surface deformation and potential formation of new pathways for groundwater movements along fault systems. The tectonic style of the region is characterized by a series of horsts and grabens, which favour vertical exchange of water across aquitards [Figure III.1, Spottke *et al.*, 2005]. The regional aquifer in the bedrock is the Upper Muschelkalk aquifer (Hauptmuschelkalk and Trigonodusdolomite). Hydraulic barriers overlie and underlie the Hauptmuschelkalk aquifer. The Middle Muschelkalk is dominated by evaporitic facies, consisting of an up to 50 m thick salt formation. Density effects, the complex structural setting of horst and graben structures, the natural hydraulic conditions and the hydraulic forcing by intense pumping activities all have an influence on the transport and mixing of salt in complex

geological settings. The complexity of the interplay of the different effects makes it necessary to develop reliable and robust numerical models, which first need to be tested in laboratory experiments under controlled conditions. This strategy promotes a better understanding of the influence of the different effects, and is a prerequisite for a more systematic setup for groundwater monitoring and sampling systems at the regional scale. However, the modeling of density-driven flow in porous media remains challenging, due to the non-linear coupling between flow and transport [Diersch and Kolditz, 2002; Johannsen *et al.*, 2002]. Commonly, three benchmark tests for density-coupled flow models are used: The Henry problem of seawater intrusion [Henry, 1964]; the Hydrocoin problem of a simplified salt dome [OECD, 1988] and the unstable Elder problem [Elder, 1967]. These test cases are either not sensitive [Henry problem, Simpson and Clement, 2004], or the solution is not precisely known (Elder and Hydrocoin).

Hence, in order to evaluate the accuracy of the numerical codes, laboratory-scale experiments are valuable tools which provide detailed data sets of several types: breakthrough curves (BTCs) at different locations and/or concentration distribution maps at different times, under well-defined conditions (boundary and initial conditions are known, the porous medium properties can be determined separately) avoiding model calibration.

One-dimensional experiments [e.g. Hassanizadeh and Leijnse, 1995; Schotting *et al.*, 1999; Watson *et al.*, 2002; Jiao and Hötzl, 2004], which are not well suited for the evaluation of numerical models, have been used to improve our understanding of the underlying processes, especially the validity of Darcy's and Fick's laws. Two- and three-dimensional experiments have been performed to define stability criteria and to provide data sets for testing numerical models. These experiments were performed on setups of:

- decimeter scales like Hele Shaw type cells [Wooding *et al.*, 1997; Oltean *et al.*, 2008], 2-dimensional [Goswami and Clement, 2007] or 3-dimensional [Pearl *et al.*, 1993; Oswald and Kinzelbach, 2004; Oswald *et al.*, 2007] tanks.
- meter scales of 2 dimensions [e.g. Schincariol and Schwartz, 1990; Oostrom *et al.*, 1992; Swartz and Schwartz, 1998; Zhang *et al.*, 2001] or 3 dimensions [Gheith and Schwartz, 1998].

Since the shape of the interface between freshwater and saltwater is scale dependent, either 2D setups in a meter scale or 3D experiments are preferable for benchmarking.

New experiments on 2D setups at meter scale ($158 \times 60 \times 4$ and $158 \times 100 \times 4$ cm³) are presented here for the following reasons:

- The vertical dimension is important for studying density effects. 3D setups in meter dimensions are very difficult to handle and do not allow for a very detailed observation of the transport processes, while a vertical dimension at meter scale with detailed observations of the concentration distribution can be handled by 2D setups.
- Non-intrusive measurement techniques are preferable for avoiding flow perturbation. Concentrations are usually obtained by image analysis [Schincariol and Schwartz, 1990; Swartz and Schwartz, 1998; Zhang *et al.*, 2001], gamma radiation technique [Oostrom *et al.*, 1992], or nuclear magnetic resonance imaging technique [Oswald and Kinzelbach, 2004]. Optical visualization techniques require a colored dye added to NaCl for the injected solution. Previous methods [Schincariol and Schwartz, 1990; Swartz and Schwartz, 1998; Zhang *et al.*, 2001] were based on digitized images from black and white photographs which does not allow for a good description of the mixing zone [Zhang *et al.*,

2001]. Here a photometric technique is applied based on a digital camera with high resolution which enables the determination of a significantly wider range of concentrations and estimated small measurement errors [Konz *et al.*, 2008a]. BTCs at any point in the tank and isolines even for low concentrations (for example the 2% isoline) can therefore be provided.

- Laboratory experiments have usually been conducted on rectangular setups. We used a more complex geometry to enhance the effects of the density. This geometry was designed to facilitate the examination of the performance of numerical codes under more complex geometries which can be found in the subsidence hazard zone shown in Figure III.1.

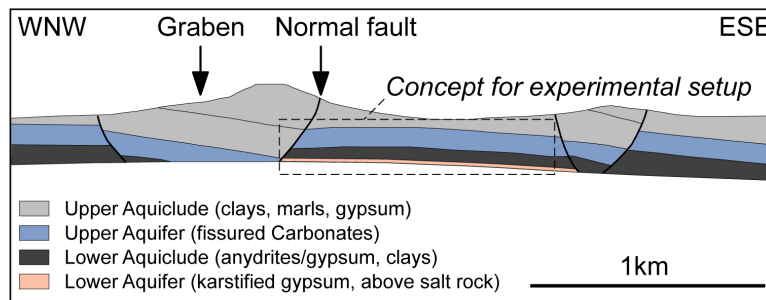


Figure III.1: Geological setting of Tabular Jura east of Basel, Switzerland.

Numerical simulations of the presented experiments were performed with a robust numerical model based on Mixed Finite Elements (MFE) for the fluid flow problem and a combination of Discontinuous Galerkin (DG) and Multi-Point Flux Approximation (MFPA) methods for the transport. A variant of this code with the standard Finite Volume (FV) method instead of the DG method was also used to simulate the experiments. The experimental data are presented along with the numerical simulations as benchmark experiments for testing numerical codes.

III.1.3 Materials and methods

III.1.3.1 Experimental procedure

Experiments on density flow with two geometric setups were conducted in a Plexiglas flow tank (Figure III.2). The first series, referred to as EXP_H, was performed with a rectangular geometry and a homogenous porous medium. A more complex geometry (referred to as more complex) was constructed for the second series of experiments, EXP_C in the following, with an impermeable layer made of Plexiglas that divides the flow domain into two regions connected by a 5 cm wide channel. For each geometrical setup, experiments with and without density effect were performed under comparable flow boundary conditions (Table III.1).

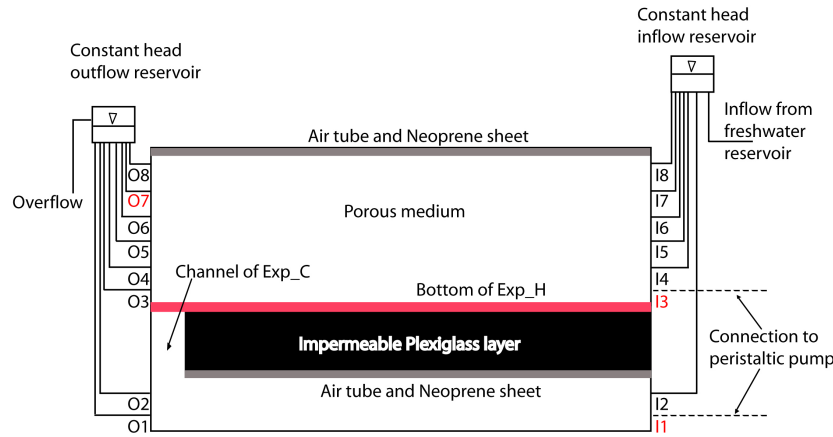


Figure III.2: Geometry of the flow tank. The bottom of the tank for the rectangular experiments, EXP_H/d was removed for the complex experiments, EXP_C/d. The openings used for the experiments are highlighted.

Table III.1: Summary of conducted experiments.

Experiment	Density (g/l)	Volumetric flow rate (l/min)	2D flow rate* (cm ² /min)	Duration
Exp_H	998	0.20 +/- 1.3%	50.41	99 min
Exp_Hd	1063	0.19 +/- 1.4%	48.33	88 min
Exp_C	998	0.19 +/- 1.5%	47.07	82 min
Exp_Cd	1063	0.20 +/- 1.6%	49.35	75 min

* flow rate used for simulation

In the following, the density-coupled experiments are referred to as EXP_Cd and EXP_Hd. In order to keep the boundary conditions simple, but also to imitate flow fields under the influence of extraction wells, flow was forced through one single inflow opening and one outflow opening on opposite sides of the tank. Solely, the outflow opening O7 (Figure III.2) was used for both experimental setups and connected to a constant head reservoir. In the case of EXP_H and EXP_Hd, a peristaltic pump was connected to I3, whereas I1 was used for EXP_C and EXP_Cd. The application of the pump was necessary to maintain a constant flux because the density of the freshwater in the outflow reservoir increased throughout the experiment when the saltwater reached the outlet and denser saltwater replaced the freshwater. This caused a decline of the flow rate if a constant head reservoir was applied to the inflow opening instead of the pump. In EXP_C and EXP_Cd the marked freshwater and the saltwater had to pass through the channel from beneath the impermeable layer towards the outlet. Volumetric and gravimetric flux measurements were conducted several times during the experiments by sampling discharged water at the outlet of the reservoir during two min. The volumetric flow rate was almost constant for all experiments with a maximum 1.6% of standard deviation (Table III.1). The pollutants entering the domain were marked with a dye to determine concentrations from optically measured dye intensities. The tank was flushed with freshwater before and after the experiments, applying a constant head difference between inflow and outflow reservoirs (see Figure III.2).

III.1.3.2 The model aquifer

All experiments were conducted in the same flow tank (Figure III.2). The back plate of the tank could be removed to enable modifications of the tank geometry. An intermediate bottom was installed, marked with the red bar in Figure III.2 for the rectangular geometry experiments, EXP_H/d. The constructional details are summarized in Figure III.6 and only the relevant inflow and outflow openings are shown. The inlets could either be connected to a constant head reservoir or to a peristaltic pump. Since the Plexiglas walls of the tank deformed when the tank was filled with a water-saturated porous medium, tension pins with a diameter of 0.5 cm were installed within the tank to prevent deformation. These obstacles were minor and we assumed that they did not perturb the laminar flow of the experiment. The back plate of the tank held devices to place the measurement instruments, whereas the front side of the tank consisted of a clear Plexiglas pane facilitating visual observation of the tracer movement through the porous medium during the course of the experiments. The measurement instruments consisted of temperature sensors (YSI 4006; accuracy $\pm 0.01^\circ\text{C}$) and pressure sensors (Keller, PR 35H/80797; accuracy ± 0.2 cm). The four pressure sensors were placed in a horizontal line 57 cm above the bottom of the EXP_H/d setup, and 96 cm above the bottom of the EXP_C/d setup. Glass beads (main constituent SiO_2 , SiLi-Beads GmbH, Germany) with an average diameter of 0.65 mm were used as porous medium. The tank was packed under fully saturated conditions and the beads were tamped down to achieve homogeneous conditions. Neoprene sheets and air tubes were placed between the Plexiglas cover/impermeable Plexiglas layer and the porous medium. The air tubes could be inflated to compensate for free space if the glass beads compacted. This prevented preferential flow along the top cover of the tank and underneath the Plexiglas layer. Supplementary experiments with traced water flowing horizontally through the tank revealed that there were no preferential pathways and that the water flowed uniformly through the porous medium only. The Neoprene sheets and air tubes had a total height of 2.5 cm beneath the top cover and 3.0 cm beneath the Plexiglas layer, which reduced the flow zone. For all experiments, deionized water with a constant temperature of 20°C to reduce degassing was used.

III.1.3.3 Photometric method to derive concentrations within the flow tank

In general, color dyes are successfully used to mark saltwater in flow tank experiments (e.g. *Schincariol et al.*, 1990, *Swartz and Schwartz*, 1998, *McNeil et al.*, 2006, *Goswami and Clement*, 2007). For our experiments, the injected fluid was marked with the dye Cochineal Red A (E124) to visually differentiate them from the ambient pore water. Details of the image analysis technique can be found in *Konz et al.* [2008a,b]. This food dye is nonsorbing, relatively inert, and mostly nonreactive with NaCl in concentrations used for the experiments [*Rahman et al.*, 2005, and our own batch experiments]. However, dye precipitation could be observed for NaCl concentration higher than 200 g/l. Therefore, the maximal concentration in the experiments was limited to 100 g/l. Chromatographic effects due to different diffusion coefficients of E124 and NaCl could not be excluded but are of minor importance due to the experiments' durations. In preliminary column experiments under similar conditions (porous material, velocity, travel distance), no significant differences were found between BTCs of NaCl obtained by resistivity measurements and of the color dye determined by intensity measurements.

To determine BTCs of concentrations at various points within the tank, we took photos with the digital camera Nikon D70 using a reproducible illumination with a single light source placed right above the camera at a distance of ~3 m from the tank. The light source (Kobold-Licht, DFR200, 200W, 5600K) was adjusted and checked with a luxmeter to minimize spatial lighting nonuniformity. A dark curtain placed around the entire experimental setup prevented reflections of any objects on the tank pane.

The image-processing procedure included the following steps: (i) data conversion to 16 bit tif images (65536 intensity values per channel of the RGB color space) with the freeware dcraw (<http://cybercom.net/~dcoffin/dcraw/>), (ii) selection of green channel (most sensitive to dye concentrations), (iii) determination of measurement area, (iv) correction of fluctuations in brightness using attached white cards (I_{corr}), (v) construction of a curve that relates intensities to concentrations from calibration images, and determination of function parameters for the mathematical formulation of the curve expressed by:

$$C_{i,j}(t) = A_{i,j}^1 \exp(I_{i,j}^{corr}(t)/b_{i,j}^1) + A_{i,j}^2 \exp(I_{i,j}^{corr}(t)/b_{i,j}^2) + D_{i,j} \quad (\text{III.1})$$

where $C_{i,j}(t)$ is the concentration at time t , $A_{i,j}^1, A_{i,j}^2, D_{i,j}, b_{i,j}^1, b_{i,j}^2$ are parameters, $I_{i,j}^{corr}$ is the brightness-corrected intensity at time t and i, j are the pixel coordinates.

The saturated porous medium in the flow tank was filled with solutions of predetermined saltwater dye concentrations (0.5, 3, 5, 8, 10, 15, 20, 40, 70, 100 g/l of saltwater; the dye concentration was always 1/100 of the salt concentration) in a sequential order from low-density solutions to high-density solutions for calibration (step v). Finally, (step vi) measured intensities of the flow experiments had to be converted into concentrations applying Equation III.1. As outlined in *Konz et al.* [2008a], the main perturbation of the measurement was the impact of lens flare. In porous media experiments, the artificial glass beads cause high reflection intensity, which may generate flare effects in the camera lenses that have enough intensity to perturb the measurements. Regions of the photographed domain, which have a high dye concentration, can appear brighter because of the lens flare effects. That causes an underestimation of concentrations. A series of experiments were conducted to estimate the error caused by the lens flare. Details on this effect can be found in *Konz et al.* [2008a]. The maximum error was determined to be +3% of the intensity values for the maximum concentration of 100g/l. The mass balances could be calculated to test the performance of the image analysis approach based on the given mass of salt entering the domain and the mass within the domain determined by image analysis at different time steps. The image analysis took the porosity and the depth of the tank into account. The impact of lens flare became more pronounced if only a small portion of the domain was filled with the dark solution. If the tank was entirely filled with the dark solution the effect was reduced.

In our investigation, we analyzed the mass balance for EXP_Hd after 10 and 45 minutes. The 10 min image delivered an underestimation of the total mass of -4.2% compared to the mass entering the domain. This was within the range of expected lens flare errors. After 45 min, the bright region of the tank was significantly reduced and the mass error accounted for 1.6%, indicating that the method slightly overestimated the total mass. As a result of this analysis, the calibration parameters of Equation III.1 could be considered to be reliable, and possible errors could be explained by the impact of lens flare. The flare effects are more pronounced for transmission measurements [*Konz et al.*, 2008b].

Therefore, reflection data were used in this study. Since the error was small and mainly affected the concentrations higher than 80g/l, we present the measurements without error bars. Images were taken every 30 sec during the course of the experiments. This enabled the determination of BTCs at every point in the flow tank and the computation of concentration isolines at distinct time steps.

III.1.3.4 Determination of experimental parameters

Permeability is a crucial parameter for density-dependent flow experiments even in the case of fixed-flux boundary conditions. Since the permeability of the aquifer model depends on the packing density of the porous medium, the most appropriate way to estimate the average permeability of the porous medium is an in situ method [Oostrom *et al.*, 1992; Goswani and Clement, 2007]. The flow through the model aquifers of both geometrical setups and the pressure differences between four pressure sensors were measured for various hydraulic gradients forced by fixed heads of the in- and outflow reservoirs (Figure III.2). The head difference was significantly higher than the sensitivity of the sensors. This was not the case for the benchmark experiments. Further, a peristaltic pump was applied to maintain a constant flow rate in EXP_H/d and EXP_C/d. Due to the pulsing of the pump the pressure sensors delivered fluctuating values. The pump was necessary in our experimental setup especially for the saltwater experiments. The impact of the pulsing on the volumetric flux was not visible as proven by flow measurements. Inverse 2D modelling was used to determine the permeability. The in situ method gave an average value for the permeability of $3.4 \times 10^{-10} (\pm 0.1 \times 10^{-10}) \text{ m}^2$ for both experimental setups. Using the Kozeny-Carman equation delivered a permeability of $3.2 \times 10^{-10} \text{ m}^2$ for a grain diameter of 0.65 mm, whereas the equation of Bear [1972] gave 2.6×10^{-10} . Additional column experiments were conducted applying different filling methods, with and without tamping down the porous medium. Depending on the packing in the columns, the permeability varied between 3.5×10^{-10} and $4.6 \times 10^{-10} \text{ m}^2$. The permeability increased with decreasing tamping and the latter value was observed for packing without tamping. In the 2D tanks, the porous material was placed with intensive tamping assumed to be more or less homogeneous. Preferential flow paths or inhomogeneities could not be detected by detailed analyses of tracer concentrations distributions at different times after injection. Therefore, the porous medium was assumed to be homogeneous with an average permeability of $3.4 \times 10^{-10} (\pm 0.1 \times 10^{-10}) \text{ m}^2$ considered here as an equivalent parameter.

In order to estimate the longitudinal dispersivity, α_l , and the porosity, tracer tests were conducted within the flow tank by continuous injection of a solution with predetermined E124 dye concentration of 0.5 g/l. With that dye concentration, no density effects were expected. Flow was applied between the openings I5-O5 for Exp_H and between I1-O1 and I5-O5 for Exp_C (Figure III.2). The tracer front in all cases was very sharp and a transport model simulation with 0.6 mm as longitudinal dispersivity was able to predict the breakthrough curves of the tracer plume at various points across the tank. This is well in line with findings of Perkins and Johnston [1963] who analyzed a number of laboratory-scale dispersivity values. Oswald and Kinzelbach [2004] and Goswani and Clement [2007] previously reported relatively small dispersivity values within the range of the grain diameter for uniform artificial porous medium systems. Commonly the transverse dispersivity is set to be a small fraction of the longitudinal dispersivity in the range of 1/20 and 1/6 according to Harleman and Rumer [1963] and Huang *et al.* [2003].

Therefore, the transverse dispersivity was assumed to be 1/10 of the longitudinal dispersivity following *Johannsen et al.*, [2002] and *Oswald and Kinzelbach* [2004].

Porosity is a sensitive parameter in transport simulations with fixed-flux boundary conditions and the simulation of the tracer experiments gave an average value of 0.37. Further, volumetric and gravimetric measurements were conducted, and the average value of porosity was estimated to be 0.38. Therefore, the porosity could be determined as the average of these values to be 0.375, and it was valid for effective porosity as assumed by *Oswald and Kinzelbach* [2004].

The saltwater solution used in the experiments was the same solution as used for the 100 g/l calibration step. This prevented minor alterations in density or color intensity between calibration and experiment due to preparation differences. The densities of the saltwater solutions were determined with a hydrometer and volumetrically equal to $1063 \pm 1 \text{ g/l}$ for EXP_Hd and EXP_Cd.

III.1.4 Experimental results

The value of a benchmark problem for testing density-coupled flow models can be assessed by comparing coupled versus uncoupled flow experiments under equal boundary conditions [*Simpson and Clement*, 2003]. Figure III.3 shows the experimental plume patterns of the four coupled and uncoupled experiments at different points in time.

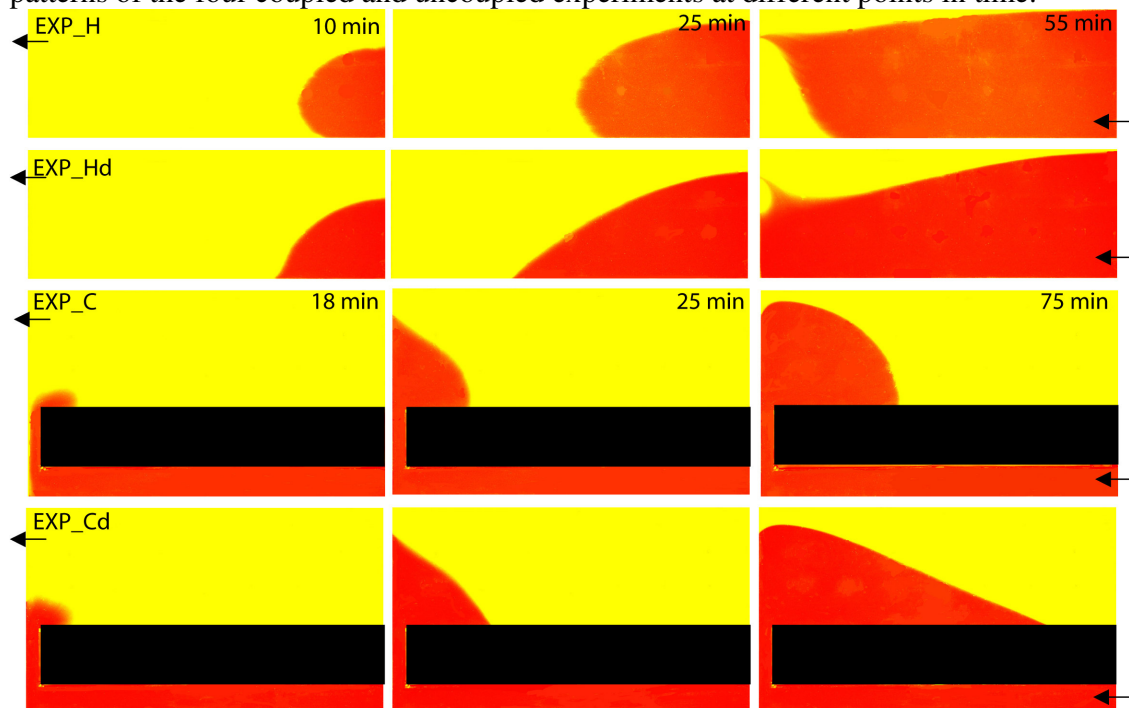


Figure III.3: Comparison of coupled and de-coupled experiments. The inflowing solutes are in dark grey, the freshwater is grey.

The inflowing solutes were marked red, the freshwater yellow in Figure III.3. Both the rectangular and the complex geometric experiments showed explicit differences in the plume patterns between the coupled and uncoupled experiments. Due to the high density contrast, the saltwater entering the tank with the rectangular setup (EXP_Hd) spread faster along the bottom of the tank and reached the opposite boundary first at the lower

left corner after 46 min. Eight minutes later the plume reached the outlet of the tank, O7. Gravity forces caused the plume to assume an almost rectangular shape until it reached the left boundary of the tank, and the concentration gradients were steep. While approaching the outlet, a wavelike shape developed in the region around the outlet after 55 min. Dispersive and diffusive mixing took place between the saltwater and the freshwater. The isolines in Figure III.4 show that the transition zone significantly expanded towards the outlet O7, generally called upconing process, whereas the sharp front prevailed at the right boundary of the tank.

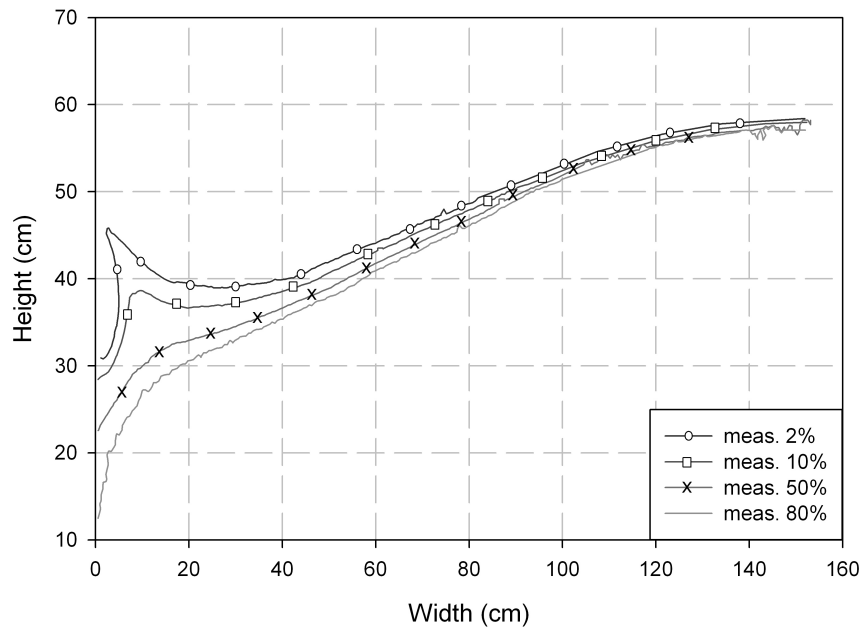


Figure III.4: Isolines of EXP_Hd after 55 min.

The experiment was stopped after 90 min when a quasi-steady-state evolved and the plume did not move significantly further. The dyed freshwater plume in the tracer experiment, EXP_H, had a more circular shape at the beginning of the experiment and it arrived at the left side of the tank first, at O7 after 53 min. In this experiment, the forced convection caused by the pumping was the dominant process. Since the boundary conditions of EXP_H and EXP_Hd could be viewed as equal in terms of flow velocity (see Table III.1), the different plume patterns could be said to have resulted from different density contrasts.

The saltwater spread further along the top of the impermeable layer in EXP_Cd, assuming an almost triangular shape, whereas the dyed freshwater in EXP_C acquired a circular shape (Figure III.3). The isolines in Figure III.5 indicated a sharp interface of the saltwater plume above the impermeable layer after 75 min in EXP_Cd.

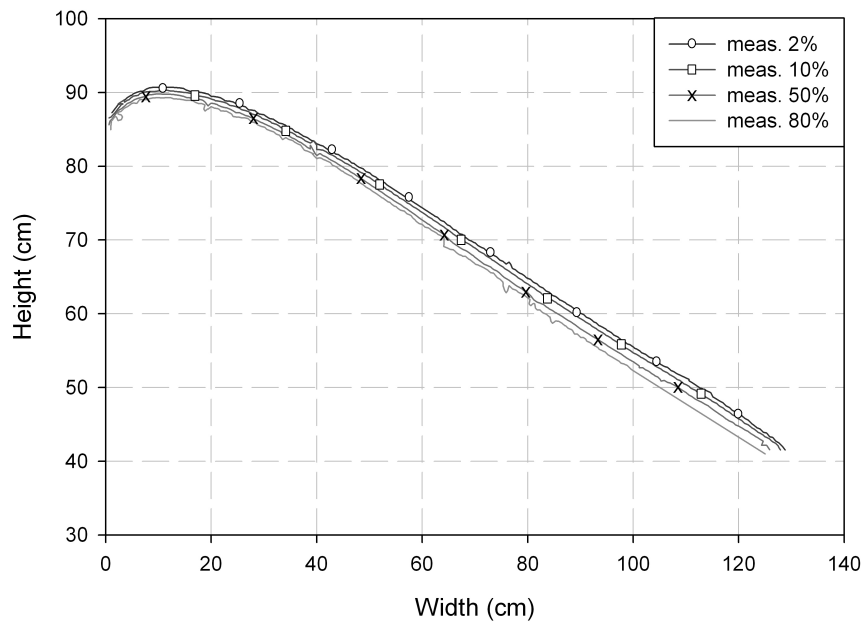


Figure III.5: Isolines of EXP_Cd after 75 min.

The transition zone was slightly wider at the right side above the impermeable layer, compared to the region around O7. The quasi steady state was reached after 80 min and EXP_Cd was stopped.

The direct comparison of coupled and uncoupled experiments conclusively showed the sensitivity of the experiments to density contrasts. Thus, both EXP_Hd and EXP_Cd could be used to test density-flow codes.

III.1.5 Modeling methods

Modeling the physical experiments requires a coupled flow-transport numerical model. To this end, Darcy's flow equation and the advection dispersion transport equation are coupled with the state equations, linking density and viscosity to mass fraction. Darcy's law is assumed to be valid as stated by *Watson et al.* [2002]. The validity of Fick's law is still under debate [*Hassanizadeh and Leijnse*, 1988; *Schotting et al.*, 1999, *Watson et al.*, 2002]. At this stage, we assume that the Fick's law is valid in order to avoid the use of an additional parameter. Because of this non-linear coupling, codes based on standard numerical schemes require often very fine spatial and time discretizations and therefore a lot of computational time to reproduce experiments. A numerical code based on Mixed Finite Elements (MFE) for the fluid flow problem and a combination of Discontinuous Galerkin (DG) and Multi-Point Flux Approximation (MPFA) methods for the transport was used for the simulation of the described benchmark experiments [*Ackerer and Younes*, 2008]. Flow, advection and dispersion were solved using different numerical methods specifically suited to achieving high accuracy for every kind of equation. The MFE method was used for the discretization of the flow equation since it is locally conservative and leads to accurate and consistent evaluation of the velocity field even in highly heterogeneous domains [*Durlofsky*, 1994]. The mixed method was combined with a mass lumping procedure [*Younes et al.*, 2006] to avoid over- and undershoots when the time step was too small. For the transport equation, it is known that if advection is

dominant, standard numerical methods, such as finite elements or finite volumes, generate solutions with numerical diffusion and/or non-physical oscillations. For these problems, the DG methods have been proven to be clearly superior to the already existing Finite Element methods [Arnold *et al.*, 2002]. DG leads to a high-resolution scheme for advection that maintains the local conservation of Finite Volume (FV) methods but allows high order approximations to enter through a variational formulation rather than by some hybridized difference or functional reconstruction [Kirby, 2000]. Ackerer and Younes [2008] combined the upwind DG method for the advection equation with the MPFA method for the dispersion equation. The MPFA method is preferred to the mixed method because it uses the same type of unknowns (average value per element) as DG, and therefore, both discretizations can be gathered into one system matrix. A θ -scheme (a combination between implicit and explicit Euler schemes) time discretization was used for advection and a fully implicit scheme for dispersion. Advective explicit schemes ($\theta = 0$) combined with a slope limiting technique gave accurate results with very limited numerical diffusion. However, with these schemes, the sub-time step of the transport was restricted (for reason of stability) by the Courant-Friedrich-Lewy (*CFL*) condition ($CFL = 1/2$). Younes and Ackerer [2008] showed that the scheme $\theta = 0.6$ is a good alternative to the fully explicit scheme, especially for highly unstructured meshes. In this study, numerical simulations were performed with $\theta = 0.6$ for advection. For the sake of accuracy, the transport sub-time step was limited to $CFL = 20$. The non-linear flow-transport system was linearized with a Picard scheme (fixed point) and solved iteratively. The flow and transport systems obtained were solved using the combined unifrontal/multifrontal UMFPACK sparse direct solver [Davis and Duff, 1997]. Direct solvers were well adapted since the structures of the flow and transport matrices were constant during the simulation. Moreover, the coefficients of the transport matrix are constant during transport sub-time steps. Therefore, the transport matrix can be factorized only for the first sub-time step. The global time step management during the simulation was of the heuristic type. The convergence was reached if the maximum change inside the domain on the pressure head and concentration was less than a fixed tolerance (absolute value of 10^{-5} in this work, which ensures a small residual). If the convergence is not reached after 20 iterations, the time step was divided by 2.

A variant of this numerical code can be obtained easily by reducing the spatial order of the DG method from piecewise linear to constant approximation. The obtained scheme corresponds to the standard upwind FV scheme for advection. This code imitates the behaviour of standard numerical codes.

The two codes MFE_DG_MPFA and MFE_FV_MPFA based on the MFE method for the flow, DG or FV for advection and MPFA for dispersion were used for the simulation of the laboratory-scale benchmark experiments. The results were compared to measured isolines and BTCs in order to provide an objective evaluation of the codes.

III.1.6 Simulation results

Figure III.6 shows the geometries of the domains for the numerical translation of the experimental setups. Note that the positions of the inflow and outflow openings are given as center points of the openings, and the diameter is 0.9 cm. Constant flux boundary conditions were applied to O7 according to the measured fluxes in Table III.1. While the experiments were conducted in a tank with a thickness of 4 cm, the simulations were

performed for a 2D geometry and therefore the converted volumetric flow rate used for the simulation of the experiments are given in cm^2/min in Table III.1.

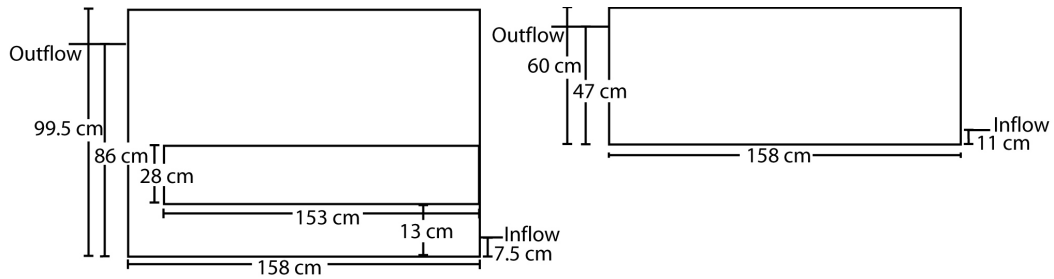


Figure III.6: Simulation domains for EXP_C/d and EXP_H/d. The diameter of the inflow and outflow holes is 0.9 cm.

An arbitrary constant head was assigned to the inflow opening I1 or I3. This combination of boundary conditions was used for the simulation because the pressure head at the outflow changed due to the rising saltwater, whereas a constant but unknown head could be assumed at the inflow opening which was connected to the pump. Therefore, a volumetric flux was used as boundary condition. No flow boundary conditions were forced at the residual edges of the computational domain. The initial condition used was a freshwater domain with $C = 0$ in the porous medium, and the simulation started at the time when the saltwater entered the domain. Table III.2 indicates the experimental parameters, and average values were used for the simulation of both experiments, EXP_Hd and EXP_Cd.

Table III.2: Experimental parameters.

Parameter	Units	Range	Value for simulation	Determination method
Permeability	m^2	2.6×10^{-10} – 4.0×10^{-10}	3.4×10^{-10}	In situ method, column experiments and empirical equations
Longitudinal dispersivity α_L	mm		0.6	Tracer experiment
Dispersivity ratio $\alpha_T = \alpha_L$	-	1/20 – 1/6	1/10	Tracer experiment, literature
Porosity	-	0.37 – 0.38	0.375	Tracer experiment, volumetric and gravimetric measurements
Density saltwater Exp_Hd	g/l	1062 – 1064	1063	Pycnometer, volumetrically
Density saltwater Exp_Cd	g/l	1062 – 1064	1063	Pycnometer, volumetrically
Density freshwater	g/l	-	998	Pycnometer, literature
Diffusion coefficient	m^2/s	0.7×10^{-9} – 1.1×10^{-9}	0.9×10^{-9}	Literature
Dynamic Viscosity	Kg/m s	-	0.001	Literature

Using the MFE_DG_MPFA code, the grid convergence and the sensitivity of the results to parameter uncertainty within the intervals in Table III.2 was analyzed. Irregular triangulated meshes with grid refinement at the outlet were used for the simulations. The main results are:

By varying the grid size between 5000 and 40000 elements, convergence was achieved for around 8000 elements for both EXP_Hd and EXP_Cd. The parameter uncertainty analysis revealed that the extreme parameter constellations of permeability and porosity, maximum porosity with minimum permeability and vice versa, were the most sensitive constellations. Further, α_1 was sensitive at some observation points. For the following discussion, we used the 8000 grid for the simulation of EXP_Hd and EXP_Cd with MFE_DG_MPFA code. The MFE_FV_MPFA code was used with 20000 elements. The grids provided a comparable number of unknowns for both codes. The calculated BTCs were taken from the elements enclosing the photometric observation points. These elements had almost the same size and the same center of gravity as the physical observation points. The measured concentration isolines of 2, 10, 50 and 80% (C/C_{\max}) were compared to the simulated isolines. The MFE_DG_MPFA code simulated the tracer experiments EXP_H/EXP_C accurately, without density contrast, for the rectangular and the complex setup. Both BTCs at various points and isolines fit well with the experimental data. This indicates that the parameters are well estimated.

The simulation results of the EXP_Hd experiment with the MFE_DG_MPFA reproduced the concentration isolines well after 10, 25, 45 and 55 min (Figure III.7). The simulated and experimental 50 and 80% isolines were in very good agreement and small differences could be seen for the 2 and 10% isolines, especially in the center of the tank after 45 min. In Figure III.7, the results with the MFE_FV_MPFA code show a good agreement of the 50% isoline at different simulation times. The MFE_FV_MPFA code reproduced the 50% isolines almost as well as the MFE_DG_MPFA code. However, large inaccuracies resulted in the case of small concentrations, especially for the 2% isoline. This phenomenon was due to numerical diffusion and showed that the 50% isoline was not sufficient to test numerical results.

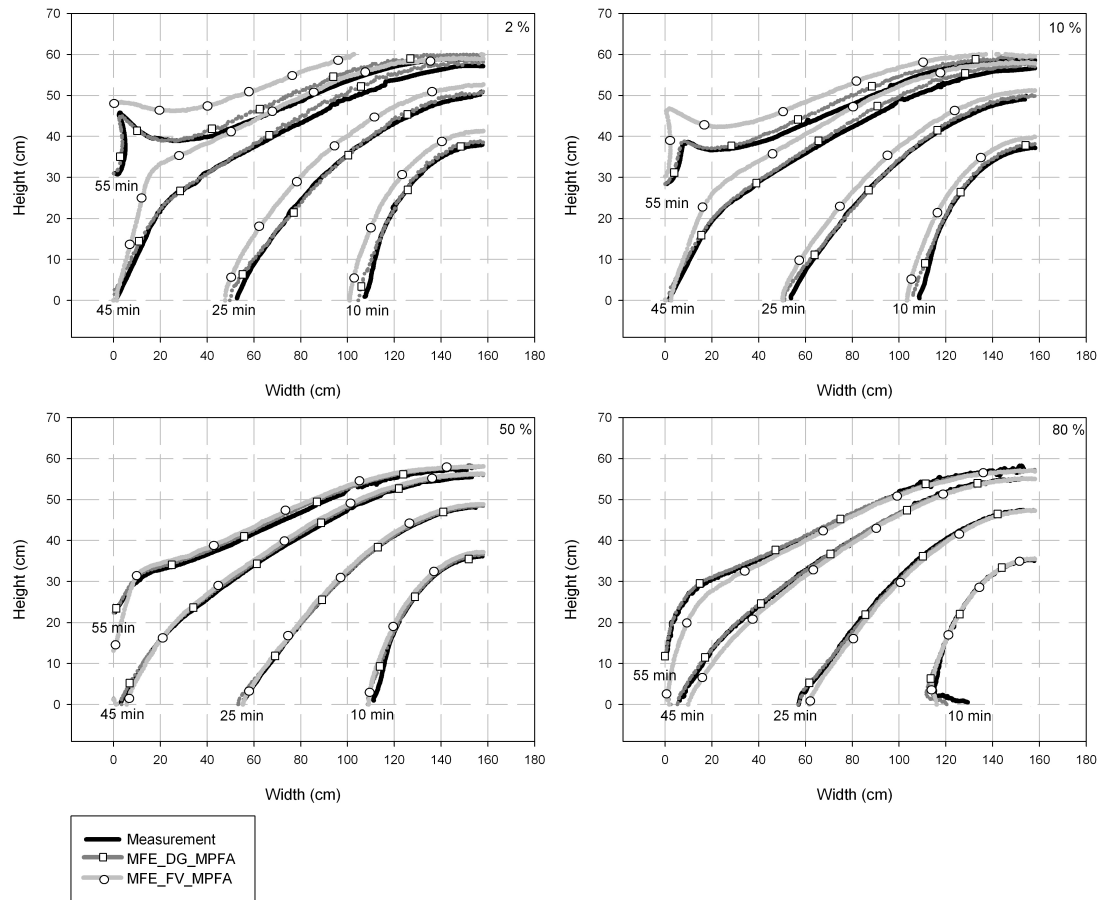


Figure III.7: Comparison of simulated and measured isolines of EXP_Hd.

Note that in Figure III.7, the shape of the 80% isoline after 10 min indicates that the high concentration plume slows down at the bottom of the tank and moves fastest around 4 cm above it. This was well reproduced by the MFE_DG_MPFA code. The simulated spatial concentration distribution after 10 min in Figure III.8 exhibits these patterns for concentrations higher than 80%. The phenomenon was also reproduced but less pronounced by the MFE_FV_MPFA code. A number of BTCs spread along the tank were analyzed. In most cases, the simulations with the MFE_DG_MPFA code fitted well with the measurement and we present four selected points in this paper. P1 was located close to the entry and to the bottom of the tank (Figure III.9).

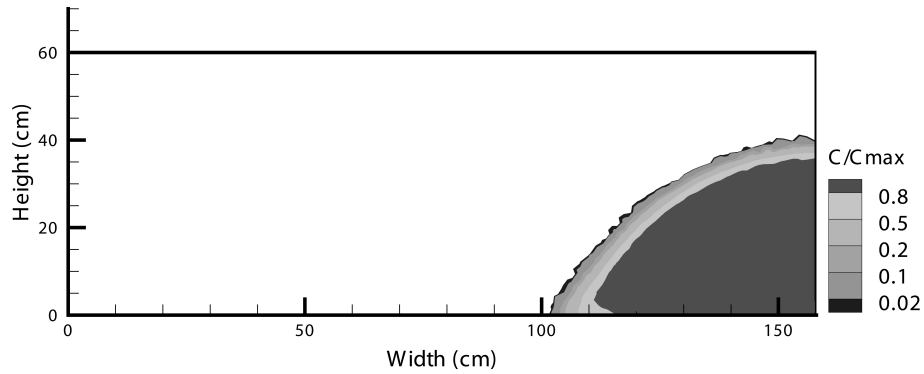


Figure III.8: Spatial concentration distribution after 10 min simulated with MFE_DG_MPFA.

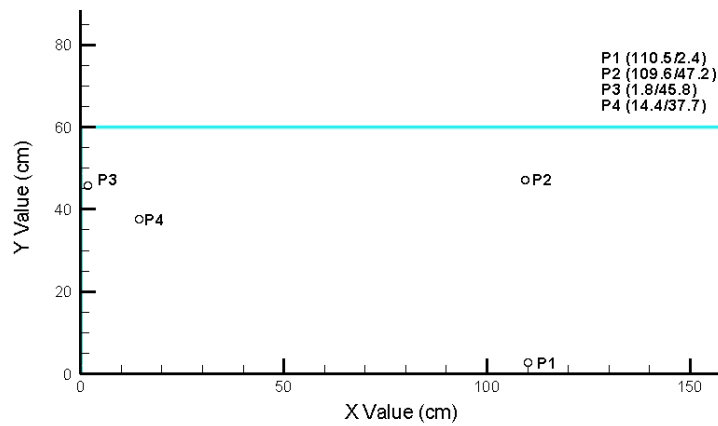


Figure III.9: Observation points for EXP_H and EXP_Hd; coordinates are given in cm.

Both codes gave results in very good agreement with the experimental curve (Figure III.10). The delay of high concentrations as observed in the isoline after 10 min (Figure III.7) could be seen in the BTC as well. The comparison of simulated and measured 2% isolines showed small differences in the center of the tank between experiments and MFE_DG_MPFA results. Therefore, observation point P2 was placed close to the front obtained at 55 min (Figure III.9). The results at this point were very sensitive. The MFE_DG_MPFA results were close to the experimental curve with a small overestimation of the velocity, whereas MFE_FV_MPFA showed strong numerical diffusion smearing the front (Figure III.10). P3 was located at the outlet O7, and P4 was chosen as a point close to the wave structure after 55 min. Both points were well simulated with the MFE_DG_MPFA. The MFE_FV_MPFA failed to reproduce the BTCs. Concentration was also measured at the outlet with a resistivity cell. However due to imperfect mixing, these measurements were not reliable.

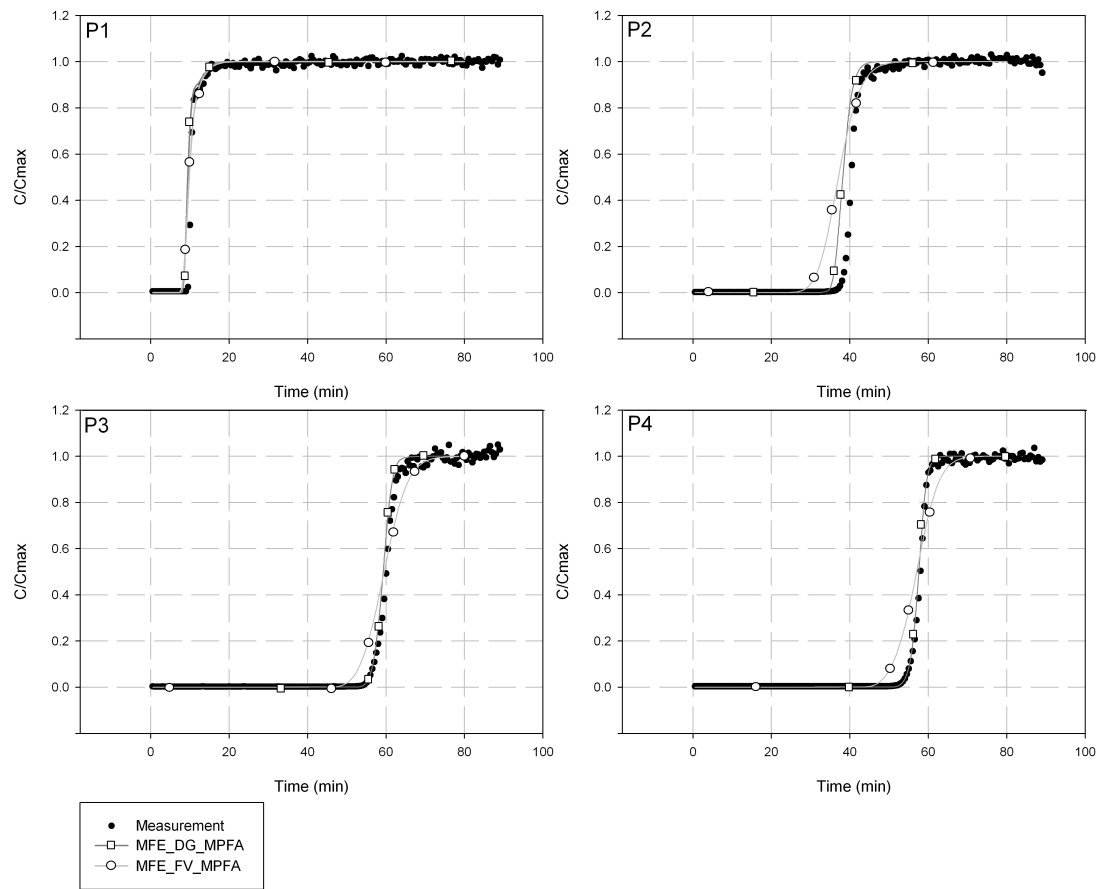


Figure III.10: Comparison of simulated versus measured BTCs for EXP_Hd.

Concerning the computational time, the MFE_DG_MPFA code with $\theta = 0.6$ on the 8000 elements mesh reduced the simulation time by about three times compared to the explicit scheme ($\theta = 0$). The MFE_FV_MPFA code with $\theta = 0.6$ for the 20000 element mesh required about 70% more computational time than the MFE_DG_MPFA code with the semi implicit time stepping ($\theta = 0.6$) on the 8000 elements mesh.

The simulations of EXP_Cd were conducted with the same parameters as for EXP_Hd. In Figure III.11, isolines of the region above the impermeable layer are shown for 30, 40, 50 and 75 min. The 50 and 80% isolines were well simulated by both codes.

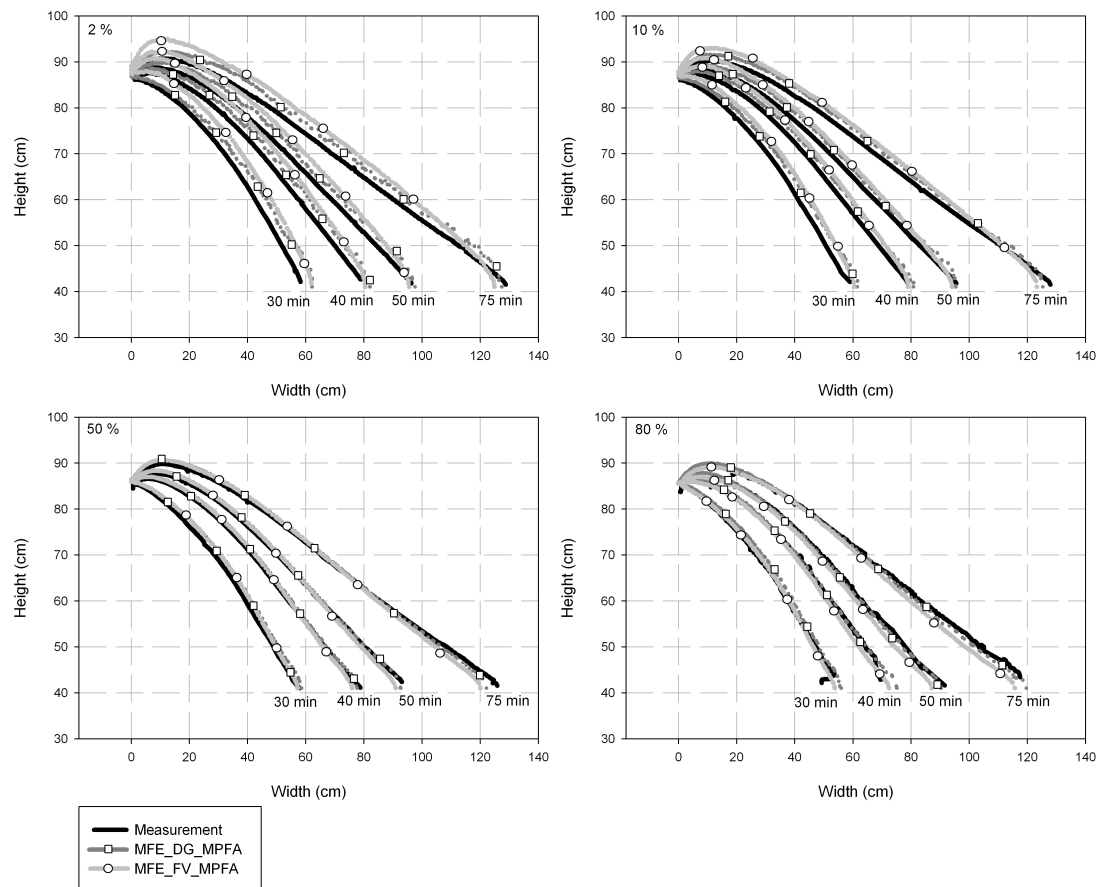


Figure III.11: Comparison of simulated and measured isolines of EXP_Cd.

Low concentration isolines (especially the 2%) show minor differences between simulated and experimental contours. The results of the MFE_DG_MPFA code with 8000 elements were closer to experimental curves than the MFE_FV_MPFA code with 20000 elements. Experimental and simulated BTCs are given in Figure III.12 for different points in the tank (Figure III.13).

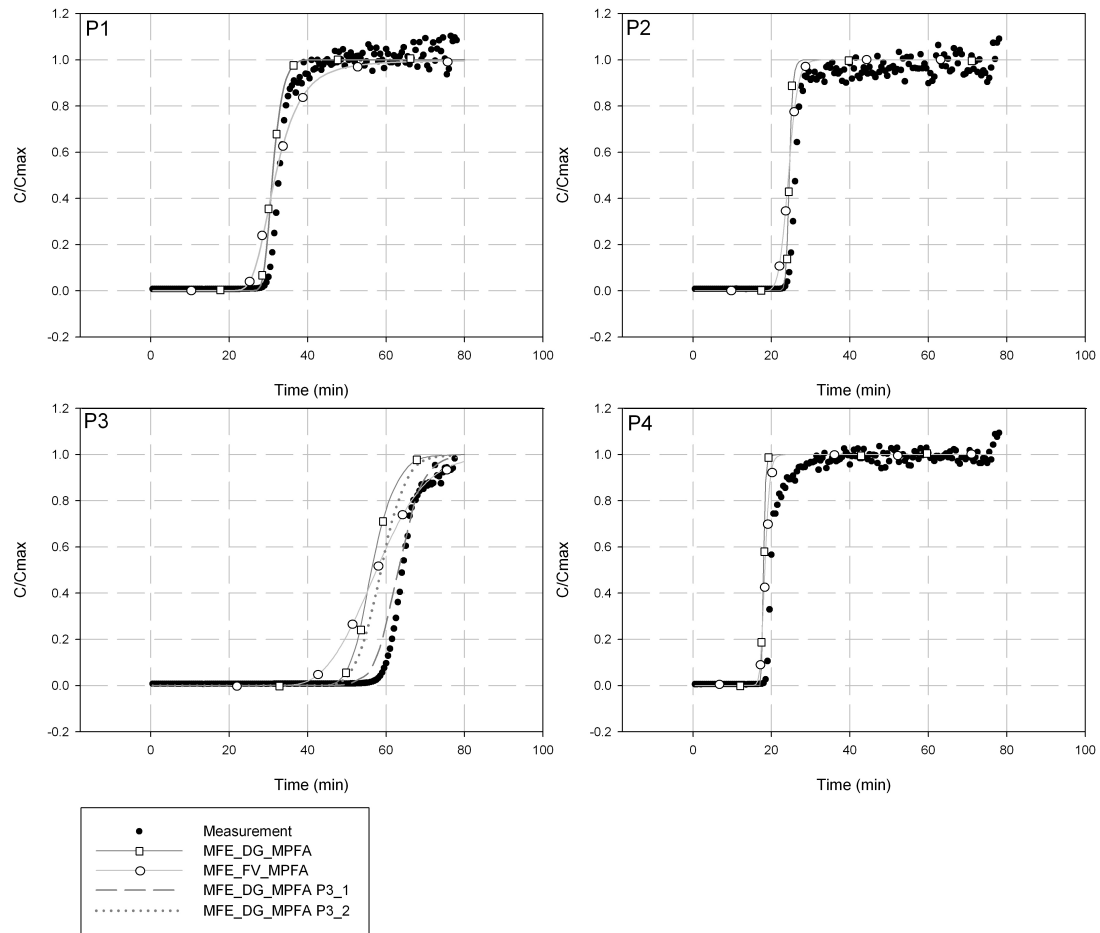


Figure III.12: Comparison of simulated versus measured BTCs for EXP_Cd.

Here, the points P1 and P2 were located close to the outlet. P1 was closer to the front (after 75 min) and was highly sensitive to dispersivity and grid size. A good agreement was obtained between simulated and experimental curves for these points. The results of the MFE_FV_MPFA code with 20000 elements contained some numerical diffusion, in contrast to the MFE_DG_MPFA results. P3 was located close to the front obtained at 75 min (Figure III.13). The MFE_FV_MPFA results showed a large amount of numerical diffusion, whereas the MFE_DG_MPFA curve arrived earlier than the experimental BTC but reproduced its shape. Figure III.12 also compares the simulated BTCs of adjacent grid elements. Although the distance between the elements' centers was less than 1 cm, large differences could be observed between the simulated curves. The BTC P3_1 in Figure III.12 was derived from the element right above P3 and agreed better with the observation. P3_2 was the element below P3 and showed inaccuracies comparable to those of P3. Since P3 was close to the transverse front, this point was very sensitive and the BTC was difficult to reproduce. The other points presented did not exhibit such a behavior. Finally, P4 was located right above the impermeable layer and showed comparable slowdown of high concentration ascent (between 0.8 and 1) as P1 in

EXP_Hd (Figure III.10). Both MFE_DG_MPFA and MFE_FV_MPFA delivered comparable results but fail to reproduce the shape of the BTC between 0.8 and 1.

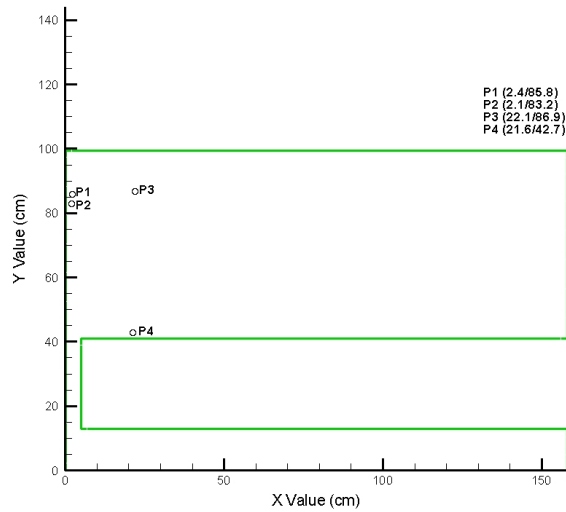


Figure III.13: Observation points for EXP_C and EXP_Cd; coordinates are given in cm.

As a result of the simulations in both experiments, it can be concluded that the MFE_DG_MPFA $\theta=0.6$ is efficient and leads to accurate results. For comparable accuracy, this code requires significantly fewer elements and less computational time compared to the MFE_FV_MPFA method. The agreement for most of the observation points was satisfactory, and even the specific patterns of the isolines could be reproduced well. The MFE_FV_MPFA code generates higher numerical diffusion, but provides a good simulation of the advection-dominated 50% isolines. Interestingly, larger differences were obtained between the MFE_DG_MPFA and MFE_FV_MPFA codes for EXP_Hd (see 2% isolines in Figures III.7 and III.11). This experiment is therefore more sensitive to numerical diffusion than EXP_Cd.

III.1.7 Conclusions and Discussion

A series of 2D laboratory-scale porous medium tank experiments was conducted to study density-driven flow problems based on well-defined experimental parameters and boundary conditions. The experiments were carried out in a flow tank with a rectangular (EXP_H and EXP_Hd) and a more complex (EXP_C and EXP_Cd) geometrical setup aiming to represent natural geological systems. A photometric method was used to study the temporal and spatial plume evolutions. This method is suitable for deriving isolines for 2, 10, 50 and 80% salt concentration with appropriate accuracy and a maximum error for intensity measurements of 3% overestimation. This results in 4% concentration underestimation due to lens flare in the beginning of the experiments. The temporally high-resolution image analysis technology facilitates the assessment of BTCs at relevant positions determined after the experiment in the post processing of the images. It is possible to derive the BTCs at positions where the simulation of the isolines fails, and they provide more detailed data for the evaluation of the code. The tank dimension enables the development of complex flow patterns and a significant spread of the front can be observed, such as the wave structure in EXP_Hd. The comparison of saltwater and

freshwater experiments with equal flow boundary conditions demonstrates the relevance of the density effects for the transport processes. The experimental systems proved to be highly sensitive to density effects both in the rectangular and the complex setups.

Simulations of the experiments were performed with a numerical code based on Mixed Finite Elements (MFE) for the flow, a θ -scheme upwind Discontinuous Galerkin Method (DG) for advection and an implicit Multi Point Flux Approximation (MPFA) method for dispersion. Simulations revealed the sensitivity of the codes to the wave pattern of EXP_Hd. Comparing the simulations of the two different geometrical setups, EXP_Hd turns out to be much more demanding for the numerical code than EXP_Cd. Good agreement is obtained for isolines and BTCs at different points using a mesh of 8000 elements, and even specific patterns of the isolines are well reproduced without any model calibration. Furthermore, non-linear Fickian dispersion could not be detected at this stage. The simulation with a variant of the code using the Finite Volume method (FV) instead of DG on a finer mesh of 20000 elements accurately reproduces the 50% isoline. However, due to numerical diffusion, large inaccuracies are obtained for the 2% and 10% isoline and BTCs. This shows the need to use robust numerical schemes for the simulation of density-driven flow problems, and highlights the quality of the very detailed experiments for benchmarking numerical codes.

Simulation results suggest using the MFE_DG_MPFA code to simulate the transport phenomena on the regional scale. The salt concentrations in the upper aquifer system east of Basel are an indicator of halite dissolution in the lower aquifer and can therefore be used to monitor the subsrosion process. The complex experiment, EXP_Cd, has shown that the salt distribution above the impermeable layer differs significantly from the tracer distribution and a larger part of the aquifer is affected by the saltwater. Further, higher salt concentrations can be expected at the bottom of the upper aquifer. Therefore, the visualization of the experimental plume patterns gives a better idea of the requirements of an effective regional- scale groundwater and subsrosion monitoring system. These systems should be planned on the basis of numerical simulations at the regional scale. Regarding subsidence hazard areas, the following questions should be raised and treated numerically:

- Under which conditions can saltwater reach the pumping wells from the lower aquifer through the fault zones?
- What are the driving forces for the subsrosion process, tectonical setting or water withdrawal?
- Where should salt concentration measurements be taken to monitor the subsrosion process in the lower aquifer?

The presented benchmark experiments are therefore a useful tool to test the reliability of numerical simulations under more realistic geometric conditions being more representative of regional-scale problems.

III.1.8 References

Ackerer, P., and A. Younes (2008), Efficient approximations for the simulation of density driven flow in porous media, *Advances in Water Res.*, 31, 1, 15-27.

Arnold, D.N., F. Brezzi, B. Cockburn, and L.D. Marini (2002), Unified analysis of discontinuous Galerkin methods for elliptic problems, *SIAM J.Numer. Anal.*, 39, 5, 1749-1779.

- Bear, J. (1972), Dynamics of Fluids in Porous Media, *Elsevier, New York*.
- Davis, T.A., and I.S. Duff (1997), A combined Unifrontal/Multifrontal method for unsymmetric sparse matrices, *Technical Report TR-97-016*, Computer and Information Science and Engineering Department, University of Florida.
- Diersch, HJ., and O. Kolditz (2002), Variable-density flow and transport in porous media: approaches and challenges, *Advances in Water Res.*, 25, 899-944.
- Durlofsky, L.J. (1994), Accuracy of mixed and control volume finite element approximations to Darcy velocity and related quantities, *Water Resour. Res.*, 30, 4, 965-973.
- Elder, J.W. (1967), Transient convection in a porous medium, *J. Fluid Mech.* 27, 3, 609–623.
- Gheith H.M., and F.W. Schwartz (1998), Electrical and visual monitoring of small-scale three-dimensional experiments, *Journal of Contaminant Hydrology*, 34, 191–205.
- Goswami, R., and P. Clement (2007), Laboratory-scale investigation of saltwater intrusion dynamics, *Water Resour. Res.* 43, W04418.
- Harleman, D.R.F., and R.R. Rumer (1963), Longitudinal and lateral dispersion in an isotropic porous medium, *J. Fluid Mech.*, 16, 3, 385–394.
- Hassanizadeh, S. M. and A. Leijnse (1988), On the modelling of brine transport in porous media, *Water Resour. Res.*, 24, 21–330.
- Hassanizadeh, S. M., and A. Leijnse (1995) A non-linear theory of high-concentration-gradient dispersion in porous media, *Advances in Water Resour.*, 18, 4, 203-215.
- Henry, H. R. (1964), Effects of dispersion on salt encroachment in coastal aquifers, in *Seawater in Coastal Aquifers, U.S. Geol. Surv. Supply Pap.*, 1613-C, 70-84.
- Huang, W.E., S.E. Oswald, D.N. Lerner, C.C. Smith, and C. Zheng (2003), Dissolved oxygen imaging in a porous medium to investigate biodegradation in a plume with limited electron acceptor supply, *Environ. Sci. Technol.*, 37, 9, 1905–1911, doi: 10.1021/es020128b.
- Huyakorn, P.S., P.F. Anderson, J.W. Mercer, and H.O. White (1987), Saltwater intrusion in aquifers: development and testing of a three-dimensional finite element model, *Water Resour. Res.*, 23, 2, 293–312.
- Jiao C.Y., and H. Hötzl (2004), An experimental study of miscible displacements in porous media with variation of fluid density and viscosity. *Transport in Porous Med.*, 54, 125–44.

- Johannsen, K., W. Kinzelbach, S. Oswald, and G. Wittum (2002), The saltpool benchmark problem – numerical simulation of saltwater upconing in a porous medium, *Advances in Water Res.*, 25, 335–348.
- Kirby, R. (2000), A Posteriori Error Estimates and Local Time-Stepping for Flow and Transport Problems in Porous Media, Ph.D thesis, *University of Texas at Austin*.
- Konz, M., P. Ackerer, E. Meier, P. Huggenberger, E. Zechner, and D. Gechter (2008a), On the measurement of solute concentrations in 2-D flow tank experiments. *Hydrol. Earth Syst. Sci.*, 12, 727-738.
- Konz, M., P. Ackerer, P. Huggenberger, and C. Veit (2008b), Comparison of light transmission and reflection techniques to determine concentrations in flow tank experiments, submitted to *Exp. in Fluids*.
- Ludwig, R., K. Schelkes, P. Vogel, and J. Wollrath (2001), Implications of large scale heterogeneities for hydraulic conductivity model studies at the potential site of a radioactive waste repository at Gorleben, Germany, *Eng. Geol.*, 61 (2-3), 119-30.
- McNeil, J.D., G.A. Oldenborger, and R.A. Schincariol (2006), Quantitative imaging of contaminant distributions in heterogeneous porous media laboratory experiments, *J. Contam. Hydrol.*, 84 , 36-54.
- OECD (Ed.) (1988), Hydrocoin Project, The International Hydrocoin Project, Level 1: Code Verification, OECD, Paris, France.
- Oltean, C, F. Golfier, and M.A. Buès (2008), Experimental and numerical study of the validity of Hele–Shaw cell as analogue model for variable-density flow in homogeneous porous media, *Advances in Water Res.*, 31, 82–95
- Oostrom, M., J.H. Dane, O. Guven, and J.S. Hayworth (1992), Experimental investigation of dense solute plumes in an unconfined aquifer model, *Water Resour. Res.* 28, 2315– 2326.
- Oswald, S., and W. Kinzelbach (2004), Three-dimensional physical benchmark experiments to test variable-density flow models, *J. Hydrol.* 290, 22–42.
- Oswald, S., M. Spiegel , and W. Kinzelbach (2007), Three-dimensional saltwater–freshwater fingering in porous media: contrast agent MRI as basis for numerical simulations, *Mag. Reson. Imaging*, 25, 4, 537 – 540.
- Pearl, Z., M. Magaritz, and P. Bendel (1993), Nuclear magnetic resonance imaging of miscible fingering in porous media, *Transp. Porous Media*, 12, 107–123.
- Perkins, T.K., and Q.C. Johnston (1963), A review of diffusion and dispersion in porous media, *Soc. Petrol. Engrs. J.*, 3, 1, 70–86.

Rahman, A., S. Jose, W. Nowak, and O. Cirpka (2005), Experiments on vertical transverse mixing in a large-scale heterogeneous model aquifer, *J. Contam. Hydrol.*, 80, 130–148.

Schincariol, R.A., and F.W. Schwartz (1990), An experimental investigation of variable density flow and mixing in homogeneous and heterogeneous media, *Water Resour. Res.*, 26, 2317-2329.

Schotting RJ, H. Moser, and S.M. Hassanizadeh (1999), High-concentration gradient dispersion in porous media: experiments, analysis and approximations. *Advances in Water Resour.*, 22, 665–80.

Simpson, M.J., and T.P. Clement (2003), Theoretical analysis of the worthiness of Henry and Elder problems as benchmarks of density-dependent groundwater flow models, *Advances in Water Res.*, 26, 17–31.

Simpson M.J., and T.P. Clement (2004), Improving the worthiness of the Henry problem as a benchmark for density-dependent groundwater flow models, *Water Resour. Res.*, 40, W01504.

Spotte I., E. Zechner, and P. Huggenberger (2005), The southeastern border of the Upper Rhine Graben: A 3D geological model and its importance for tectonics and groundwater flow, *Int. J. of Earth Sciences*, 94, 580-593.

Swartz, C.H., and F.W. Schwartz (1998), An experimental study of mixing and instability development in variable-density systems, *J. Contam. Hydrol.*, 34, 169-189.

Watson, S.J., D.A. Barry, R.J. Scotting, and S.M. Hassanizadeh (2002), Validation of classical density-dependent theory for stable, high-concentration gradient brine displacements in coarse and medium sand. *Advances in Water Resour.*, 25, 611–35.

Wooding R.A., S.W. Tyler, and I. White (1997), Convection in groundwater below evaporating salt lake: 1. Onset of instability. *Water Resour Res.*, 33, 1199–217.

Younes A., P. Ackerer, and F. Lehmann (2006), A new mass lumping scheme for the mixed hybrid finite element method, *Int. J. for Num. Methods in Eng.*, 67, 1, 89-107.

Younes A., and P. Ackerer (2008), Solving the Advection-Dispersion Equation with Discontinuous Galerkin and Multipoint Flux Approximation methods on unstructured meshes, *Int. J. for Num. Methods in Fluids*, published online in Wiley Inter Science DOI: 10.1002/fld.1783.

Zhang Q., R.E. Volker, and D.A. Lockington (2001), Influence of seaward boundary condition on contaminant transport in unconfined coastal aquifers, *Journal of Contaminant Hydrology*, 49, 201-215.

IV. Experiments and simulations of 2D-density flow problems in heterogeneous porous media.

Paper published in *Journal of Contaminant Hydrology*

Variable-density flow in heterogeneous porous media – Laboratory experiments and numerical simulations

Konz, M.⁽¹⁾; Younes, A.⁽²⁾; Ackerer, P.⁽²⁾; Fahs, M.⁽²⁾; Huggenberger, P.⁽¹⁾; Zechner, E.⁽¹⁾

⁽¹⁾Department of Environmental Sciences, University of Basel, Institute of Geology, Applied and Environmental Geology, Basel, Switzerland

⁽²⁾ Université Louis Pasteur, Institut de Mécanique des Fluides et des Solides, CNRS, UMR 7507, Strasbourg, France

IV.1 Variable-density flow in heterogeneous porous media – Laboratory experiments and numerical simulations

IV.1.1 Abstract

In *Konz et al.* [2009a], a series of laboratory-scale 2D tank experiments were conducted and accurately simulated for density driven flow problems on homogeneous porous media. In the present work, we extended the numerical and experimental studies to heterogeneous problems. The heterogeneous porous medium was constructed with a low permeability zone in the centre of the tank and had well-defined parameters and boundary conditions. Concentration distributions were measured in high resolution using a photometric method and an image analysis technique. The numerical model used for the simulations was based on efficient advanced approximations for both spatial and temporal discretizations. The Method Of Lines (MOL) was used to allow higher-order temporal discretization. Three different boundary conditions, corresponding to different localizations of the inflow and the outflow openings at the opposite edges of the tank, were applied to investigate different flow scenarios in the heterogeneous porous medium flow tank. Simulation results of all three density coupled experiments revealed a density-dependent behavior of dispersion. Thus, a reduction of dispersivities was required to obtain a good matching of the experimental data. The high quality of the experiments enabled a detailed testing of numerical variable-density flow codes under heterogeneous conditions. Therefore, the experiments were considered to be reliable benchmark tests.

IV.1.2 Introduction

Density differences of fluids can alter the flow dynamics of the entire flow system. In groundwater sciences variable-density flow phenomena may be expected in landfill leachate, sewage plumes and seawater intrusion into coastal aquifers [e.g. *Huyakorn et al.*, 1987; *Ludwig et al.*, 2001; *Masciopinto*, 2006; *Gemitzi and Tolikas*, 2007]. Issues concerning geomechanical stability of halite bearing horizons have also encouraged research in density-coupled flow [*Konz et al.*, 2009a]. However, modeling density-driven flow in porous media remains challenging, due to the non-linear coupling between flow and transport [*Diersch and Kolditz*, 2002; *Johannsen et al.*, 2002, *Oswald and Kinzelbach*, 2004]. Hence, in order to evaluate the accuracy of the numerical codes, an increasing number of laboratory-scale experiments exists for 2D and 3D problems [e.g. *Schincariol and Schwartz*, 1990; *Oostrom et al.*, 1992; *Swartz and Schwartz*, 1998; *Oswald and Kinzelbach*, 2004; *Goswami and Clement*, 2007; *Konz et al.*, 2009a]. The laboratory experiments have several advantages: boundary and initial conditions are known, the porous medium properties can be determined separately, and the experiments can be repeated if necessary.

Laboratory experiments on high-concentration-gradient dispersion have shown that density contrasts between fluids in porous media can result in decreased dispersive mixing and smaller effective dispersivities [see *Schotting and Landman*, 2004 for an overview of the topic]. Generally, one-dimensional experiments were performed to study the behavior of dispersion under the influence of high density contrasts [e.g. *Schotting et*

al., 1999; *Watson et al.*, 2002; *Jiao and Hötzl*, 2004]. *Hassanizadeh and Leijnse* [1995] describe a non-linear behavior of dispersion if large density variations occur and develop a non-linear dispersion theory.

In a previous work [*Konz et al.*, 2009a], a series of laboratory-scale 2D tank experiments is presented and accurately simulated for density driven flow problems on homogeneous porous medium. In the present work, we extended the numerical and experimental studies to heterogeneous problems with different boundary conditions. The aim of this study is to provide reliable data for testing numerical codes under heterogeneous conditions and to present suitable simulation methods including adequate parameter values. Hence, an assessment of density-dependent dispersivity is essential for this purpose and was realized by means of a sensitivity analysis for the tracer and the density flow experiments. The first part of the paper describes the experimental setup and the numerical model. The second part analysis the results and discusses the sensitivity of dispersion under the influence of density contrasts.

IV.1.3 Experimental procedures, materials and properties of the porous media

An experimental flow tank (158 cm × 98 cm × 4 cm, see Figure IV.1) was constructed of Plexiglas panes, facilitating the optical observation of dyed plumes.

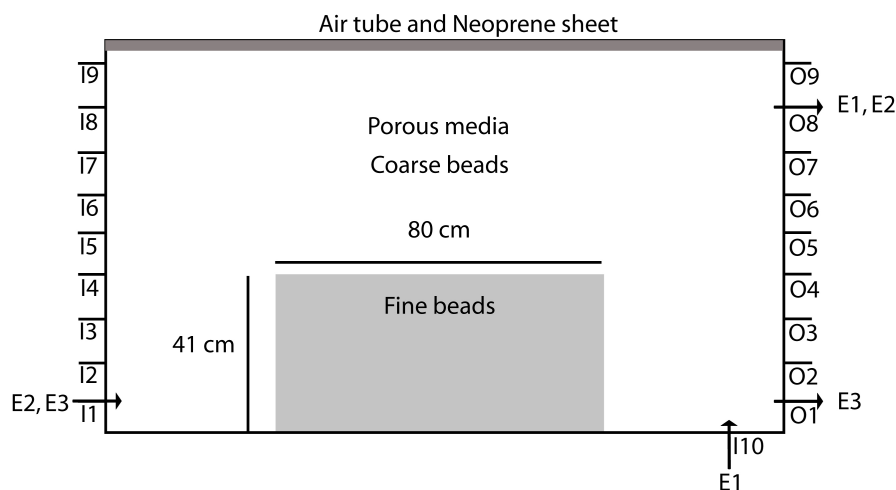


Figure IV.1: Experimental setup with boundary conditions for E1 to E3. Arrows indicate the in- and outflows.

Two glass beads types (SiLi-beads GmbH) were used to establish the heterogeneous porous medium. The fine beads had a mean diameter of 0.6 mm, the coarse beads' diameter was 2 mm. The same photometrical concentration determination method as described in *Konz et al.* [2008, 2009b] was used in the present work. Therefore, we only summarize the most important features of the method and the interested reader is referred to literature for further details. Time lapse photography was applied to monitor the progress of the experiments using a digital camera (Nikon D70). A red food dye (Cochineal Red A, E124) marked the saltwater or acted as a tracer in the density uncoupled experiments. The intensity distribution of the dye was converted to concentrations. The image analysis methodology is based on the non-linear relation of reflected intensity and dye concentration. This relation was determined for each image

pixel specifically by calibration experiments and followed a second order exponential function. The pixel specific calibration is important to avoid influences of spatial heterogeneity in illumination and different background brightness of the coarse and fine beads. Preliminary Darcy column experiments demonstrated that the dye tracer and saltwater show similar flow behaviors and that the dye concentration can be used to derive salt concentrations. The procedure allowed the computation of concentration isolines and breakthrough curves (BTCs). *Konz et al.* [2008] showed that the method is highly accurate although flare effects in the camera lens system can alter the measured intensities. This effect is, however, much smaller for reflection intensities, as used here, compared to transmission intensities. The measurement error is about 1% for the measured intensities [*Konz et al.*, 2009b].

Three different boundary conditions were applied to the porous medium flow tank (E1 to E3 in Figure IV.1). In E1 the solution was injected from the bottom upwards to the outflow opening. In E2 a flow from the lower left side to the upper right side was induced and in E3 the flow was from the lower left side to the lower right side. A constant flow rate was realized by means of a peristaltic pump. The values are given in Table IV.1.

Table IV.1: Flow rates of tracer and density experiments.

Experiment	Flow rate (cm ² /min)
E1_D	28.5
E1_T	30.0
E2_D	28.8
E3_D	27.6
E3_T	29.0

Tracer experiments without density gradients between inflowing solutions and ambient pore water were conducted with red marked (E124) freshwater for each of the three different boundary conditions. These experiments are named E1_T through E3_T in the following discussion. Density-coupled experiments were conducted with a saltwater solution of 1073 g/l density and named E1_D through E3_D.

The porous media parameters of the coarse and fine beads were determined in-situ in the flow tank using pressure and flow measurements to derive the permeability (K) by inverse calibration (Table IV.2, see also *Konz et al.*, 2009a for details). Flow rates and pressure differences between four pressure sensors were measured for various hydraulic gradients forced by fixed heads of the in- and outflow reservoirs. The head differences were significantly higher than the sensitivity of the sensors. Temperature variations of the inflowing water and the water in the tank were minimized by water heating systems and air-conditioning. Permeability values between 2.6×10^{-10} and 4.0×10^{-10} m² were found for the fine beads zone. *Konz et al.* [2009a], who used the same porous medium type for their homogeneous experiments, derived a permeability value of 3.4×10^{-10} m² from tracer experiments in the flow tank and from column experiments. Therefore, we fixed this value for our experiments (see section simulation results). Permeabilities between 2.9×10^{-9} and 3.5×10^{-9} m² were found for the coarse beads zone. The Kozeny-Carman equation also suggests values of permeability for the coarse beads zone to be one magnitude higher than for the fine beads zone.

Porosity could be determined based on volumetric and gravimetric measurements as 0.375 for both zones, which is a common value for uniform artificial glass beads.

Dispersivities were assumed to be proportional to the beads' diameter. A discussion of the values for both zones will follow in section 'simulation results'

Table IV.2: Experimental parameters of the fine and the coarse beads zones.

Parameter	Units	Coarse beads zone	Fine beads zone
Permeability	m ²	$2.9 \times 10^{-9} - 3.5 \times 10^{-9}$	$2.6 \times 10^{-10} - 4.0 \times 10^{-10}$ 3.4×10^{-10}
Bead diameter	mm	2.0	0.6
Dispersivity ratio $\alpha_T = \alpha_L$	-	1/10	1/10
Porosity	-	0.37 - 0.38	0.37 - 0.38
Density saltwater	g/l	1073	1073
Density freshwater	g/l	998	998
Diffusion coefficient	m ² /s	$0.7 \times 10^{-9} - 1.1 \times 10^{-9}$ 0.9×10^{-9}	$0.7 \times 10^{-9} - 1.1 \times 10^{-9}$ 0.9×10^{-9}
Dynamic Viscosity	Kg/m s	0.001	0.001

IV.1.4 Results of experiments

The value of a benchmark problem for testing density-coupled flow models can be assessed by comparing coupled versus uncoupled flow experiments under equal boundary conditions [Simpson and Clement, 2003]. The density effects were visible for all experiments E1_D to E3_D. Figure IV.2 compares the shape of the injected saltwater and tracer plumes of E1 and E3 after 125 min.

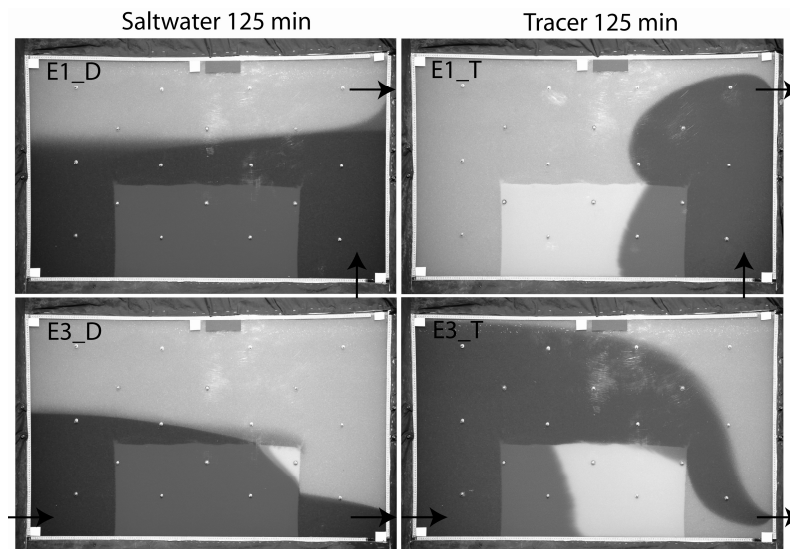


Figure IV.2: Different plume patterns of saltwater experiments (E1_D, E3_D) and freshwater experiments (E1_T, E3_T) showing the effects of density coupling on fluid movements. Arrows indicate inflow and outflow openings.

Due to the gravitational effects, after 125 min the plume in E1_D formed an almost horizontal interface between freshwater and saltwater. The saltwater moved upwards to

the outflow opening and spread horizontally into the fine beads zone, forming a wedge. A sharp interface developed both in the fine and in the coarse beads zone during the experiment (Figure IV.3). Although the average flow velocities were comparable (Table IV.1), the tracer plume in E1_T did not reach the left side of the tank and did not form a wedge in the fine beads zone.

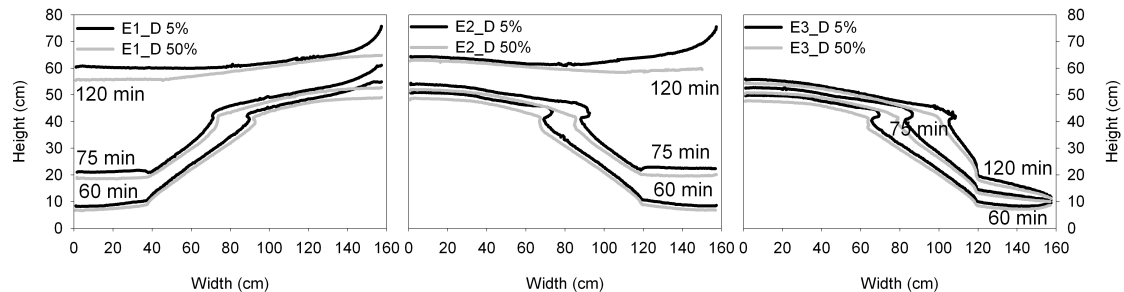


Figure IV.3: Experimental 5% and 50% saltwater isolines of E1_D, E2_D and E3_D at different times.

A spread of the front was observed in E2_D close to the outlet of the tank during the course of the experiment (Figure IV.3). By the end of the experiment (after 200 min), the saltwater formed an almost horizontal front.

In E3_D, the saltwater moved fastest along the bottom of the tank and formed a wedge shape within the low permeability zone, whereas in tracer experiment E3_T the marked freshwater flowed around the low permeability zone in order to reach the outlet. A significant spread of the interface could be observed in E3_D in the coarse beads zone above the fine beads zone (Figure IV.2 and Figure IV.3). Once the saltwater had passed the low permeability zone, a sharp interface formed on the right side beside the low permeability zone.

The sharp interfaces generally formed at a position where the plume moved upwards, e.g. on the right side beside the low permeability zone in E3_D or on the left side beside the low permeability zone in E1_D, whereas a spread could be observed in horizontal flow directions above the fine beads zone. The formation of the sharp interface was expected for the upward movement due to gravitational effects of the high density solution.

The three experimental setups exhibited small instability developments along the horizontal interface between the two beads units although the general fluid stratification can be viewed as stably layered. The formation of unstable situations only depended on the applied boundary conditions, namely the different inflow and outflow opening configurations. The second experimental setup (E2_D) forced a slight instability development at the horizontal interface of the 2 zones. This phenomenon was more pronounced for E3_D (Figures IV.2 and IV.4) where the denser saltwater front overlaid the freshwater due to the higher flow velocities in the coarse beads zone. The development of small gravitational salt fingers started from the interface of the two zones and reached into the fine beads zone (Figure IV.4).

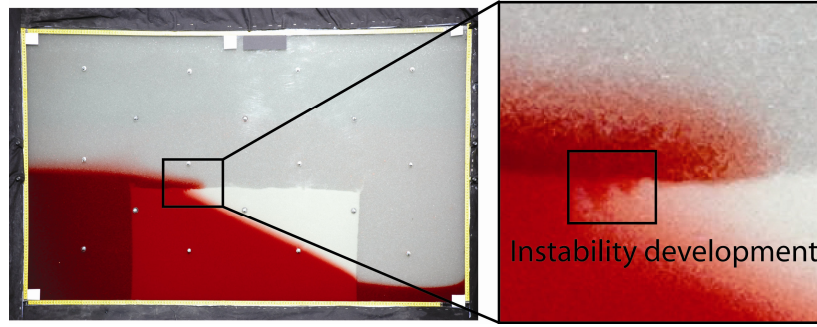


Figure IV.4: Small gravitational salt fingers along the horizontal interface of the two porous media types of E3_D.

4. The Numerical model

Modeling density driven flow problems requires a coupled flow-transport numerical model where the flow system can be written in terms of equivalent fresh water head:

$$\rho S \frac{\partial h}{\partial t} + \varepsilon \frac{\partial \rho}{\partial C} \frac{\partial C}{\partial t} + \rho \nabla \cdot \mathbf{q} = 0 \quad (\text{IV.1})$$

$$\mathbf{q} = -\frac{\rho_0 g}{\mu} \mathbf{k} \left(\nabla h + \frac{\rho - \rho_0}{\rho_0} \nabla z \right) \quad (\text{IV.2})$$

with ρ the fluid density [ML^{-3}], S the specific mass storability related to head changes [L^{-1}], h the equivalent fresh water head [L], t the time [T], ε the porosity [-], C the solute mass fraction [M. salt/M. fluid], \mathbf{q} the Darcy's velocity [LT^{-1}], ρ_0 the density of the displaced fluid [ML^{-3}], g the gravity acceleration [LT^{-2}], μ the fluid dynamic viscosity [$\text{ML}^{-1}\text{T}^{-1}$], \mathbf{k} the permeability tensor [L^2] and z the depth [L].

The solute mass conservation is written in term of mass fraction:

$$\frac{\partial(\varepsilon \rho C)}{\partial t} + \nabla \cdot (\rho C \mathbf{q} - \rho \mathbf{D} \cdot \nabla C) = 0 \quad (\text{IV.3})$$

where the dispersion tensor \mathbf{D} is given by:

$$\mathbf{D} = D_m \mathbf{I} + (\alpha_L - \alpha_T) \mathbf{q} \times \mathbf{q} / |\mathbf{q}| + \alpha_T |\mathbf{q}| \mathbf{I} \quad (\text{IV.4})$$

with α_L and α_T the longitudinal and transverse dispersivities [L], D_m the pore water diffusion coefficient [L^2T^{-1}] and \mathbf{I} the unit tensor.

Flow and transport equations are coupled by state equations linking density and viscosity to mass fraction. We used a linear model for density and a polynomial function for viscosity [Herbert *et al.*, 1988]:

$$\rho = \rho_0 + (\rho_1 - \rho_0)C, \quad \text{and} \quad \mu = \mu_0(1.0 + 0.4819C - 0.2774C^2 + 0.7814C^3) \quad (\text{IV.5})$$

with ρ_1 the density of the injected fluid, ρ_0 and μ_0 the density and viscosity of freshwater. Different state equations may be used for density or viscosity [Diersch and

Kolditz, 2002]. Due to the strong non-linearities, modeling density driven flow problems requires specific numerical methods in order to reduce the large computational requirements while maintaining the accuracy. In this work, we used a robust numerical model developed by *Younes et al. [2009]* with efficient advanced approximations for both spatial and temporal discretizations. In the following, we only summarize the most important features of the model. For the spatial discretization of flow and transport equations, numerical methods that are specifically suited to achieve high accuracy for each kind of equation were applied. Indeed, the Mixed Finite Element (MFE) method was combined with the mass lumping procedure of *Younes et al. [2006]* and applied to the flow equation. For the transport equation, the Discontinuous Galerkin (DG) method was used to discretize the advection equation, and was combined with the Multipoint Flux Approximation (MPFA) method for the discretization of the dispersion equation [*Younes and Ackerer, 2008*]. The DG method leads to a robust and accurate numerical scheme for problems involving sharp fronts [*Shuangzhang and Shahrouz, 2005*]. Furthermore, the MPFA method is locally conservative and handles general irregular grids on anisotropic heterogeneous domains [*Edwards and Rogers, 1998; Aavatsmark, 2002*]. The spatial discretization (MFE_DG_MPFA) based upon the combination of MFE, DG and MPFA methods is robust and accurate for modelling density driven flow problems [*Ackerer and Younes, 2008*]. For the temporal discretization, the Method Of Lines (MOL) was used to improve temporal accuracy and efficiency by the use of adaptive higher-order time discretizations with formal error control. With the MOL, the error checking, robustness, order selection and time step adaptability features available in sophisticated ODE/DAE codes can be applied to the time integration of the coupled system. The MFE_DG_MPFA spatial discretization was solved in time with the recent version of the DLSODIS solver. This solver uses the fixed-coefficient implementation of the implicit BDF method, adapting in both the order of approximation and time step to provide the necessary accuracy, efficiency and robustness. The developed numerical model is much more accurate and efficient than standard methods [*Younes et al., 2009*].

IV.1.6 Simulation results

The boundaries of the low permeability zone were digitized to account for irregularities of the interface between the fine beads block and the high permeability zone. The non-planar interface developed due to the filling procedure, when the beads were placed into the saturated flow tank. This created disturbances of the horizontal interface of the fine beads zone. A mesh of 10000 elements with two zones was used for the simulation. Zone 1 is the high permeability zone and zone 2 the low permeability zone.

IV.1.6.1 Tracer experiments

The tracer experiments were used to refine the permeability value of the coarse beads (estimated to be one magnitude larger than the fine beads' permeability) as well as the values of longitudinal and transverse dispersivities in both zones. We used the 5% and 50% isolines at different time steps for the comparison of numerical and experimental results because the 50% isoline is dominated by advection and therefore alone not suitable to show errors caused by numerical dispersion [*Konz et al., 2009a*].

The parameters were derived from tracer experiments E1_T and E3_T by means of a sensitivity analysis. The following assumptions were made:

- The flow rates at the input opening were measured accurately and should not be included in the sensitivity analysis.
- The conductivity of the low permeability zone is fixed to the value of $3.4 \times 10^{-10} \text{ m}^2$ based on the inverse calibration (see section ‘Experimental procedures, materials and properties of the porous media’) and on previous studies [Konz *et al.*, 2009a]. However, the conductivity of the coarse beads zone is allowed to vary within the range of 2.9×10^{-9} and $3.5 \times 10^{-9} \text{ m}^2$. Therefore, the ratio between both conductivities is variable. Note that since the input flow rate is fixed, the solution is highly sensitive to this ratio.
- The longitudinal dispersivity values in both zones are unknown but assumed to be proportional to the diameter of beads. The transverse dispersivities are assumed to be fixed at 1/10 of longitudinal dispersivities.

The error, Err , of the simulations was calculated by comparing the simulated concentrations, C_i^{num} , of the cells i , crossed by the measured 5% and 50% isolines with the measured concentration C_i^{mes} .

$$Err = \frac{\sum_{i=1}^{nbp} S_i \left(\frac{C_i^{num} - C_i^{mes}}{C_i^{mes}} \right)^2}{\sum_{i=1}^{nbp} S_i} \quad (IV.6)$$

where S_i is the area of the element crossed by the 5% or 50% isoline. The values of dispersivities in the fine beads zone (α_L^1) and coarse beads zone (α_L^2) were obtained using initial values and a reduction coefficient r .

$$\alpha_L^1 = r \times \alpha_L^{1,init}, \quad \alpha_T^1 = \alpha_L^1 / 10 \quad \text{and} \quad \alpha_L^2 = r \times \alpha_L^{2,init}, \quad \alpha_T^2 = \alpha_L^2 / 10 \quad (IV.7)$$

The initial values of dispersivity, $\alpha_i^{1/2,init}$, represented the glass beads’ diameters as suggested by Perkins and Johnston [1963] who analyzed a number of laboratory-scale dispersivity values. Oswald and Kinzelbach [2004] and Goswami and Clement [2007] previously reported relatively small dispersivity values within the range of the grain diameter or smaller for uniform artificial porous medium systems. Commonly, the transverse dispersivity is set to be a small fraction of the longitudinal dispersivity in the range of 1/20 and 1/6 according to Harleman and Rumer [1963] and Huang *et al.* [2003]. Therefore, the transverse dispersivity was assumed to be 1/10 of the longitudinal dispersivity following Johannsen *et al.*, [2002] and Oswald and Kinzelbach [2004]. Results of simulations using different ratios between the conductivities of the porous medium and different reduction coefficients for dispersivities are given in Table IV.3. The best results were obtained for $K1=3.26 \cdot 10^{-9} \text{ m}^2$ and r equal to 50% of the bead diameter. Note that $K1 = 3.16 \times 10^{-9} \text{ m}^2$, $K1 = 3.26 \times 10^{-9} \text{ m}^2$ and $K1 = 3.36 \times 10^{-9} \text{ m}^2$ gave close results. Therefore, only these values of $K1$ were later used for the variable density simulations.

Table IV.3: Results of the sensitivity analysis for the tracer experiments.

K1	r	$Err_{(E1_T)}$	$Err_{(E3_T)}$	$Err_{(E1_T)}+Err_{(E3_T)}$
29.6	100%	0.61	0.45	1.06
-	50%	0.56	0.29	0.85
-	20%	0.57	0.29	0.86
-	10%	0.59	0.32	0.91
30.6	100%	0.39	0.37	0.76
-	50%	0.33	0.2	0.53
-	20%	0.34	0.22	0.56
-	10%	0.35	0.26	0.61
31.6	100%	0.27	0.36	0.63
-	50%	0.22	0.18	0.4
-	20%	0.23	0.2	0.43
-	10%	0.24	0.25	0.49
32.6	100%	0.22	0.39	0.61
-	50%	0.17	0.19	0.36
-	20%	0.18	0.2	0.38
-	10%	0.19	0.25	0.44
33.6	100%	0.2	0.39	0.59
-	50%	0.16	0.21	0.37
-	20%	0.17	0.21	0.38
-	10%	0.18	0.25	0.43
34.6	100%	0.22	0.49	0.71
-	50%	0.17	0.24	0.41
-	20%	0.18	0.24	0.42
-	10%	0.20	0.26	0.46

The simulation with $K1 = 3.36 \times 10^{-9} \text{ m}^2$ and 0.3 mm as longitudinal dispersivity for the fine beads and 1.0 mm for the coarse beads was able to predict accurately the measured 5% and 50% concentration isolines (Figure IV.5).

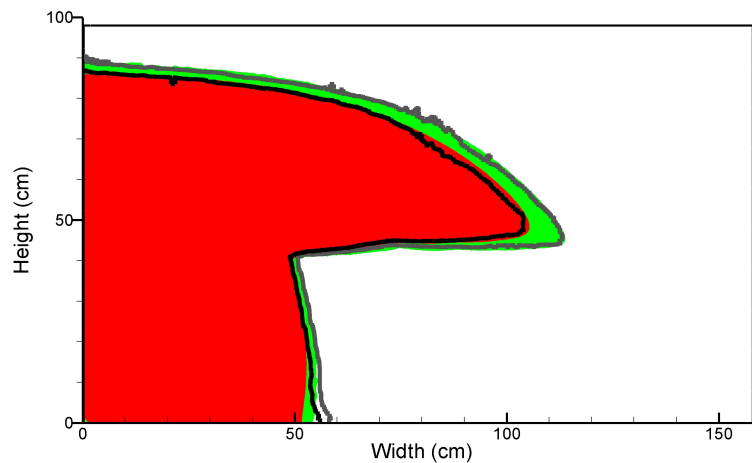


Figure IV.5: Comparison of simulated and experimental (black lines) results of E3_T after 75 min for $K1=3.36 \times 10^{-9} \text{ m}^2$ and $r = 50\%$. The green area indicates concentrations between 5% and 50%, the red area is above 50%.

IV.1.6.2 Density experiments

It is well known that the simulation of density driven flow problems can be highly sensitive to the mesh size [Diersch and Kolditz, 2002]. Therefore, grid convergence was analysed for E1_D, E2_D and E3_D with a first mesh of 10000 elements, a fine mesh of 30000 elements including a local refinement at the interface of the two beads zones and a very fine mesh of 50000 elements. E1_D and E2_D were well simulated with the 10000 elements mesh. Results for E3_D showed that the first mesh was not sufficient to obtain accurate results. In this case, the grid convergence was reached with the second mesh of 30000 elements. Therefore, all simulations for E1_D, E2_D and E3_D were performed using this mesh.

A parameter sensitivity analysis comparable to the one for the tracer experiments was conducted. Due to the strong non-linearities, simulations with the mesh of 30000 elements can be highly CPU consuming. This can cripple the sensitivity analysis which requires a lot of simulations. However, the used numerical model, based on the quasi-Newton method and adaptive higher-order time discretizations with formal error control, is highly efficient. Indeed the simulation of, e.g. E1_D, required 9 min of CPU time whereas, the same simulation required about 4h with a standard scheme based on the well known Picard linearization technique combined with a heuristic time step management (the current time step size is related to the number of iterations required to reach convergence in the previous time step).

For the simulations of the density flow experiments (E1_D to E3_D), the densities of the injected fluids were measured accurately and therefore not included in the sensitivity analysis. The results of the sensitivity analysis using different ratios between the conductivities of the porous medium and different reduction coefficients for dispersivities are given in Table IV.4.

Table IV.4: Results of the sensitivity analysis for the density experiments.

K1	r	$Err_{(E1_D)}$	$Err_{(E2_D)}$	$Err_{(E3_D)}$	$\frac{Err_{(E1_D)}+Err_{(E2_D)}+Err_{(E3_D)}}{Err_{(E3_D)}}$
31.6	100%	1.22	0.6	0.86	2.68
-	50%	0.7	0.23	0.52	1.45
-	20%	0.35	0.1	0.37	0.82
-	10%	0.28	0.12	0.35	0.75
-	5%	0.27	0.13	0.32	0.72
32.6	100%	1.15	0.58	0.83	2.56
-	50%	0.63	0.23	0.5	1.36
-	20%	0.29	0.11	0.37	0.77
-	10%	0.24	0.12	0.34	0.7
-	5%	0.22	0.12	0.3	0.64
33.6	100%	1.1	0.57	0.82	2.49
-	50%	0.57	0.24	0.49	1.3
-	20%	0.25	0.13	0.36	0.74
-	10%	0.21	0.12	0.33	0.66
-	5%	0.2	0.12	0.3	0.62

The best results for variable density experiments were obtained for $K1=3.26 \times 10^{-9} \text{ m}^2$ and $K1=3.36 \times 10^{-9} \text{ m}^2$ with r equal to 5% of the bead diameter. The results were more

sensitive to the values of dispersivity than in the case of the tracer experiments. The simulations indicated that the used numerical model reproduced satisfactorily the density-flow processes in heterogeneous porous media (Figure IV.6). Indeed, Figure IV.6b shows that the characteristic nose of the front in the coarse beads zone above the fine beads zone was well simulated for E3_D with $K_1=3.36 \times 10^{-9} \text{ m}^2$ and $r = 5\%$.

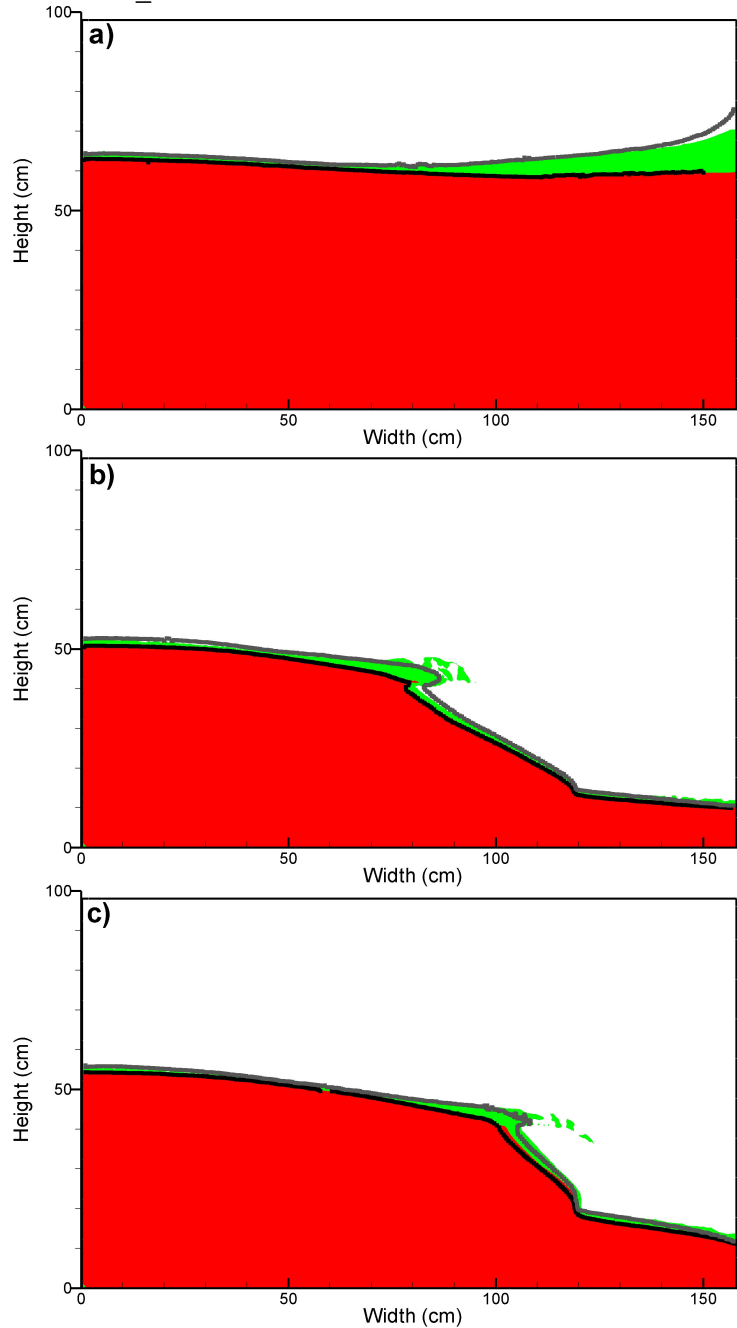


Figure IV.6: Comparison of simulated and experimental (black lines) results for $K_1=3.36 \times 10^{-9} \text{ m}^2$ and $r = 0.05$ of a) E2_D after 120 min, b) E3_D after 75 min and c) E3_D after 120 min. The green area indicates concentrations between 5% and 50% and the red area is above 50%.

As expected, the ‘best fit’ permeability values of zone 1 did not change from the tracer experiments to the density experiments. However, longitudinal dispersivity was 1/10 of the value found for the tracer experiment. This observation is well in line with *Hassanizadeh and Leijnse* [1995] who also observed reduced dispersivity values in their experiments. Simulations of the density experiments using the dispersivity values suggested by the tracer experiments deteriorated the results as shown for E3_D in Figure IV.7.

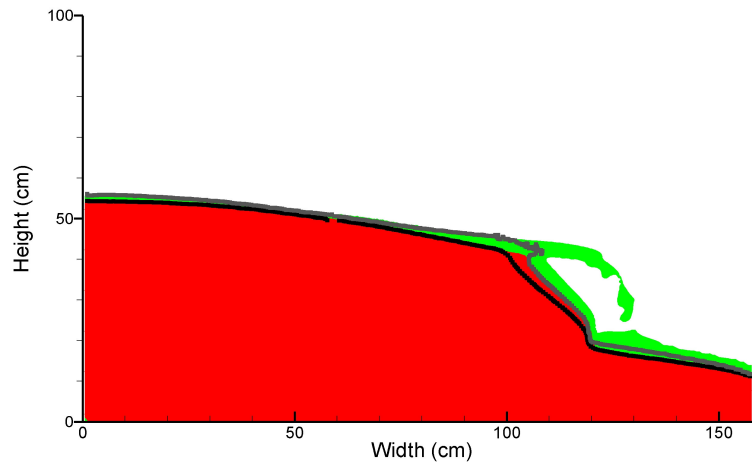


Figure IV.7: Comparison of simulated and experimental (black lines) results of E3_D after 120 min for $K_1=3.36 \times 10^{-9} \text{ m}^2$ and $r = 50\%$. The green area indicates concentrations between 5% and 50% and the red is above 50%.

In turn, the simulations of the tracer experiments using the dispersivity values of the density experiments ($r = 5\%$) deteriorated the fit between simulated and measured tracer isolines (Figure IV.8 vs. Figure IV.5). Therefore, it became obvious that a reduction of the longitudinal dispersion had a positive effect on the simulation results which shows the density dependence of dispersion.

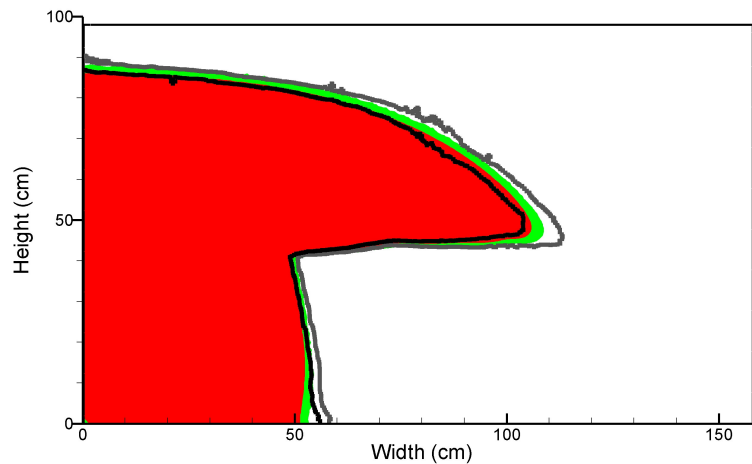


Figure IV.8: Comparison of simulated and experimental (black lines) results of E3_T after 75min for $K_1=3.36 \times 10^{-9} \text{ m}^2$ and $r = 5\%$. The green area indicates concentrations between 5% and 50% and the red is above 50%.

IV.1.7 Conclusions

Heterogeneous density-coupled flow tank experiments were conducted and simulated with a robust numerical code. Different boundary conditions were applied to the flow tank and the saltwater experiments were repeated using dyed freshwater in order to demonstrate the effects of density differences on the flow patterns and in order to derive the experimental parameters based on sensitivity analysis and inverse calibration. The density effects became visible and suggested a high relevance for the experimental flow patterns.

The experiments were simulated with a numerical code based on advanced approximations for both spatial and temporal discretizations. The code used the Method Of Lines (MOL) to allow higher-order temporal discretization and adapted in both the order of approximation and time step to provide the necessary accuracy. The simulation results generally showed that the numerical code was able to reproduce the experimental data satisfactorily. However, inaccuracies were observed for the simulation of the dispersion processes using the parameter values determined from the tracer experiments. Ten times decreased dispersivities delivered the most appropriate simulation results for the saltwater experiments. This is well in line with findings of *Hassanizadeh and Leijnse* [1995], who show a density-dependent dispersion, which induces a reduction of dispersivities for high density contrasts.

The density dependent flow phenomena were relevant for all saltwater experiments and the simulations were sensitive to numerical diffusion. Thus, the experiments are considered as suitable to investigate density flow phenomena and to test numerical codes under heterogeneous conditions.

IV.1.8 References

- Aavatsmark, I., 2002. An introduction to multipoint flux approximations for quadrilateral grids. *Computational Geosciences*, 6, 404-432.
- Ackerer, P., Younes, A., 2008. Efficient approximations for the simulation of density driven flow in porous media. *Advances in Water Resources*, 31, 15-27.
- Diersch, H.J., Kolditz, O., 2002. Variable-density flow and transport in porous media: approaches and challenges. *Advances in Water Resources*, 25, 899-944.
- Edwards, M.G., Rogers, C.F., 1998. Finite volume discretization with imposed flux continuity for the general tensor pressure equation. *Computational Geosciences*, 2, 259-290.
- Gemitzi, A., Tolikas, D., 2007. HYDRA model: Simulation of salt intrusion in coastal aquifers using Visual Basic and GIS. *Environmental Modelling & Software*, 22, 7, 924-936, DOI: 10.1016/j.envsoft.2006.03.007.
- Goswami, R., Clement, P., 2007. Laboratory-scale investigation of saltwater intrusion dynamics, *Water Resour. Res.* 43, W04418.

- Harleman, D.R.F., Rumer, R.R., 1963. Longitudinal and lateral dispersion in an isotropic porous medium, *J. Fluid Mech.*, 16, 3, 385–394.
- Hassanizadeh, S. M., A. Leijnse, 1995. A non-linear theory of high-concentration-gradient dispersion in porous media. *Advances in Water Resources*, 18, 4, 203-215.
- Huang, W.E., Oswald, S.E., Lerner, D.N., Smith, C.C., Zheng, C., 2003. Dissolved oxygen imaging in a porous medium to investigate biodegradation in a plume with limited electron acceptor supply, *Environ. Sci. Technol.*, 37, 9, 1905–1911, doi: 10.1021/es020128b.
- Huyakorn, P.S., Anderson, P.F., Mercer, J.W. , White, H.O., 1987. Saltwater intrusion in aquifers: development and testing of a three-dimensional finite element model. *Water Resources Research*, 23, 2, 293–312.
- Jiao C.Y., Hötzl, H., 2004. An experimental study of miscible displacements in porous media with variation of fluid density and viscosity. *Transport in Porous Media*, 54, 125–44.
- Johannsen, K., Kinzelbach, W., Oswald, S., Wittum, G., 2002. The saltpool benchmark problem – numerical simulation of saltwater upconing in a porous medium. *Advances in Water Resources*, 25, 335–348.
- Konz, M., Ackerer, P., Meier, E., Huggenberger, P., Zechner, E., Gechter, D., 2008. On the measurement of solute concentrations in 2-D flow tank experiments. *Hydrology and Earth System Sciences*, 12, 727-738.
- Konz, M., Ackerer, P., Younes, A., Huggenberger, P., Zechner, E., 2009a. 2D Stable Layered Laboratory-scale Experiments for Testing Density-coupled Flow Models. *Water Resources Research*, 45, doi:10.1029/2008WR007118.
- Konz, M., Ackerer, P., Huggenberger, P., Veit, C., 2009b. Comparison of light transmission and reflection techniques to determine concentrations in flow tank experiments. *Experiments in Fluids*, doi 10.1007/s00348-009-0639-0.
- Ludwig, R., Schelkes, K., Vogel, P., Wollrath, J., 2001. Implications of large scale heterogeneities for hydraulic conductivity model studies at the potential site of a radioactive waste repository at Gorleben, Germany. *Engineering Geology*, 61, 2-3, 119-30.
- Masciopinto, C., 2006. Simulation of coastal groundwater remediation: the case of Nardo fractured aquifer in Southern Italy. *Environmental Modelling & Software*, 21, 1, 85-97, DOI: 10.1016/j.envsoft.2004.09.028.
- Oostrom, M., Hayworth, J.S., Dane, J.H., Güven, O., 1992. Behavior of dense aqueous phase leachate plumes in homogeneous porous media. *Water Resources Research*, 28, 8, 2123–2134.

- Oswald, S., Kinzelbach, W. , 2004. Three-dimensional physical benchmark experiments to test variable-density flow models, *J. Hydrol.*, 290, 22–42.
- Perkins, T.K., Johnston, Q.C., 1963. A review of diffusion and dispersion in porous media, *Soc. Petrol. Engrs. J.*, 3, 1, 70–86.
- Schincariol, R.A., Schwartz, F.W., 1990. An experimental investigation of variable density flow and mixing in homogeneous and heterogeneous media, *Water Resour. Res.*, 26, 2317-2329.
- Schotting, R.J., Moser, H., Hassanizadeh, S.M., 1999. High-concentration gradient dispersion in porous media: experiments, analysis and approximations. *Advances in Water Resources*, 22, 665–80.
- Schotting, R.J., Landman, A.J., 2004. Towards a physically based theory of high-concentration-gradient dispersion in porous media – Experimental, theoretical and numerical studies. In: Ingham DB et al., editors. *Emerging technologies and techniques in porous media*, NATO Science Series II, vol. 134. Kluwer Academic Publishers, 321-336.
- Shuangzhang, T., Shahrouz, A., 2005. A slope limiting procedure in Discontinuous Galerkin finite element method for gas dynamics applications. *International Journal of Numerical Analysis and Modeling*, 2, 163-178.
- Simpson, M.J., Clement, T.P., 2003. Theoretical analysis of the worthiness of Henry and Elder problems as benchmarks of density-dependent groundwater flow models. *Advances in Water Resources*, 26, 17–31.
- Swartz, C.H., Schwartz, F.W., 1998. An experimental study of mixing and instability development in variable-density systems. *Journal of Contaminant Hydrology*, 34, 169-189.
- Watson, S.J., Barry, D.A., Scotting, R.J., Hassanizadeh, S.M., 2002. Validation of classical density-dependent theory for stable, high-concentration gradient brine displacements in coarse and medium sand. *Advances in Water Resources*, 25, 611–35.
- Younes, A., Ackerer, P., Lehmann, F., 2006. A new mass lumping scheme for the mixed hybrid finite element method. *International Journal for Numerical Methods in Engineering*, 67, 1, 89-107.
- Younes, A., Ackerer, P., 2008. Solving the Advection-Dispersion Equation with Discontinuous Galerkin and Multipoint Flux Approximation methods on unstructured meshes. *International Journal for Numerical Methods in Fluids*, 58, 6, 687-708.
- Younes, A., Fahs, M., Ahmed, S., 2009. Solving density driven flow problems with efficient spatial discretizations and higher-order time integration methods. *Advances in Water Resources*, doi: 10.1016/j.advwatres.2008.11.003.

V. Conclusions and outlook

Water resources management decisions often rely on numerical simulations. If density effects influence the flow dynamics the simulations of the highly non-linear coupled flow and transport equations is complicated. Therefore, reliable physical test cases are needed to evaluate the numerical codes and to investigate variable- density flow processes. In this thesis, two independent methods to determine salt concentrations in flow tanks were developed further and tested regarding their applicability to provide reliable data for testing numerical density-flow models. Furthermore, series of homogeneous and heterogeneous porous media experiments were conducted to study variable-density flow processes.

Within the resistivity method the voltage between two electrodes, which is controlled by the number of ions of the surrounding fluids, was measured. The measurement volume of the resistivity method was not known and it was not constant throughout the experiment. Therefore, the derived experimental data were hard to compare to simulation results.

Optical intensity data of a color dye were recorded and converted to concentration data in the photometric method. An image analysis technique based on measured reflection intensities was found to be suitable to determine breakthrough curves of concentrations as well as concentration isolines at distinct time steps. In comparison to the resistivity measurement technique, image analysis delivered spatial continuous concentration data. Thus, breakthrough curves can be derived in the post-processing after the experiment was conducted at positions where the information content was the highest. Lens flare effects turned out to be the major source of error and are more pronounced for light transmission measurements.

Different density-coupled and uncoupled flow problems were investigated in a flow tank ($158 \times 100 \times 4 \text{ cm}^3$) under homogeneous and heterogeneous porous media conditions and under geometries that were relevant to tectonical settings found in field scale problems. The heterogeneous porous medium was realized with two glass beads units. The fine beads were placed as a $80 \times 40 \text{ cm}^2$ block in the center of the tank. An impermeable layer divided the flow domain into two parts connected via a vertical channel in the experiment representing a tectonic setting of two aquifers connected by fault zones. The saltwater had to pass through the channel to reach the outlet of the tank above the impermeable layer. The experiments were designed specifically to enable numerical simulations of the experimental flow patterns. The saltwater front significantly spread at the outlet of the homogeneous experiment and a wave structure developed. A sharp front could be observed throughout the course of the complex geometry experiment and the saltwater moved along the top of the impermeable layer after having passed the channel. Within the heterogeneous experiments fingering effects due to local instability developments occurred. The density-flow experiments were simulated and the results were presented as benchmark tests.

Conclusions

The non-invasive photometric method based on measured reflection intensities is the most appropriate to derive comprehensive data sets of the flow tank experiments with

high accuracy. It has a well defined measurement area and a high resolution which enables a detailed investigation of flow patterns. The data processing method significantly reduces the impacts of instable illumination and optical heterogeneities of the glass beads. The direct conversion of measured intensities to concentration data without a previous transformation of intensity data to optical densities enables an effective processing of the measured raw data.

The dimension of the experiments enables the development of specific flow patterns which are characteristic for variable-density flow. Those patterns, e.g. the wave structure in the homogeneous experiment and the sharp front of the complex geometry experiment, are sensitive to the numerical inaccuracies and therefore well suited to test numerical models. The comparison of density-coupled and uncoupled experiments under equal boundary conditions clarifies the relevance of the density effects for the flow processes. The high data availability of the experiments allows a very detailed evaluation of the numerical models. Since the 50% isolines are dominated by advection and exhibit no dispersion, concentration levels higher or smaller than 50% are required to test for numerical diffusion. Breakthrough curves of concentration at various points of the tank give highly precise test data sets additional to the concentration isolines and show even slightest inaccuracies of the simulations. Simulation results show the need to use robust numerical schemes for the simulation of density-driven flow problems and highlight the quality of the very detailed experiments for benchmarking numerical codes. Thus, the MFE_DG_MPFPA code is recommended for field scale simulations.

The heterogeneous experiments exhibit different levels of instabilities depending on the boundary conditions. Instable fluid stratification develops if the higher density fluid has to flow around the lower permeability zone. Due to the different flow velocities in the two glass beads zones, higher density fluids are placed above fluids of lower density. Fingering effects at the horizontal interface between the two porous media zones can be observed. This leads to a convective mixing along the interface with a mass transfer from the coarse beads zone to the fine beads zone. Simulation results show that the applied code is able to reproduce the patterns of the measured isolines. A reduction of the longitudinal dispersion significantly improved the simulations what implies non-Fickian dispersion.

Besides the code testing, relevant conclusions can be drawn for the field scale subsidence problem in the region of Basel, especially for the setup of possible monitoring systems: Saltwater can reach the extraction wells in the upper aquifer from the lower aquifer through the fault zones.

The saltwater develops a concentration stratification in the Muschelkalk aquifer with highest concentrations at the top of the hydraulic barrier, e.g. in saltpools.

Effective groundwater monitoring systems need to consider the above mentioned effects. Furthermore, the sampling systems should be planed on the basis of numerical simulations at the regional scale.

Outlook

With the photometric method an effective non-invasive approach to measure solute concentrations is available, which can be used for further two dimensional fluid flow experiments. Such experiments could be designed in order to study, e.g. leakages from landfills associated with significant instable fluid stratifications.

The reliability of the numerical tools has been proven and further numerical studies on field scale subrosion processes could be conducted. 2D simulations of selected cross-sections based on field data and structures would improve the understanding of the driving forces for subrosion such as hydraulic boundary conditions and tectonic structures. As opposed to 3D simulations, the 2D simulations allow an analysis of a set of models with a significantly reduced CPU-time. Furthermore, the effects of the discretisation (element size) on instable situations (e.g. fingering due to dense water over fresh water) at the field scale should be analyzed in detail. These 2D simulations would provide guidelines for the discretisation of the 3D field. Finally, gained knowledge could contribute to a 3D simulation of density flow with field data and geological structures. This would help to improve the knowledge on regional flow fields such as at the presented subsidence area in the region of Basel. Based on this knowledge a monitoring system could be installed in the Upper Muschelkalk aquifer that enables the monitoring of subrosion processes in the halite horizon below the impermeable Anhydrites.

References

- Ackerer, P. & Younes, A. (2008): Efficient approximations for the simulation of density driven flow in porous media. *Adv. Water Res.*, 31, 1, 15-27.
- Aegerter, I. & Bosshardt, A.G. (1999): Technischer Bericht, Setzungsproblematik-Massnahmen gegen Setzungen. Bericht im Auftrag der SBB, unpublished.
- Alkattan, M., Oelkers, E. H., Dandurand, J.-L. & Schott, J. (1997): Experimental studies of halite dissolution kinetics, 1 the effect of saturation state and the presence of trace metals. *Chemical Geology*, 137, 201-219.
- Barth, G.R., Illangsekare, T.H., Hill, M.C. & Rajaram, H. (2001): A new tracer-density criterion for heterogeneous porous media. *Water Resour. Res.* 37, 21– 31.
- Bear J. (1972): *Dynamics of fluids in porous media*. New York: Elsevier.
- Berkowitz, B. & Scher, H. (1995): On characterization of anomalous dispersion in porous and fractured media. *Water Resour. Res.* 31, 6, 1461– 1466.
- Berkowitz, B. & Scher, H. (2001): The role of probabilistic approaches to transport theory in heterogeneous media. *Transp. Porous Media* 42, 241– 263.
- Brigham, W.E., Reed, P.W. & Dew, J.N. (1961): Experiments on mixing during miscible displacements in porous media. *Soc. Petrol. Eng. J.*, 1, 1–8.
- Catania, F., Massabo, M., Valle, M., Bracco, G. & Paladino, O. (2008): Assessment of quantitative imaging of contaminant distributions in porous media. *Exp. Fluids*. 44, 167–177.
- Cooper, C.A., Glass, R.J. & Tyler, S.W. (1997): Experimental investigation of the stability boundary of double-diffusive finger convection in a Hele-Shaw cell. *Water Resour. Res.*, 33, 4, pp 517ff.
- Corapcioglu, M.Y., Chowdhury, S. & Roosevelt, S.E. (1997): Micromodel visualization and quantification of solute transport in porous media. *Water Resour. Res.* 33, 11, 2547–2558.
- Croucher, A.E. & O’Sullivan, M.J. (1995): The Henry problem for seawater intrusion. *Water Resour. Res.*, 31, 7, pp. 1809ff.
- Danquigny, C., Ackerer, P. & Carlier, JP. (2004): Laboratory tracer tests on three-dimensional reconstructed heterogeneous porous media. *J. Hydrol.*, 294, 1-3, 196-212 Sp. Iss. SI JUL 15.

- Detwiler, R.L., Rajaram, H. & Glass, R.J. (2000): Solute transport in variable-aperture fractures: An investigation of the relative importance of Taylor dispersion and macrodispersion. *Water Resour. Res.* 36, 7, 1611– 1625.
- Diersch, H.J. (1996): Interactive, graphics-based finite-element simulation system FEFLOW for modeling flow, contaminant mass and heat transport processes. FEFLOW User's manual version 4.5, Berlin.
- Diersch, H.J. & Kolditz, O. (2002): Variable-density flow and transport in porous media: approaches and challenges. *Adv. Water Res.*, 25, 899–944.
- Durie, R.W. & Jessen, F.W. (1964): Mechanism of the dissolution of salt in the formation of underground cavities. *Soc. Pet. Engn. J.*, 4, 2, 183-190.
- Elder, J.W. (1967): Transient convection in a porous medium. *J. Fluid Mech.* 27, 3, 609–623.
- Frind, E. (1982): Simulation of long-term transient density-dependent transport in groundwater. *Adv. Water Res.*, 5, pp. 73ff.
- Frumkin, A. (1994): Morphology and development of salt caves. *NSS Bulletin*, 56, 82-95.
- Frumkin, A. (1998): Salt cave cross-sections and their paleoenvironmental implications. *Geomorphology*, 23, 183-191.
- Frumkin, A. (2000a): Dissolution of salt. In: Klimchouk, A. B., Ford, D. C., Palmer, A. N. & Dreybrodt, W. (eds): *Speleogenesis – evolution of karst aquifers*, 169-170. National Speleological Society, Huntsville.
- Frumkin, A. (2000b): Speleogenesis in salt – the Mount Sedom area, Israel. In Klimchouk, A. B., Ford, D. C., Palmer, A. N., Dreybrodt, W. (eds): *Speleogenesis – evolution of karst aquifers*. National Speleological Society, Huntsville, 443-451.
- Galeati, G., Gambolati, G. & Neuman, S.P. (1992): Coupled and partially coupled Eulerian-Lagrangian model of freshwater-seawater mixing. *Water Resour. Res.*, 28, pp. 149ff.
- Gechter, D. (2008): Genesis and Shapes of Salt and Gypsum Solution Cavities Created by density-driven Groundwater Flow: A Laboratory Experimental Approach. University of Basel, PhD-Thesis.
- Gelhar, L.W., Welty, C. & Rehfeldt, K.R. (1992): A critical review of data on field-scale dispersion in aquifers. *Water Resour. Res.*, 28 , 7, 1955– 1974.
- Goswami, R. & Clement, P. (2007): Laboratory-scale investigation of saltwater intrusion dynamics, *Water Resour. Res.*, 43, W04418.

- Greiner, A., Schreiber, W., Brix, G. & Kinzelbach, W. (1997): Magnetic resonance imaging of paramagnetic tracers in porous media: Quantification of flow and transport parameters. *Water Resour. Res.*, 33, 6, pp. 1416ff.
- Gürler, B., Hauber, L. & Schwander, M. (1987): Die Geologie der Umgebung von Basel mit Hinweisen über die Nutzungsmöglichkeiten der Erdwärme. Beitrag zur Geologischen Karte der Schweiz.
- Guillot, G., Kassab, G., Hulin, J.P. & Rigord, P. (1991): Monitoring of tracer dispersion in porous media by NMR imaging. *J. Phys. D, Appl. Phys.*, 24, pp. 763ff.
- Hassanizadeh, S.M & Leijnse, A. (1988): On the modeling of brine transport in porous media. *Water Resour. Res.*, 24, 3, 321–30.
- Hassanizadeh, S.M. & A. Leijnse (1995): A non-linear theory of high-concentration-gradient dispersion in porous media. *Adv. Water Res.*, 18, 4, 203-215.
- Hauber, L. (1971): Zur Geologie des Salzfeldes Schweizerhalle-Zinggibrunn (Kt. Baselland). *Elogae geol. Helv.*, 64(1), 163-183.
- Heim, A. (1919): Geologie der Schweiz. Leipzig.
- Henry, H.R. (1964): Effects of dispersion on salt encroachment in coastal aquifers, in *Seawater in Coastal Aquifers*, U.S. Geol. Surv. Supply Pap., 1613-C, 70-84.
- Herbert, A., C. Jackson & D. Lever (1988): Coupled Groundwater Flow and Solute Transport With Fluid Density Strongly Dependent Upon Concentration. *Water Resour. Res.*, 24, 10, 1781-1795.
- Hoffman, F., Ronen, D. & Pearl, Z. (1996): Evaluation of flow characteristics of a sand column using magnetic resonance imaging. *J. Contam. Hydrol.*, 22, 95– 107.
- Huang, W., Smith, C.C., Lerner, D.N., Thornton, S.F. & Oram, A. (2002): Physical modelling of solute transport in porous media: evaluation of an imaging technique using UV excited fluorescent dye. *Water Res.*, 3, 7, 1843–1853.
- Huyakorn, P.S., Anderson, P.F., Mercer, J.W. & White, H.O. (1987): Saltwater intrusion in aquifers: development and testing of a three-dimensional finite element model. *Water Resour. Res.*, 23, 2, 293–312.
- Istok, J.D. & Humphrey, M.D. (1995): laboratory investigation of buoyancy-induced flow (plume sinking) during two-well tracer tests. *Ground Water*, 33, 4, pp. 597 ff.
- James, A. N. (1992): Soluble materials in civil engineering. Ellis Horwood, Chichester.

- Johns, R.T. & Rivera, A. (1996): Comment on “Dispersive transport dynamics in a strongly coupled groundwater-brine flow system” by Oldenbourg, C and Preuss, K. *Water Resour. Res.*, 32, 11, pp. 3405ff.
- Jones, E.H. & Smith, C.C. (2005): Non-equilibrium partitioning tracer transport in porous media: 2-D physical modelling and imaging using a partitioning fluorescent dye. *Water Res.*, 39, 20, 5099–5111.
- Johnson, K.S. (1981): Dissolution of salt on the east flank of the Permian Basin in the southwestern U.S.A. *J. Hydrol.*, 54, 75-93.
- Johnson, K.S. (1992): Evaporite karst in the Permian Blaine Formation and associated strata in Western Oklahoma, USA. *Int. Contributions to Hydrogeology*, 13, 405-420.
- Johannsen, K., Kinzelbach, W., Oswald, S. & Wittum, G. (2002): The saltpool benchmark problem – numerical simulation of saltwater upconing in a porous medium. *Adv. Water Res.*, 25, 335-348.
- Kempers, L. (1991): Dispersive mixing in stable and unstable miscible displacements. Unpublished Ph.D. thesis, Delft University of Technology, Delft, The Netherlands.
- Kinzelbach, W., Oswald, S. & Schwarz, C (1998): Abschlussbericht der Arbeitsgruppe Kinzelbach zum Projekt „Entwicklung eines schnellen Programms zur Modellierung von Grundwasserströmungen mit variabler Dichte“. Institut für Hydromechanik und Wasserwirtschaft, ETH Zürich.
- Koch, M. & Zhang, G. (1992): Numerical simulation of the effects of variable density in a contaminant plume. *Ground Water*, 30, 5.
- Kolditz, O., Ratke, R., Diersch, H.J. & Zielke, W. (1998): Coupled groundwater flow and transport: 1 Verification of variable density flow and transport models. *Adv. Water Res.*, 21, 1, pp 27ff.
- Konikow, L.F., Sanford, W.E. & Campbell, P.J. (1997): Constant-concentration boundary condition: Lessons from the HYDROCOIN variable-density groundwater benchmark problem. *Water Resour. Res.*, 33, 10, pp. 2253ff.
- Konz, M., Ackerer, P., Meier, E., Huggenberger, P., Zechner, E. & Gechter, D. (2008a): On the measurement of solute concentrations in 2-D flow tank experiments. *Hydrol. Earth Syst. Sci.*, 12, 727-738.
- Konz, M., Ackerer, P., Younes, A., Huggenberger, P. & Zechner, E. (2008b): Experimental procedures for benchmarking density-coupled numerical codes. Proceedings of HydroPredict conference 2008, Predictions for Hydrology, Ecology and Water Resources Management: Using data and Models to benefit Society. ISBN 978-80-903635-3-3.

Konz, M., Ackerer, P. & Huggenberger, P. (2009a): Comparison of light transmission and reflection techniques to determine concentrations in flow tank experiments. *Exp Fluids*, 47, 85–93.

Konz, M., Ackerer, P., Younes, A., Huggenberger, P. & Zechner, E. (2009b): Two-dimensional stable-layered laboratory-scale experiments for testing density-coupled flow models. *Water Resour. Res.*, 45, doi:10.1029/2008WR007118.

Konz, M., Ackerer, P., Younes, A., Fahs, M., Huggenberger, P. & Zechner, E. (2009c): Variable-density flow in heterogeneous porous media – Laboratory experiments and numerical simulation. *J. of Cont. Hydrol*, 108, 168–175.

McNeil, J.D., Oldenborger, G.A. & Schincariol, R.A. (2006): Quantitative imaging of contaminant distributions in heterogeneous porous media laboratory experiments. *J. Contam. Hydrol.* 84 , 36-54.

Nield, D.A. & Bejan, A. (1992): *Convection in porous media*. Springer Verlag, New York.

Laubscher, H.P. (1982): Die Südostecke des Rheingrabens - ein kinematisches und dynamisches Problem. *Eclogae geol. Helv.*, 75, 1, 101-116.

Leijnse, A. (1992): *Three-Dimensional Modeling of Coupled Flow and Transport in Porous Media*, PhD-Thesis, Notre Dame, Indiana.

Levy, M. & Berkowitz, B. (2003): Measurement and analysis of non-Fickian dispersion in heterogeneous porous media. *Journal of Cont. Hydrol.*, 64, 203–226.

Ludwig, R., K. Schelkes, P. Vogel & J. Wollrath (2001): Implications of large scale heterogeneities for hydraulic conductivity model studies at the potential site of a radioactive waste repository at Gorleben, Germany. *Eng. Geol.*, 61, 2-3, 119-30.

Molson, J.W. & Friend, E.O. (1994): *Saltflow, Version 2.0, density-dependent flow and mass transport model in three dimensions, User Guide*, Waterloo Centre for Groundwater Research, University of Waterloo, Waterloo, Ontario, Canada.

Nield, D.A. & Bejan, A. (1992): *Convection in porous media*. Springer Verlag, New York.

OECD (1988): *Hydrocoin Project, The International Hydrocoin Project, Level 1: Code Verification*, OECD, Paris, France.

Oldenbourg, C. & Preuss, K. (1995): Dispersive transport dynamics in a strongly coupled groundwater-brine flow system. *Water Resour. Res.*, 31, 2, pp. 289ff.

Oldenbourg, C., Preuss, K. & Travis, B.J. (1996): Reply. *Water Resour. Res.*, 32, 11, pp. 3411ff.

Oostrom, M., Hayworth, J.S., Dane, J.H. & Güven, O. (1992a): Behavior of dense aqueous phase leachate plumes in homogeneous porous media. *Water Resour. Res.*, 28, 8, 2123–2134.

Oostrom, M., Dane, J.H., Güven, O. & Hayworth, J.S. (1992b): Experimental investigation of dense solute plumes in an unconfined aquifer model. *Water Resour. Res.*, 28, 9, 2315–2326.

Oostrom, M., Hofstee, C., Lenhard, R.J. & Wietsma, T.W. (2003): Flow behavior and residual saturation formation of liquid carbon tetrachloride in unsaturated heterogeneous porous media. *J. Contam. Hydrol.*, 64, 93–112.

Oswald, S., Schwarz, C. & Kinzelbach, W. (1996): Benchmarking in numerical modelling of density driven flow. Proc. of 14th saltwater intrusion meeting SWIM 96, report No. 87, Geological Survey of Sweden, Uppsala, Sweden, pp. 32ff.

Oswald, S., Kinzelbach, W., Greiner, A. & Brix, G. (1997): Observation of flow and transport processes in artificial porous media via magnetic resonance imaging in three dimensions. *Geoderma* 80, 417–429.

Oswald, S. & Kinzelbach, W. (2004): Three-dimensional physical benchmark experiments to test variable-density flow models. *J. Hydrol.* 290, 22–42.

Oswald, S., Spiegel, M. & Kinzelbach, W. (2007): Three-dimensional saltwater–freshwater fingering in porous media: contrast agent MRI as basis for numerical simulations. *Mag. Reson. Imaging*, 25, 4, 537 – 540.

Pearl, Z., Magaritz, M. & Bendel, P. (1993): Nuclear magnetic resonance imaging of miscible fingering in porous media. *Transp. Porous Media* 12, 107–123.

Pearson, F.J., Balderer, W., Loosli, H.H., Lehmann, B.E., Matter, A., Peters, T., Schmassmann, H. & Gautschi, A. (1991): *Applied Isotope Hydrogeology—a case study in northern Switzerland*. Elsevier.

Rahman, A., Jose S., Nowak W. & Cirpka, O. (2005): Experiments on vertical transverse mixing in a large-scale heterogeneous model aquifer. *J. Contam. Hydrol.* 80, 130–148.

Rezanezhad, F., Vogel, H.J. & Roth, K. (2006): Experimental study of fingering flow through initially dry sand. *Hydrol. Earth Syst. Sci. Discuss.*, 3, 2595–2620.

Reuter, F., Klengel, K.J. & Pašek, J. (1992): *Ingenieurgeologie*. Deutscher Verlag für Grundstoffindustrie GmbH, Leipzig, Stuttgart.

Reuter, F. & Tolmačëv, V.V. (1990): *Bauen und Bergbau in Senkungs- und Erdfallgebieten. Eine Ingenieurgeologie des Karstes*. Schriftreihe für Geologische Wissenschaften, 28, Akademie-Verlag Berlin.

Reuter, F. & Stoyan, D. (1993): Sinkholes in carbonate, sulphate, and chloride karst regions: Principles and problems of engineering geological investigations and predictions, with comments for the destruction and mining industries. In Beck, B.F. (ed.): Applied karst geology, Proceedings of the fourth multidisciplinary conference on sinkholes and the engineering and environmental impacts of karst, Panama City, Florida, 1, 3 – 25.

Ritzel, A. (1911): Die Kristalltracht des Chlornatriums und ihrer Abhängigkeit vom Lösungsmittel. *Z. Kristallogr.*, 49, 152-192.

Schincariol, R.A. & Schwartz, F.W. (1990): An experimental investigation of variable density flow and mixing in homogeneous and heterogeneous media. *Water Resour. Res.*, 26, 2317-2329.

Segol, G. (1994): *Classic groundwater Simulations*. PTR Prentice Hill, New Jersey.

Silliman, S.E. & Simpson, E.S. (1987): Laboratory evidence of the scale effects in dispersion of solutes in porous media. *Water Resour. Res.* 23, 1667–1673.

Simmons, C.T., Pierini, M.L. & Hutson, J.L. (2002): Laboratory investigation of variable-density flow and solute transport in unsaturated–saturated porous media. *Transp. Porous Media* 47, 15– 244.

Simpson, M.J. & T.P. Clement (2003): Theoretical analysis of the worthiness of Henry and Elder problems as benchmarks of density-dependent groundwater flow models, *Advances in Water Res.*, 26, 17–31.

Slobod, R.L. & Howlett, W.E. (1964): The effects of gravity segregation in laboratory studies of miscible displacement in vertical unconsolidated porous media. *Soc. Petrol. Eng. J.*, 4, 1–8.

Spottke I., Zechner, E. & Huggenberger, P. (2005): The southeastern border of the Upper Rhine Graben: A 3D geological model and its importance for tectonics and groundwater flow. *Int. J. of Earth Sciences*, 94, 580-593.

Standards Australia (1995): *Methods of testing soils for engineering purposes—Soil classification tests—Determination of the particle size distribution of a soil—Standard method of analysis by sieving*. AS1289.3.6.1.

Swartz, C.H. & Schwartz, F.W. (1998): An experimental study of mixing and instability development in variable-density systems. *J. Contam. Hydrol.*, 34, 169-189.

Theodoropoulou, M.A, Karoutsos, V., Kaspiris, C. & Tsakiroglou, C.D. (2003): A new visualization technique for the study of solute dispersion in model porous media. *J Hydrol.*, 27, 1–4, 176–197.

Thury, M., Gautschi, A., Mazurek, M., Müller, W.H., Naef, H., Pearson, F.J., Vomvoris, S. & Wilson, W. (1994): *Geology and hydrogeology of the crystalline basement of*

northern Switzerland—synthesis of regional investigations 1981–1993 within the Nagra Radioactive Waste Disposal Programme. Technical Report 93–01.

Trefzger, E. (1925): Die Tektonik des westl. Dinkelbergs und des nördl. Tafeljuras bei Basel. Ber. natf. Ges. Freiburg i.Br., 24, 1-63.

Trefzger, E. (1950): Die Steinsalzlagerstätte von Rheinfelden (Baden). Stratigraphie, Solung und Senkung. Jber.u.Mitt.oberrh.geol.Ver., N.F. 32.

Verloop, J. H. (1909): Die Salzlager der Nordschweiz., Basel.

Voss, C.I. & Souza, W.R. (1987): Variable density flow and solute transport simulation of regional aquifers containing narrow a freshwater-saltwater transition zone. Water Resour. Res., 23, 10, pp. 1857ff.

Wagner, C. (1949): The dissolution rate of sodium chloride with diffusion and natural convection as rate-determining factors. J. Phys. Colloid Chem., 53, 1030-1033.

Watson, S.J., Barry, D.A., Scotting, R.J. & Hassanizadeh, S.M. (2002): Validation of classical density-dependent theory for stable, high-concentration gradient brine displacements in coarse and medium sand. Adv. Water Res., 25, 611–35.

Wildenschild, D. & Jensen, K.H. (1999): Laboratory investigations of effective flow behavior in unsaturated heterogeneous sands. Water Resour. Res. 35, 17–27.

Wooding, R.A., Tyler, S.W. & White, I. (1997a): Convection in groundwater below an evaporating salt lake: 1. onset of instability. Water Resour. Res., 33, 6, pp. 1119ff.

Wooding, R.A., Tyler, S.W., White, I. & Anderson, P.A. (1997b): Convection in groundwater below an evaporating salt lake: 2. Evolution of fingers or plumes. Water Resour. Res., 33, 6, pp. 1219ff.

Curriculum Vitae

Markus Konz

Born on 10th February 1980 in Bietigheim-Bissingen, Germany

Education

2006-2009 PhD at University of Basel Switzerland, and University of Strasbourg, France
2000 - 2005 BSc and MSc in Hydrology, University of Freiburg, Germany
1990 - 1999 Christoph-Schrempf Gymnasium, Besigheim

Experience Record

10/2007 – 1/2008 McKinsey & Company
10/2005 – 12/2005 Munich Re Group
07/2005 – 10/2005 German Federal Institute of Hydrology, Bavarian Academy of Sciences
01/2004 – 03/2004 Ministry of Agriculture, Water Resources Authority, Jamaica
03/2004 Community Based Disaster Management Project (UNDP)
09/2003 – 12/2003 German Federal Institute of Hydrology, Bavarian Academy of Sciences
05/2002 – 12/2002 Environmental Engineering Company, Ingenieurgesellschaft für Umwelttechnik mbH, Kirchzarten, Germany
02/2002 – 04/2002 Environmental Engineering Company, IFB-Eigenschenk GmbH, Deggendorf, Germany